Draft version 0.0

ATLAS NOTE

January 15, 2012

Measuring azimuthal anisotropy of particle productions in $Pb + Pb$ collisions at $\sqrt{s_{NN}}$=2.76 TeV using event plane method

Jiangyong Jia[a,c] and Soumya Mohapatra[a]

[a]*Department of Chemistry,Stony Brook University, Stony Brook, NY 11794, USA*
[c]*Brookhaven National Laboratory, Physics Department, Bldg. 510A, Upton, NY 11973, United States of America*

Abstract

We present a measurement of the harmonic flow coefficent v_n in Pb+Pb collisions at $\sqrt{s_{NN}}$=2.76 TeV using the event plane determined by the Forward Calorimeter (Fcal) in ATLAS which situated symmetrically along the beam line in both the positive η and negative η. Significant v_n signals are observed for n=2-6 in a broard ranges of p_T, centrality and η. We see that the p_T dependence of the higher order coefficents (n=3 and above) has similar p_T dependence as v_2, namely it increases to about 3-4 GeV and then decreases at higher p_T, however such dependence is quantitatively much stronger than that oberved for v_2. A simple scaling relation $v_n^{1/n} \propto v_2^{1/2}$ are found to discribe these different p_T dependence rather well. The centrality dependence of the v_n suggest that they all increases to mid-central collisions and then drop towards peripheral collisions. however the level of centrality varition is much smaller for $v_3 - v_6$ than that for v_2. We also measured the η dependence of the v_n, only a weak decrease within $0 < |\eta| < 2.5$ is seen. Suggesting that the v_n is almost boost invariant in a rather larger rapidity window.

Contents

1 Introduction

The central focus of heavy ion program at RHIC and LHC is to understand the properties of the strongly interacting Quark Gluon Plasma (sQGP) created in heavy ion collisions. A common tool used to study the properties of the sQGP is the azimuthal anisotropy of particles emitted in the transverse plane. A non-zero anisotropy can be traced to the elliptic shape of the initial fireball and the strong final state interaction which transfers such spacial asymmetry into the transverse momentum (p_T) space. Such final state interactions lead to an effective anisotropic pressure gradient in the overlap region, with a larger pressure gradient along the short axis of the fireball. This anisotropic pressure gradient drives an anisotropic collective expansion (or flow) of the fireball, which can be modelled via relativistic viscous hydrodynamic models. The magnitude of the azimuthal anisotropy is sensitive to properties of the sQGP such as the kinetic viscosity (the ratio of shear viscosity to entropy density η/s) and equation of state (EOS).

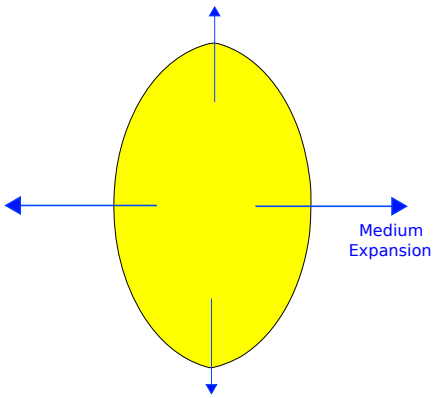

Figure 1: The elliptic fireball formed in a heavy-ion collision. There is a greated pressure gradient along the minor axis (called reaction plane) than along the major axis. This results in a greater yield ofparticles along the in-plane direction.

If we treat the nucleus a smooth function described by Woods-Saxon geometry, then the overlap region has an almost elliptic shape (see Fig.1). This spatial asymmetry can be quantified by the eccentricity of of the overlap region.

$$\begin{aligned} \epsilon_2 &= \frac{\langle y^2\rangle - \langle x^2\rangle}{\langle y^2\rangle + \langle x^2\rangle} \\ &= \sqrt{\frac{\langle r^2\cos 2\phi\rangle + \langle r^2\sin 2\phi\rangle}{\langle r^2\rangle}} \end{aligned} \tag{1}$$

where the (x, y) and ϕ are the position and azimuthal angle of a participating nucleons, and $r^2 = x^2 + y^2$.

The anisotropy of particles in final momentum space relative to the short axis can be approximated as

$$dN/d\phi \propto 1 + 2v_2\cos 2(\phi - \Psi_2) \tag{2}$$

Where Ψ_2 is the orientation of the short axis(called reaction plane or RP) and $v_2 = \langle\cos 2(\phi - \Psi_2)\rangle$ characterizes the magnitude of the anisotropy. Measurements from RHIC and LHC suggests that $v_2 \propto \epsilon_2$, with the proportional constant being sensitive to η/s and EOS. Current best fit of the viscous hydrodynamic

calculation to RHIC suggest a η/s to be $\sim 1-2.5$ times $\frac{1}{4\pi}$, the conjectured lower bound from AdS/CFT gravity-gauge dual theory.

Experimentally, the direction of RP is usually estimated using event shape (the azimthal distribution of particles of the whole event). The precision of such estimation depends on the kinematic selection of the particles such as p_T or η. The estimated direction is known as event plane (EP) to distinguish from the truth reaction plane.

So far we just considered the elliptic component of the overlap region. In general, the fireball may have other higher order shape deformations. This is because each nucleus is consists of finite number of nucleons whose positions could fluctuate from event to event. Such fluctuations were shown to lead to significant event-by-event higher moment shape distortions of the overlap region (see Figure 2).

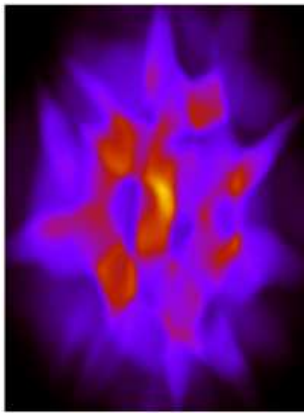

Figure 2: Fluctuating geometry of an heavy ion collision from Galuber model calculations.

These shape deformations, similar to ϵ_2, can be transferred into higher order azimuthal anisotropy in the p_T space via hydrodynamic evolution. Thus the azimuthal distribution of particles may contains higher moments of modulation:

$$dN/d\phi \propto 1 + 2\sum_{n=1}^{\infty} v_n \cos n(\phi - \Psi_n) \tag{3}$$

Where Ψ_n is the n^{th} order reaction plane and the harmonics $v_n = \langle \cos n(\phi - \Psi_n) \rangle$ characterize the strength of the n^{th} order azimuthal anisotropy.

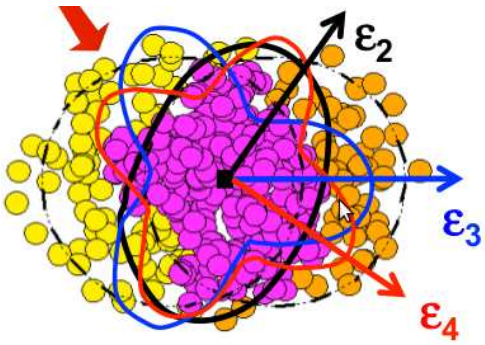

Figure 3: Depiction of a heavy-ion collisions showing the elliptic, triangular and square anisotropies .

However, instead of the usual r^2 weighting, the deformations relevant for n^{th} order azimuthal anisotropy were found to take the following form

$$\epsilon_n = \sqrt{\frac{\langle r^n \cos n\phi \rangle + \langle r^n \sin n\phi \rangle}{\langle r^n \rangle}}$$

Due to the r^n weighting, the higher order harmonics are more sensitive to later stage evolution of the fireball, where the effect of the viscosity is more pronounced. The general expectation is that the higher order harmonic flow should be more strongly damped relative to v_2. Thus measurement of the v_n can help to constrain the initial geometry and provide independent constraints on the EOS and η/s.

Finally, measurement of higher order harmonics also serves very important role to properly interpret the two-particle correlation results at the RHIC and LHC. These correlation measurement was aimed to probe the in-medium modification of jet and dijets in heavy ion collisions. Previous measurements have shown novel long range $\Delta\eta$ correlation structure at the near-side (the ridge) and split double peak structure at the away-side (the cone). These structures has been argued to reflect medium response to quenched jets, however they could also be mimicked the presence of higher order collective harmonic flow, such as v_2, v_3, v_4. So a direct and detailed measurement of the v_n allows a systematic decomposition of medium response from the collective flow.

ATLAS detector is well suited for collective flow measurement in heavy ion collisions. It not only has an extensive coverage for charged hadrons (2π in azimuth and ± 2.5 units in η) measurement, and but also provides precision measurement of the event plane (EP) in forward rapidity ($3.3 < \eta < 4.8$). ATLAS recorded $9ub^{-1}$ high quantity Pb+Pb from last year's heavy ion run. This large high quality dataset, combined with excellent detector capabilities allow a detailed measurement of harmonic flow to un-precedented precision. In this note, we present a detailed differential measurement of the harmonic flow v_2 to v_6 as a function p_T, centrality and η. The standard event plane (EP) method with a large rapidity gap is used.

This note is organized as follows, we first discuss the basic cuts for run and track selection, we then present EP measurement, resolution determination, v_n measurement and studies on systematic errors, followed by the results.

2 Event and Track selections

From Nov6-Dec.6, ATLAS recorded $9.17\mu b^{-1}$ of Pb+Pb data. The list of runs and cut conditions is summarized at https://twiki.cern.ch/twiki/bin/viewauth/Atlas/HeavyIonRunList. In order to select good events, we also apply some additional cuts to remove background (these are the minimum bias cuts):

- The event must be from a good lumi-block
- The event must pass atleast one of the following triggers (after Pre-scale):
  - MBTS_1_1
  - MBTS_2_2
  - MBTS_3_3
  - MBTS_4_4
  - L1_ZDC_AND
  - L1_ZDC_A_C
- The event must pass L1_ZDC_AND or L1_ZDC_A_C triggers (before prescale)
- It must have good MBTS timing
  - $|mbtime\_timeA|$ or $|mbtime\_timeC|$ must not equal 75 or 0
  - $|mbtime\_timeA - mbtime\_timeC|$ must be less than 3
- It must have a reconstructed vertex

We also reject small runs (with less than $10mb^{-1}$). We obtain a total of 45.7 Millons good events from 34 runs. We also apply a $|Z_{vtx}| < 150mm$ cut and only analyze events with $centrality < 95\%$ which reduces the number of evente to 37.4M. The list of runs and associated luminosity information is summarized in Table 1.

Run	Good LB	Total live Luminosity	events $\lvert z_{vtx}\rvert$ < 250mm	cent< 95% &events $\lvert z_{vtx}\rvert$ < 150mm	cent< 95% & events $\lvert z_{vtx}\rvert$ < 100mm
169045	333	75.6	508461	485299	460903
169136	545	171.7	1158058	1088462	998830
169175	458	376.1	2388525	2240828	2045971
169206	374	186.9	1226132	1144846	1028244
169207	56	76.7	461753	430201	385537
169223	405	378.4	2020777	1865148	1628519
169224	96	45.6	281777	258823	222817
169226	366	257.2	1745883	1630158	1461450
169270	311	298.1	2011015	1873270	1668055
169564	140	123.7	840386	784638	702633
169566	192	126.2	864655	796759	692390
169567	114	69.7	473710	446278	403882
169627	385	364.6	2308700	2131652	1859507
169648	63	66.5	448841	418645	375627
169693	568	396.3	2641298	2446958	2153561
169750	368	199.3	1339548	1255121	1134400
169751	163	96.1	652424	607893	540507
169765	307	161.8	1086637	1014877	907601
169783	63	31.5	211231	199004	183284
169839	222	197.2	1323701	1226869	1077826
169864	240	231.7	1561529	1464078	1325156
169927	575	526.5	3546973	3277671	2869331
169961	326	314.0	2116371	1973672	1749519
169964	93	94.6	636116	600539	543873
169966	121	83.1	550913	518079	468713
170002	462	522.8	3470018	3229078	2839374
170004	409	421.6	2877836	2672519	2347999
170015	161	236.1	1576022	1474166	1306844
170016	206	227.3	1511267	1396119	1205492
170080	27	28.2	188816	178615	162787
170082	117	147.0	982653	922273	824207
170398	380	392.6	2676024	2501053	2218872
170459	295	253.2	1726034	1622258	1457597
170482	212	314.3	2137288	2008045	1802582
Sum	9153	7639.5	49,551,372	46,183,894	41,053,890

Table 1: List of used runs showing the total luminosity, the number of events passing the trigger cuts (“events” column).

The centrality class is then defined using the the transverse energy deposited in FCal to categorize the event into percentiles. Details of the event centrality selections are documented in Heavy Ion centrality note. An Example Fcal energy distribution passing the trigger cuts and the corresponding centrality percentile distributions produced using the official centrality definition are shown in Fig. 4.

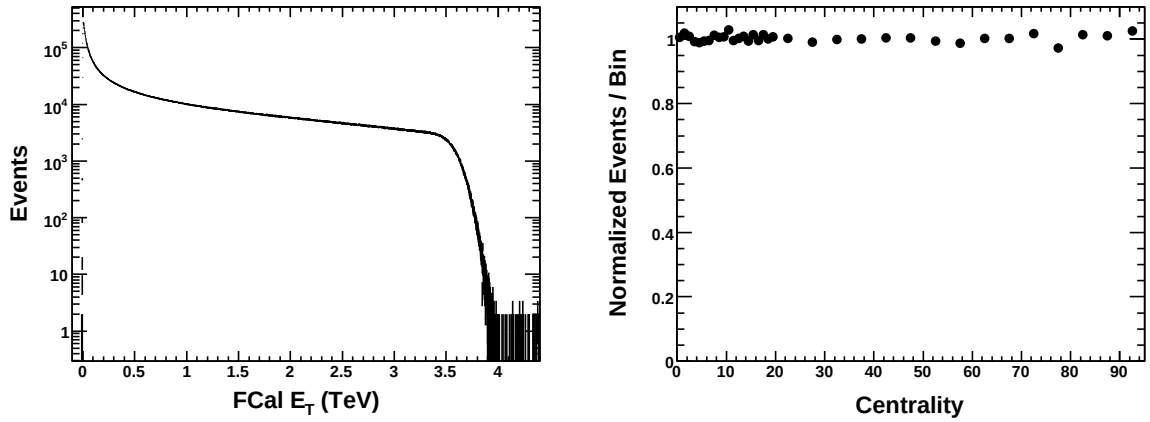

Figure 4: E_T distribution if FCal and the corresponding Centrality distribution of events

The charged particles used in this analysis are required to pass the following cuts (these are the ”tight cuts” also used by the Flow group):

- Number of B-Layer hits > 0 if expected number of B-layer hits=1
- Number of Pixel hits > 0
- Number of Pixel holes = 0
- Number of SCT Hits > 7
- Number of SCT Holes <2
- $0.5 < p_T < 20GeV$
- $2.5 < \eta < 2.5$
- $\chi^2/ndf < 6.0$
- $|d_0| < 1mm$
- $|z_0 \times \sin(\theta)| < 1mm$

3 Methodology

The event plane or EP method involves determining the reaction plane for an event using one detector and then measuring the distribution of particles (or E_T) about that plane using another detector. A rapidity gap is required to suppress the auto-correlations between the two detectors. The detailed discussion of the mathematics of this method is provided in the appendix, here we only present the most relevant steps and formulas.

The reaction plane angle of a event is defined by the azimuthal anisotropy of particles in that event; thus it can be estimated independently using detectors sitting at different η region. The large acceptance and radial segmentation of the ATLAS detectors provide many independent ways to measure the EP. Some of these studies have been documented in he Physics Performance Report for the heavy ion group. This analysis uses the first two layers of the Forward Calorimeter (Fcal) detector as the reaction plane detector, which provide reasonable precision for v_2 to v_6, while minimizing the auto-correlations with the

tracks. Once the orientation of the n^{th} order reaction plane Ψ_n is determined, we then correlate the tracks reconstructed in the Inner Detector w.r.t this plane to obtain the v_n values.

Figure5 illustrate the idea behind the method. The elongated red blob in this figure is the fireball extended in the η direction. Detector situated at different η sees the same collision geometry. Thus we can use the Fcal E_T to measure the orientation of the EP Ψ_n, then correlate the tracks to the EP to determine the flow coefficients. Due to flow correlations the E_T distribution can be expressed as a Fourier series

$$dE_T/d\phi = Q_0 + 2\sum_{n=1}^{\inf} |\overrightarrow{Q_n}| \cos n(\phi - \Psi_n) \tag{4}$$

where the flow vector $\overrightarrow{Q_n}$ can be calculated by summing the E_T of individual towers which has a segmentation of 0.1×0.1 in ϕ and η.

$$\overrightarrow{Q_n} = (Q_{x,n}, Q_{y,n}) = (\sum_i E_{T,i} \cos 2\phi_i, \sum_i E_{T,i} \sin 2\phi_i) \tag{5}$$

The orientation of the Q vector gives the EP angle Ψ_n,

$$\Psi_n = \frac{1}{n}\tan^{-1}\left(\frac{Q_{y,n}}{Q_{x,n}}\right) = \frac{1}{n}\tan^{-1}\left(\frac{\Sigma\, E_T \sin(n\phi)}{\Sigma\, E_T \sin(n\phi)}\right) \tag{6}$$

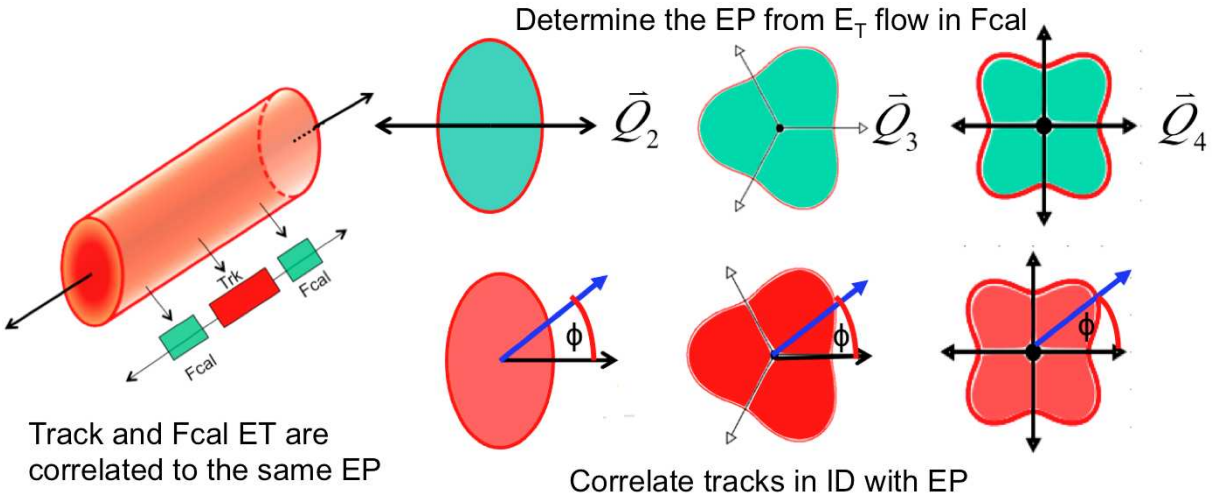

Figure 5: Schematic description of the event plane method. Both the Reaction Plane detector, Fcal, and the tracks are correlated to the same geometry. Thus one can use the Fcal E_T to measure the orientation of the EP Ψ_n, then correlate the tracks to the EP to determine the flow coefficients. The rapidity gap between the two suppress the short range and jet correlations.

Once the n^{th} order event plane Ψ_n is determined, one then correlate it with the tracks from ID to obtain the raw harmonic coefficient v_n^{obs}. However, due to smearing of the Ψ_n around true n^{th} order RP $\Psi_{RP,n}$. The observed v_n is diluted by a resolution factor Res$\{\Psi_n\}$

$$\frac{dN}{d\phi} \propto 1 + 2\sum_{n=1}^{\infty} v_n \cos n\,(\phi - \Psi_{RP,n}) = 1 + 2\sum_{n=1}^{\infty} v_n \mathrm{Res}_n \cos n\,(\phi - \Psi_n) = 1 + 2\sum_{n=1}^{\infty} v_n^{obs} \cos n\,(\phi - \Psi_n)$$

where

$$\mathrm{Res}\{\Psi_n\} = \langle \cos\,(n(\Psi_n - \Psi_{\mathrm{RP,n}}))\rangle$$

Thus the observed the observed coefficient need to be corrected by this dilution factor,

$$v_n = \frac{v_n^{\rm obs}}{\rm Res\{\Psi_n\}} = \frac{\langle \cos\left(n(\phi - \Psi_n)\right)\rangle}{\langle \cos\left(n(\Psi_n - \Psi_{\rm RP,n})\right)\rangle}. \quad (7)$$

and the main task in EP analysis involves determining the resolution factor $\rm Res_n$ and measure the raw harmonic flow signal v_n^{obs}.

4 Data reduction

4.1 Reaction plane detector

The Fcal detectors cover pseudo-rapidity range $3.2 < |\eta| < 4.9$, and are consists two symmetric subdetectors along the beam direction: one on the positive η ($Fcal_P$) and the other at the negative η ($Fcal_N$). Each fcal detector has three longitudinal segmentations. The first layer is an EM calorimeter and the second and third layers are hadronic calorimeters. Each layer are subdivided into cells with 0.1×0.1 segmentation in η and ϕ. We only use cells from the first two layers, as the third layer contains little energy and is more susceptable to noises; we also restrict the cells in the range $3.3 < |\eta| < 4.8$,as the first η segments overlap with EM endcap detector, and the last η segment has some non-uniformities.

Each of the two fcal detectors can be used to measure the EP. In this analysis, we employed two different, but complimentary ways of measuring the event plane. The first method calculate the raw harmonic flow v_n^{obs} by correlating tracks in $-2.5 < \eta < 2.5$ with the combined EP measured by both both Fcal detectors (**Full-Fcal** EP); one then apply the correction for the full Fcal resolution to obtain the final v_n accoring to Eq. 7. The second method, tracks are correlated with the EP calcualted with the Fcal in the opposite hemisphere, i.e tracks with $\eta \geq 0$ ($\eta < 0$) are correlated with the EP obtained from $Fcal_N$ ($Fcal_P$), known as **Sub-Fcal** EP; one then apply the correction for the Sub-Fcal resolution to obtain the final v_n accoring to Eq. 7. This method is illustrated by Figure 6. This second method greatly increases the rapidity seperation between the tracks and the EP. In comparision with the first method, the average gap is increased from about 3 units to about 5 units in η. Thus the second method is much less affected by the non-flow correlations. This is especially useful for measuring the rapidity dependence of the v_n. The downside with the second method, however, is that it has poor RP resolution, and does not measure the higher order hamornics very well. In this analysis, we present the results from both the Full-Fcal and Sub-Fcal method.

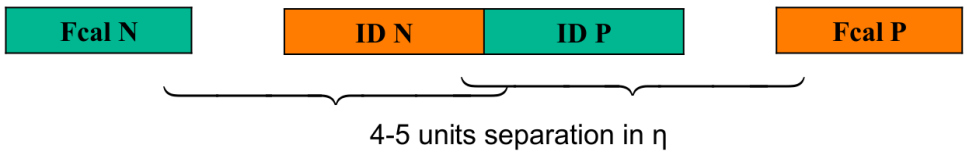

Figure 6: Illustraction of the second EP (Sub-Fcal) method. The tracks at positive hemisphere is correlated with $Fcal_N$ and thos in negative hemisphere with $Fcal_P$.

4.2 Reaction plane calibration

We shall use the Full-Fcal detector to illustrate the calibration procedures. The methodology discussed in section 3 assumes an ideal reaction plane detector, that is the azimuthal anisotropy of the Fcal E_T distribution is caused by the physical flow, instead of detector effects. Since the RP direction varies randomly event to event, such anisotropy should not be correlated with detector geometry, thus should

be averaged out in the ATLAS lab frame. On the other hand, the detector effects such as dead modules or inefficiencies would lead to false modulation of the E_T flow which, after averaged over many events in the lab frame (so real flow drops out), can be expanded into a Fourier series

$$\langle \frac{dE_T}{d\phi} \rangle = Q_0 + 2\sum_{n=1}^{\infty}(\langle Q_{x,n}^{raw}\rangle \cos(n\phi) + \langle Q_{y,n}^{raw}\rangle \sin(n\phi)) = Q_0 + 2\sum_{n=1}^{\infty} \overline{Q_n^{raw}} \cos\left(n(\phi - \Phi_n)\right) \quad (8)$$

where

$$\overline{Q_n^{raw}} = \sqrt{\langle Q_{x,n}^{raw}\rangle^2 + \langle Q_{y,n}^{raw}\rangle^2}, \quad \Phi_n = \frac{1}{n}\tan^{-1}\left(\frac{\langle Q_{y,n}^{raw}\rangle}{\langle Q_{x,n}^{raw}\rangle}\right) \quad (9)$$

Note that $\overline{Q_n^{raw}}$ should be zero for an ideal detector. A non-zero $\overline{Q_n^{raw}}$ would bias the measured event plane towards some fixed direction Φ_n.

Figure 7 shows the event averaged 2-D E_T map, or acceptance function, of Full-Fcal in ϕ and η. Some detector structures are clearly visible. We then project this 2-D distribution onto ϕ axis and expand it into a Fourier series according to Eq. 8. Each Fourier coefficient can be calculated directly via Discrete Fourier Transformation. The left panel of Figure 8 shows the 1-D acceptance function, and the first six Fourier moments plotted individually around the mean values of the histogram, together with the sum of all terms up to $n = 6$ (dashed line). The phases of each n, Φ_n, are drawn as vertical bars on the same figure.The Fcal acceptance function shows a significant modulation for n=1, 2,4 and are relatively small for other moments.

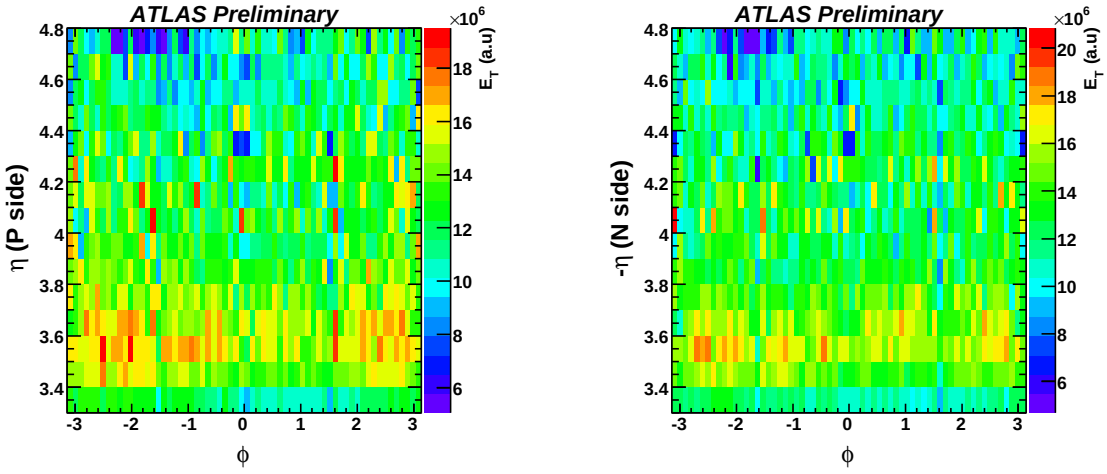

Figure 7: FCal layer 1&2 E_T distribution, intergated from 0-70% centrality range for positive (left) and negative η(right). The first and last η slices centered at $|\eta|$=3.25 and $|\eta|$=4.85 are not used in this analysis and has been excluded from the figures.

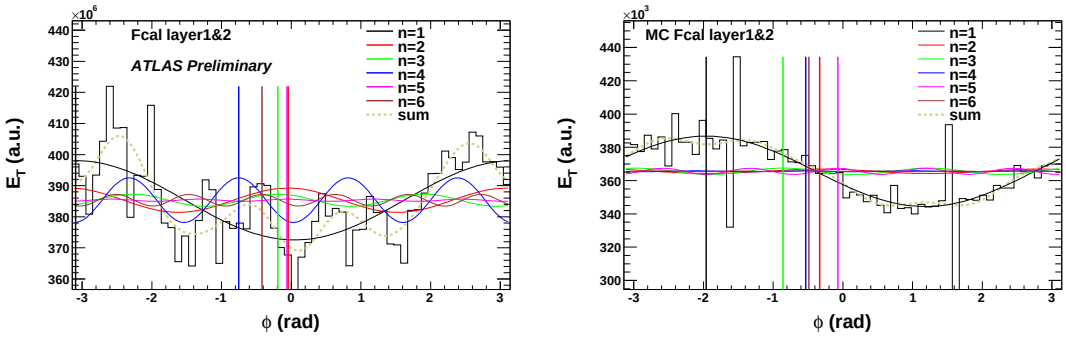

Figure 8: Left: FCal E_T layer 1&2 distribution integrated from 0-70% centrality range and over the η range. Right: same plot obtained from ATLAS GEANT simulations with HIJING.

The right panel of Figure 8 shows the same plot obtained from ATLAS HIJING simulati on, it only shows a significant n=1 component and even that is somewhat out of phase with what is observed from the data. This suggests that more tuning of FCal simulation is required in order to properly represent the structures seen in the data.

To eliminate the EP biases due to detector effects, we use a standard procedure of re-centering and flattening methods employed by the RHIC experiments (see Appendix 7.5). In the re-centering step, the flow vectors are shifted and normalized by its mean and width

$$Q_{x,n} = \frac{Q^{raw}_{x,n} - \langle Q^{raw}_{x,n}\rangle}{\sigma_{Q^{raw}_{x,n}}}, \quad Q_{y,n} = \frac{Q^{raw}_{y,n} - \langle Q^{raw}_{y,n}\rangle}{\sigma_{Q^{raw}_{y,n}}} \tag{10}$$

Any residual high order distortion can be removed using the flattening method, in which the reaction plane angle calculated after the re-centering, $\Psi_n = \tan^{-1}\left(\frac{Q_{y,n}}{Q_{x,n}}\right)$, is corrected by a angle $\delta\Psi_n$ that is a function of the Ψ_n itself:

$$\begin{aligned} \Psi_n &\rightarrow \Psi_n + \delta\Psi_n, \\ n\delta\Psi_n &= \sum_{k=1}^{k_{max}} \frac{2}{k}\left[-\langle\sin(kn\Psi_n)\rangle\cos(kn\Psi_n) + \langle\cos(kn\Psi_n)\rangle\sin(kn\Psi_n)\right] \end{aligned} \tag{11}$$

this procedure basically force the final distribution to be uniform (since the distribution true reaction plane angle is distribution uniform in azimuth.) at a small cost of the resolution[1]. We choose $k_{max} = 10$ in this analysis. We tried other k_{max} values, the results are essentially identical. So we conclude no systematic uncertainty due to choice of k_{max} is necessary.

The detector biases on the EP, if purely due to detector acceptance or inefficiency, should be large independent of the occupancy. On the other hand, the biases could also arise from detector mis-calibrations, such as residual non-linearity or noises that might depend on the occupancy. Also total energy of the Fcal also fluctuate event to event, thus the amount shift $\overline{Q_n^{raw}}$ would also be multiplicity dependent. Thus we apply the re-centering and flattening corrections in 1% centrality bins and then group them into larger centrality bins. These calibration procedure is also done independently for each harmonic plane. Figure 9 shows the second to sixth event plane distributions for FCal with and without the re-centering and flattening calibration. Most of the corrections arises from the a single re-centering procedure, while the flattening step has very little effect. This suggests that the raw Q vector distribution has no additional

[1]There are many ways to make the EP distribution to be flat, each would be supplemented by its own resolution, and subsequently its own measured v_n signal for tracks. In principle one can apply the flattening procedure without re-centering, but that would worsen the resolution.

anomalies other than a simple global shift from origin. Such anomaly would arise, for example, if the detector has higher efficiency at $n\phi$ and $n\phi + \pi$ which would stretch the Q vector distribution to be an elliptic shape pointing to $n\phi$, but has no net shift.

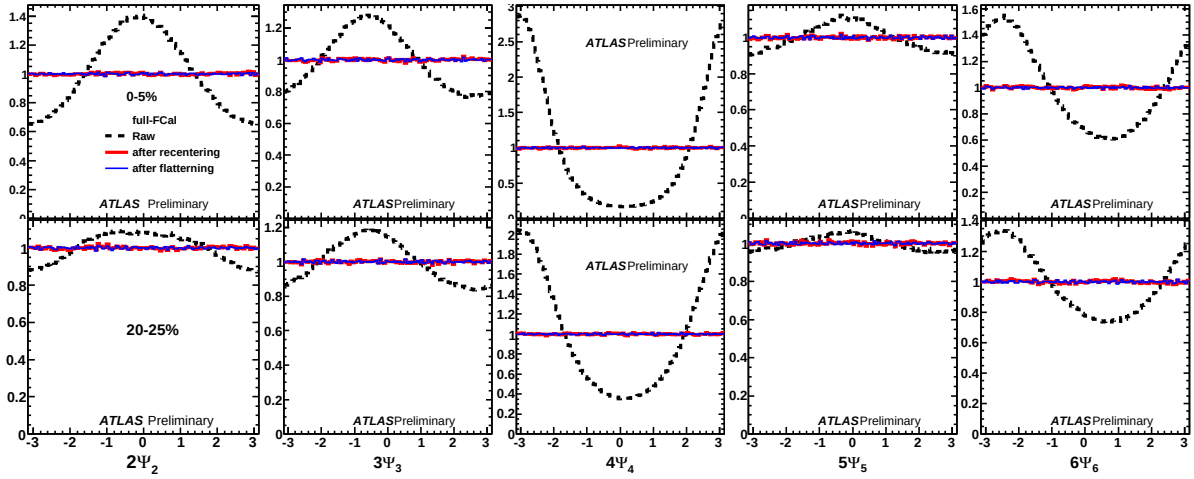

Figure 9: The effects of the reaction plane angle calibration for Full-Fcal detector from $n = 2$ to $n = 6$. A central bin (top) and mid-central bin (bottom) are used. One can see that the most of the calibration arises from the re-centering step.

If the most of the corrections arises from a global shift of the Q vector, it should be correlated among different centrality, Figure 10 shows the $\langle \overrightarrow{Q_n^{raw}} \rangle$ values obtained for $n = 1 - 6$ in 5% centrality bin steps. Left panel show a very nice correlations between directions of the shifts for different centrality selections (the points for given color corresponds to different centrality) for all n values. The relative spacing between the this and next centrality point are also highly correlated among different n values (right panel), suggesting that the magnitude of the shift is proportional to total Fcal transverse energy. This correlation of shift direction between different centrality can be better seen in Figure 11, where we plot directly the magnitude of the shift versus the direction of the shift. We also overlay with the direction obtained directly from Fourier analysis of the E_T map as shown in Figure 8. We see they agree very well with the directions obtained in the calibration procedure. Small deviation does arises in peripheral collisions, especially for $n = 5$. On the other hand, this is the region where the magnitude of the average shift $\langle \overrightarrow{Q_n^{raw}} \rangle$ is less than 1 GeV (usually 100 MeV) where it is start to be sensitive to detector noises and residual calibrations. It is actually amazing to see that we can pick up this centrality dependent detector effects, which is only $\ll 1\%$ level of the total E_T in peripheral collisions.

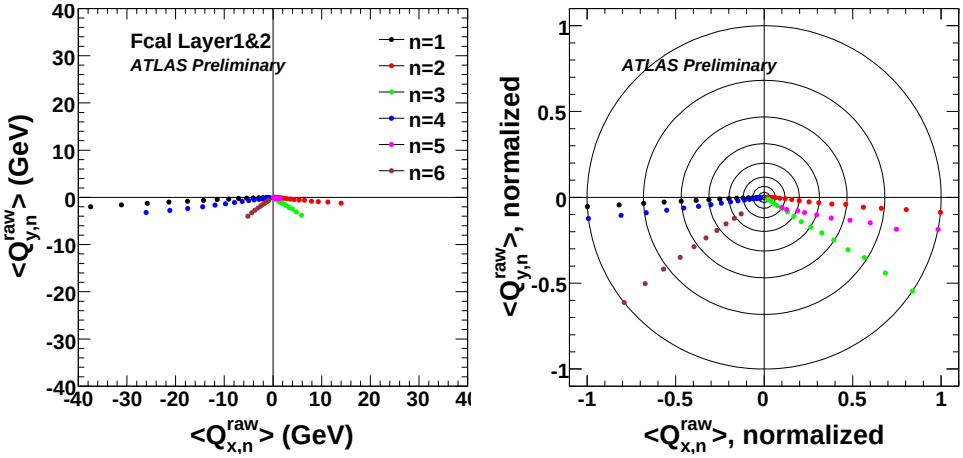

Figure 10: Left: the average flow vector for six harmonic v_1-v_6, each one has 10-18 points each corresponding to a 5% centrality bin. Right: the average flow vector divided by the most central bin 5% result.

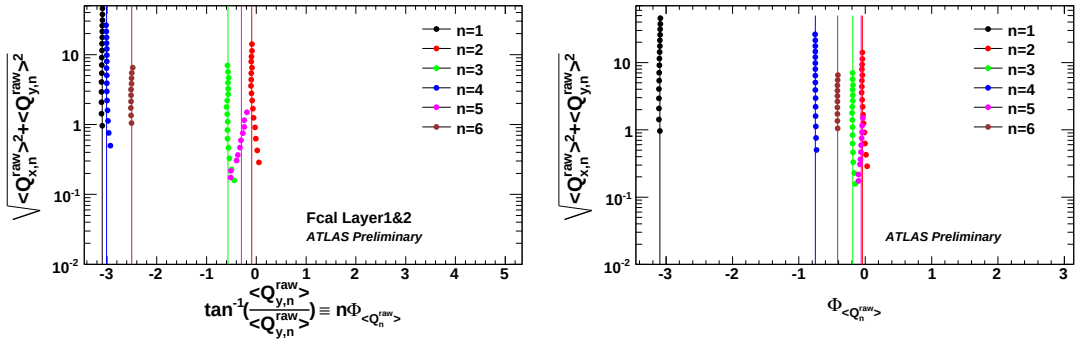

Figure 11: The average flow vector plotted in polar coordinate system (magnitude vs the angle). Left: $n\Phi_n$, right Φ_n. The lines indicates those obtained directly from the E_T map shown in the left panel of Figure 8.

Looking at Figure 11 and 9 together, we can make the following interesting observations. First we see the peak position of the raw event plane direction in 9 are tightly correlated with the direction of the average shift vector , $n\Psi_n$, order by order. However the magnitude of the peak strongly depends on n value. This is because the magnitude of the peak depends on the relative length of the physical flow vector and average shift of the flow vector. The flow vector is largest for $n = 2$ and are small for $n > 4$. On the other hand the magnitude of the average shift, hence the acceptance effect, as shown by the left panel of the Figure11 is large for $n = 4$ and 1, thus they have the strongest effect for Q_1 and Q_4. In the left panel of Figure11, the magnitude of the false flow vector relative to average value ,$\overline{Q^{raw}_{r,n}}/Q_0$, is 1.45%, 0.5%, 0.2%, 1.1%, 0.08%, and 0.25% for $n = 1 - 6$, respectively.

We check the stability of the Fcal detector and its influence on the reaction plane measurement by checking the run by run dependence of $\overline{Q^{raw}_{r,n}}$ and Ψ^{raw}_n. They are shown in Figure 12. As one see they are stable throughout the runs.

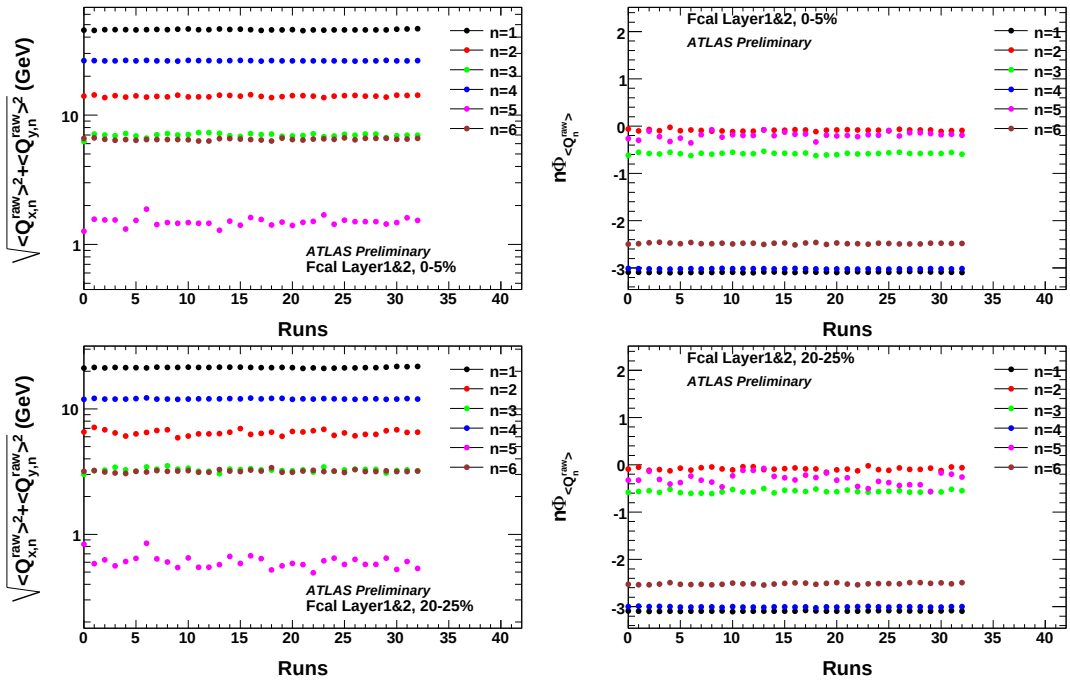

Figure 12: Run dependence of the average shift in Q vectors for 0-5% (top panels) and 25-30% (bottom panels) centrality selections.

After the calibration is applied, the Q vector angle should be uniformly distributed in the transverse plane, centered at the origin. One can think it as a vector with finite length rotating randomly event by event around the origin (thus the mean value of the x,y projections should be zero). Thus when the resolution is good, the Q vector distribution should appear a ring centered around origin as illustrated by Figure13. The magnitude of the Q vector relative to the width of the ring, reflects the precision with which we can measure the Q vector. This ratio is called χ, and directly relates to the resolution factor Res$\{\Psi_n\}$. Figure 14 shows the Q vector distribution obtained from data for the full Fcal detector for $n = 2$. We clearly see that the mean radial position of Q vector is non zero and random orientation gives rise to the ring like structure. This is the first time that we have ever seen a ring like structure in Heavy ion collisions, thanks to the excellent detector resolution provided by the ATLAS. The method of determining the reaction plane resolution is centered around calculating the values of χ and estimating the associated systematic errors.

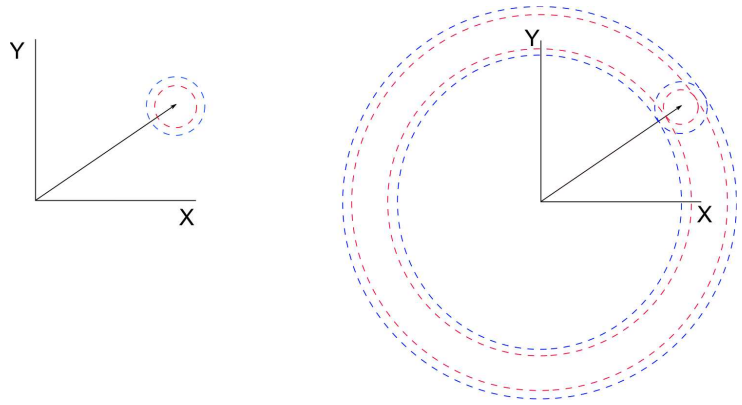

Figure 13: Cartoon showing the Q vector that has finite length but random orientation.

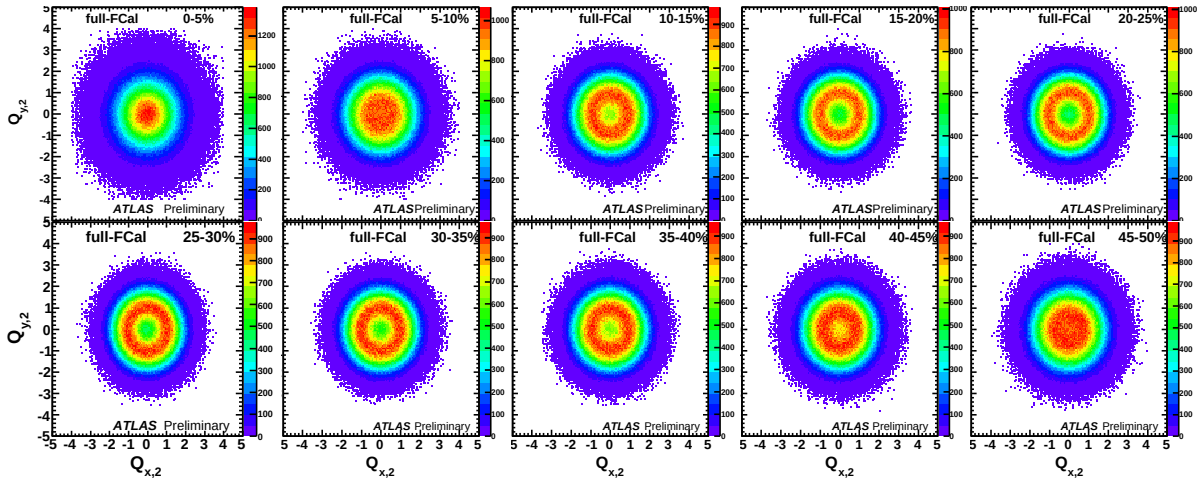

Figure 14: The experimentally measured Q vector distributions from Full-FCal for $n = 2$ and several centrality selections, they are normalized according to Eq.10

.

4.3 Methods for calculating reaction plane resolution

All the results in this section are derived in the appendix section 7.6. Here we just mention the final formulae. As mentioned earlier, χ is the single most important parameter in determining the resolution correction. Since it is given by the ratio of strength of the flow divided by the fluctuation term, we expect χ is proportional to average flow strength of each and the square root of number of particles in the Fcal acceptance.

$$\chi \propto v_n \sqrt{N} \tag{12}$$

It was shown that if fluctuations of the spread particle flow around the mean value is Gaussian, the resolution factor for a detector is related to the χ value as (see Eq. 61) :

$$\mathrm{Res}\{\Psi_n\} = \langle \cos n\Delta\Psi_n \rangle = \frac{\chi\sqrt{\pi}}{2} e^{-\frac{\chi^2}{2}} \left[I_0(\frac{\chi^2}{2}) + I_1(\frac{\chi^2}{2}) \right]. \tag{13}$$

χ can be obtained from the **two-sub-event method**, which divides a given reaction plane detector into two sub-detectors covering equal but opposite η ranges, one in positive and one in negative hemisphere,

such that the two sub-detectors have the same resolution. The symmetry in η between the positive and negative side of Fcal provide such a natural division. The distribution of difference of the two event plane angles, $\Psi'_n = \Psi^P_n - \Psi^N_n$, can be parametrized with an analytical function of the sub-detector $\chi_{sub}(= \chi/\sqrt{2})$ as (see Eq.63) :

$$\frac{dN}{d\Delta n\Psi'_n} = \frac{e^{-\chi^2_{sub}}}{2}\left[\frac{2}{\pi}(1+\chi^2_{sub}) + z(I_0(z)+L_0(z)) + \chi^2_{sub}(I_1(z)+L_1(z))\right] \tag{14}$$

Where $z = \chi^2_{sub}\cos(n\Delta\Psi'_n)$, I_n is the modified Bessel functions of the first kind and L_n is the modified Struve function.

We can derive χ value directly by fitting the measured $dN/d\Delta\Psi'_n$ distribution; or we first calculate the sub-event resolution from $dN/d\Delta\Psi'_n$ distribution (see Eq.68):

$$\langle\cos(n[\Psi^{P(N)}_2 - \Psi_{\mathrm{RP,n}}])\rangle = \sqrt{\langle\cos(n[\Psi^P_n - \Psi^N_n])\rangle},$$

This resolution can be directly used in the Sub-Fcal v_n analysis. However if we want to do the Full-Fcal v_n analysis, we need to calculate the χ_{sub} value for the sub-event with Eq.13, and then obtain the full event χ as $\chi = \sqrt{2}\chi_{sub}$. Once χ is obtained, we then plug back it into Eq.13 to obtain the full event resolution.

The two-sub-event method has the disadvantage that it relies on the assumption that the two sub-detectors have the same resolution. The second method, known as **three-sub-event method**, calculates $\mathrm{Res}\{\Psi_\mathrm{n}\}$ of a given detector A directly from the correlation of its event plane with those of two other detectors sitting at different η windows B and C,

$$\mathrm{Res}\{\Psi^A_n\} = \langle\cos(n(\Psi^A_n - \Psi_{\mathrm{RP,n}}))\rangle = \sqrt{\frac{\left\langle\cos\left(n\left(\Psi^A_n - \Psi^B_n\right)\right)\right\rangle\left\langle\cos\left(n\left(\Psi^A_n - \Psi^C_n\right)\right)\right\rangle}{\left\langle\cos\left(n\left(\Psi^B_n - \Psi^C_n\right)\right)\right\rangle}} \tag{15}$$

We denote the resolution obtained this way as A-B-C three-sub-event method. The three-sub-event method does not require to determine the χ, instead $\mathrm{Res}\{\Psi^A_n\}$ is obtained directly, one can then calculate the χ using Eq. 13. The second advantage of the three-sub-event method is that, for a given detector A, we can have many choices of B and C, which provide independent estimates. The drawback though is that the precision with which one can determine the $\mathrm{Res}\{\Psi_\mathrm{n}\}$ now also depends on the reference detectors we choose, that is, if we choose reference detectors with poor resolution, then the $\mathrm{Res}\{\Psi_\mathrm{n}\}$ obtained would have large systematic errors.

We now present results from the two-subevent and three-subevent studies of reaction plane resolution for both the Full-Fcal and Sub-Fcal.

4.4 Resolution from two-sub-event method

In Fig.15 we show some of the $\Psi_P - \Psi_N$ distributions for the FCal. Also shown are the fits to the functional form in Eq.14. One can obtained the Sub-Fcal resolution either from fit (obtain χ_{sub} then use Eq.68) or calculate it directly via Eq. 15. For the Full-Fcal resolution, we first calculate the χ_{sub} directly from the Eq 15 or obtain it from this fit. After that the $\chi = \sqrt{2}\chi_{sub}$ for Full-Fcal is calculated, and its resolution can be obtained from Eq.68.

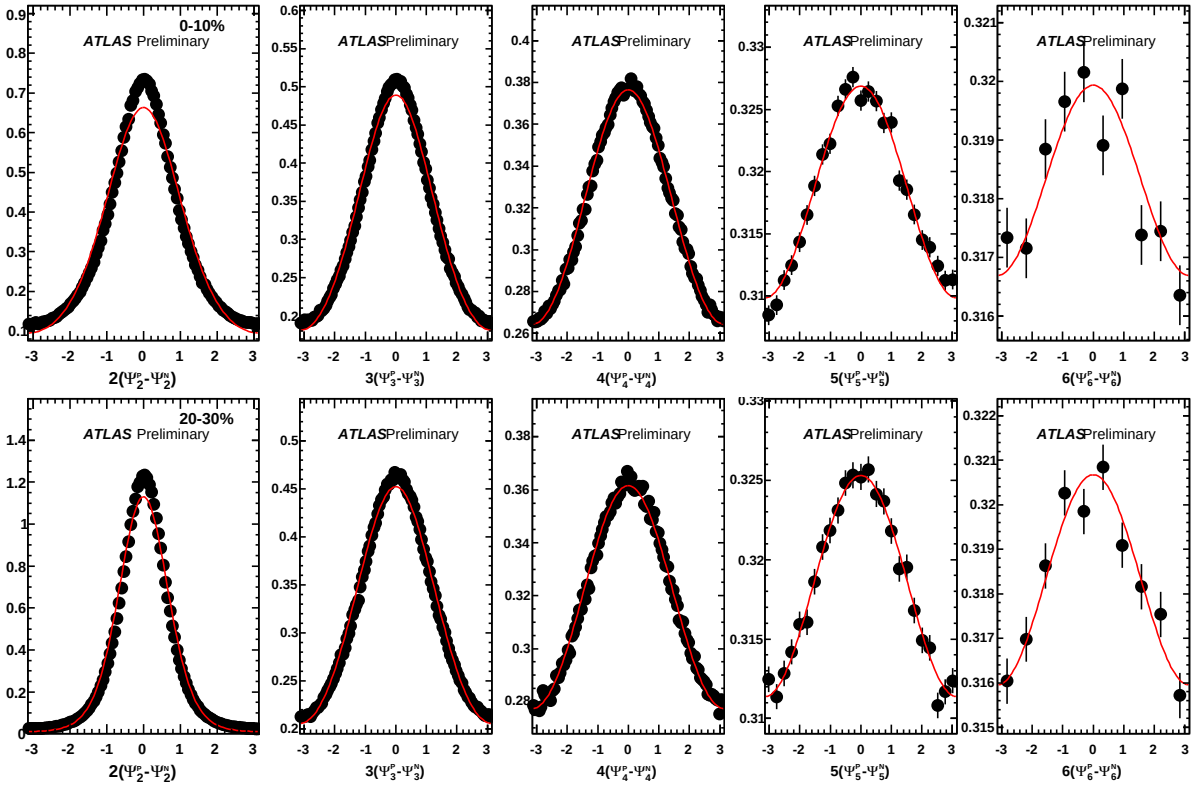

Figure 15: $\Psi_P - \Psi_N$ distributions for FCal for two different 10% centrality bins. Also shown is the fit to the functional form in Eq.14 used to obtain the value of χ_{sub}

Figure 16 show the ratio of the full-Fcal resolution obtained using these two slightly different approaches; the same comparison for sub-Fcal resolution is shown in Figure 17. The results agree with each other very well for all n, only a 0.5% (1%) systematic deviation is observed for $n = 2$ in mid-central collisions for Full-Fcal(Sub-Fcal), with the fitting method giving a higher value. This is the region where $\Psi_P - \Psi_N$ distribution deviates from the fit. We shall include this difference in the final systematic error table.

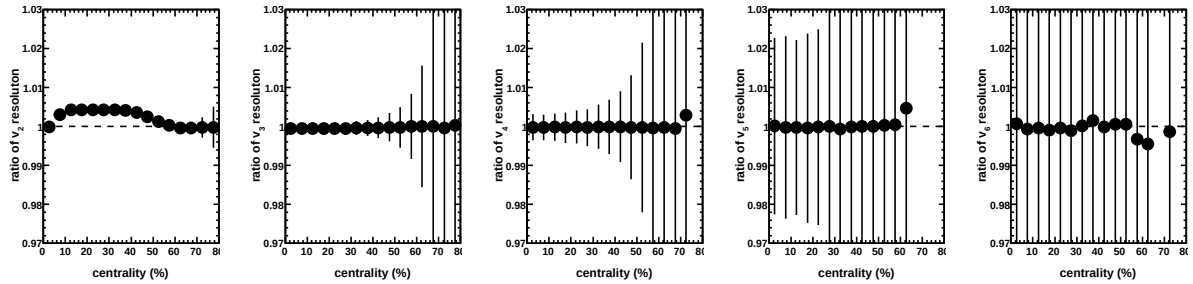

Figure 16: The ratio of the full Fcal resolution for two methods of obtaining full Fcal χ: fitting of the two sub-event distribution or calculating via Eq 15 .

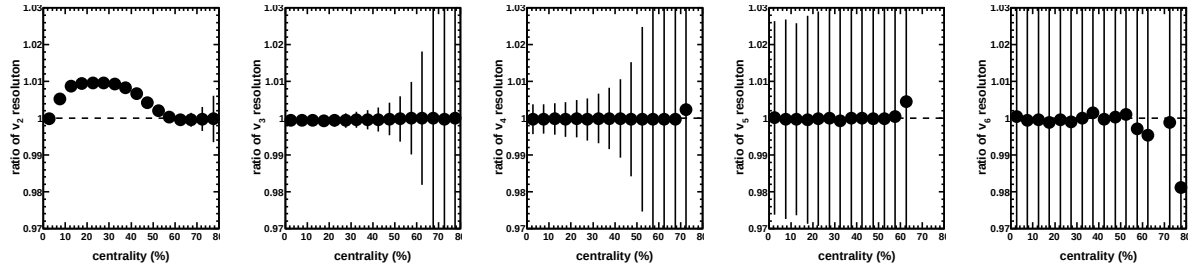

Figure 17: The ratio of the Sub-Fcal resolution between fitting of the two sub-event distribution or calculating directly via Eq 15 .

The two sub-event method is our main method for obtaining the χ and hence the resolution of the FCal. The resolution that we obtain from this method is the resolution that we use to calculate our final results. However, we have carried out a detailed study of three-sub-event method to estimate the systematic uncertainty associated with the FCal resolution.

4.5 Resolution from three-sub-event methods

As we said earlier, the main advantage of three-sub-event method is that

- It makes no assumptions about the functional form of the dispersion distribution of Ψ_n relative to $\Psi_{RP,n}$.
- We can directly calculate the resolution of the full FCal, as opposed to the two sub-event method, which gave us the resolution of the sub-detector ($FCal_P/FCal_N$) which we used to obtain the full resolution

On the other hand, the three detectors has to be well separated in η in order to minimize the auto-correlations. also the reference detector (B and C) themselves must have good resolution, otherwise the resolution for detector A obtained from this method would have large statistical and systematic error.

4.5.1 Detectors used for three sub-event study

The large coverage of the ATLAS Electro-magnetic Calorimeter (EMCal) system, including Barral EM-Cal ($|\eta| < 1.5$) and Endcap ($1.5 < |\eta| < 3.2$) with fine segmentation, allows a very flexible choices of the B and C. For the three-sub-event study, we choose the EM barrel calorimeter (denote as EMB), EM endcap calorimeter (denote as EMC), and tracks from Inner detector (denote as ID) as the nominal set of reference detectors. These detectors are then divided into a set of sub-detectors each covering 0.5 unit in η. In total we have 22 calorimeter segments and 10 inner detector segments. Their relative positions in η are illustrated by Figure 18. The naming convention for the detectors used are listed in Table 2. The names refer to detector with both the positive η and negative η segments. When just one side is used we add a subscript, for example EMB_N would refer to the EMcal barrel detector on the negative η.

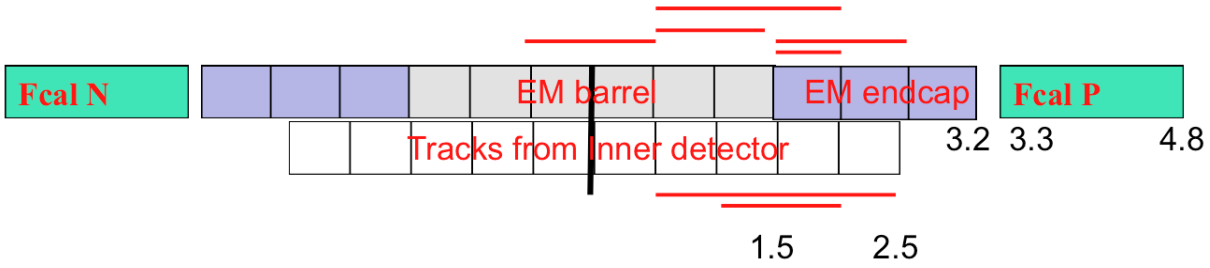

Figure 18: A schematic representation of the detectors(besides the FCal) used in the three sub-event calculations. See Table.2 for the descriptions. The detectors are represented by red-lines. The other two detectors are : EMB (all grey boxes) EMEC (all purple boxes).

Detector	Name	Description	$\|\eta\|$ coverage	Calorimeter-Layers
1	EMB0	EMcal Barrel	0-0.5	presamp+layer1,2
2	EMB1	EMcal Barrel	0.5-1.5	presamp+layer1,2
3	EMB2	EM Barrel	0-1.5	sum of Detectors 1 and 2
4	EME0	EMcal End Cap	1.5-2.1	presamp+layer1,2
5	EME1	EMcal End Cap	1.5-2.7	Detector 4 +
				presamp+layer1,2,3 for $2.1 < \eta < 2.7$
6	EME2	EMcal End Cap	1.5-3.2	Detector 4+
				presamp+layer1,2 for $2.7 < \eta < 3.2$
7	EMB1EME0	EM Barrel + End Cap	0.5-2.1	sum of Detectors 2 and 4
8	ID0	Inner Detector	0.5-2.0	charged particles $p_T > 0.5$ GeV
9	ID1	Inner Detector	0-2.5	charged particles $p_T > 0.5$ GeV

Table 2: Detectors used in the three sub-event method to determine Full-FCal and Sub-Fcal resolution. If only one side of the detector is used, we use a substript “N” or “P” to indicate the either negative or the positive η.

4.5.2 Three types of three-sub-event studies

To suppress the short range correlations, a minimum 1 unit separation in choosing the three detectors. We have performed many three-sub-event studies, and they can be roughly divided in to three types. In Type-I analysis, A is chosen to be the Full Fcal, and B and C are chosen such as to be symmetric in + and - η, one example is $|\eta| < 0.5$ for B and $1.5 < |\eta| < 2.0$ for C. The list of combinations used are listed in Table 3.Note the choice of B and C are such that they totally symmetric with respect to $Fcal_N$ and $Fcal_P$. The advantage of this type is that we can calculate the resolution for full-Fcal directly. However by definition this method is not designed for Sub-Fcal method.

Type-I checks	
Check1	FCal – EMB0 – EME0
Check2	FCal – $EMB1_P$ – $EMB1_N$
Check3	FCal – $EMB1EME0_P$ – $EMB1EME0_N$
Check4	FCal – $EME0_P$ – $EME0_N$

Table 3: A list of Type-I combinations, they can only be used for Full-Fcal resolution. See Table.2 for description of the detectors.

Fig.19 shows the Full-Fcal resolution for $n = 2 - 6$ obtained for the *Fcal* for various Type-I combinations as a function of centrality. We also show the resolution obtained from the two sub-event method. The different combinations have been given small offsets on the x-axis so that they can be clearly seen. Fig.20 shows the ratios to the two-sub-event method results. For $n = 2$, the ratios is systematicall below one in central collisions by up to 5% and then become about 1% in mid-central collisions, then the ratio spread out in peripheral collisions by about ±5%. For $n = 3$ and 4, we see a small systematically increasing trend of the ratio towards peripheral collisions, but the change is within 3%. For $n = 5$, the ratio is systematicall above one and increases toward more peripheral collisions to about 5-10%. For $n = 6$, we see there is a large spead of the ratios with about ±30% variation, and in some cases, the ratio is systematically lower than 1.

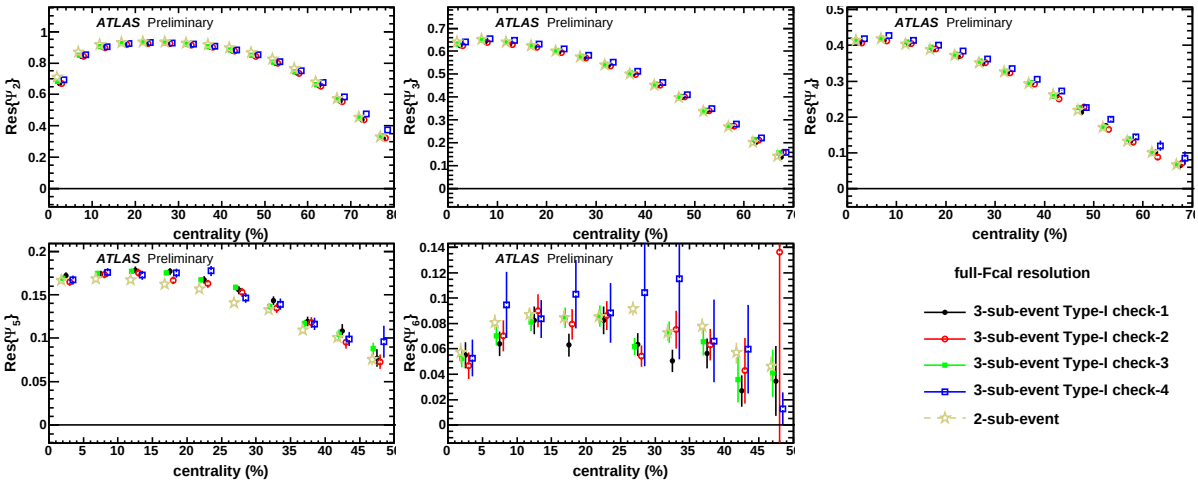

Figure 19: The full-fcal resolutions for $v_2 - v_6$ obtained for the full *Fcal* from Type-I combinations. The full-fcal resolution obtained from the two sub-event method is also shown for comparison. Error bars are statistical only.

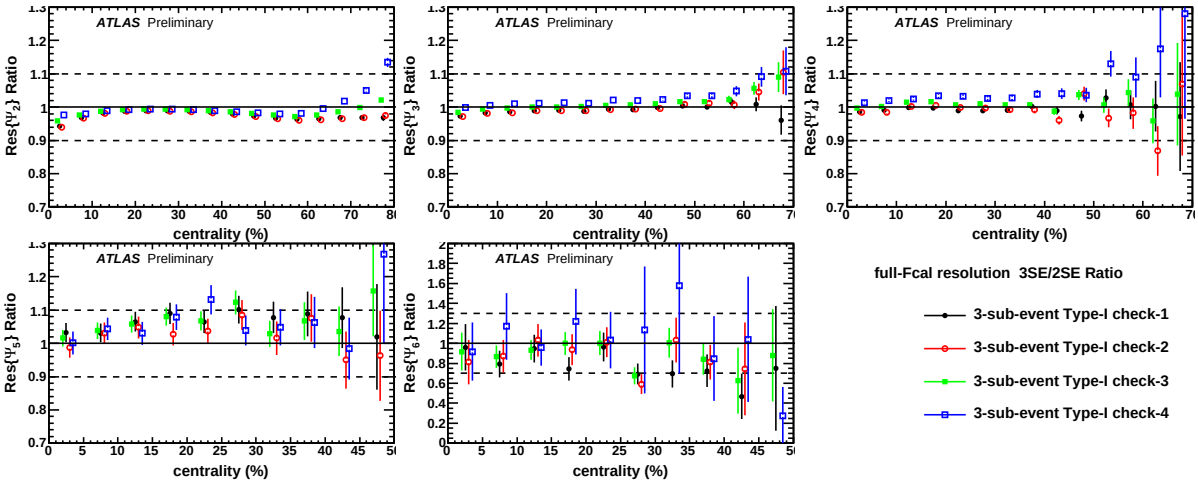

Figure 20: The ratio of Full-Fcal resolutions for $v_2 - v_6$ obtained for the full $FCal$ from Type-I combinations to the ones obtained from the two sub-event method. Error bars are statistical errors. The vertical dashed red line indicates the centrality range over which we will quote our final results.

In Type-II analysis, we chose A and B as FcalN and FcalP, and chose C from the list of reference detectors. Detectors C has an η separation > 1 form both $Fcal_{P/N}$ and is symmetrically placed in between them. This allow us to calculate the resolution for $Fcal_P$ from Eq. 15. We then swap the A and B while keep the same C and calculate the resolution for $Fcal_N$. We then calculate χ values for the FcalN and FcalP according to Eq 13, then combine them to get the full Fcal $\chi = \sqrt{\chi^2_{Fcal_N} + \chi^2_{Fcal_P}}$. Finally use Eq 13 again to obtain the resolution for Full-Fcal. In total 5 Type-II checks were performed as listed in Table 4. Note that since $Fcal_P$ or $Fcal_N$ resolution is calculated at the intermediate step, it can also used for the Sub-Fcal method.

Type-II checks	
Check1	$\mathrm{FCal_N} - \mathrm{EMB0} - \mathrm{FCal_P}$ and $\mathrm{FCal_P} - \mathrm{EMB0} - \mathrm{FCal_N}$
Check2	$\mathrm{FCal_N} - \mathrm{EMB1} - \mathrm{FCal_P}$ and $\mathrm{FCal_P} - \mathrm{EMB1} - \mathrm{FCal_N}$
Check3	$\mathrm{FCal_N} - \mathrm{EME1} - \mathrm{FCal_P}$ and $\mathrm{FCal_P} - \mathrm{EME1} - \mathrm{FCal_N}$
Check4	$\mathrm{FCal_N} - \mathrm{EMB2} - \mathrm{FCal_P}$ and $\mathrm{FCal_P} - \mathrm{EMB2} - \mathrm{FCal_N}$
Check5	$\mathrm{FCal_N} - \mathrm{EMB1EME0} - \mathrm{FCal_P}$ and $\mathrm{FCal_P} - \mathrm{EMB1EME0} - \mathrm{FCal_N}$

Table 4: A list of Type-II combinations, they can be used to calulate resolution for both the Full-Fcal and Sub-Fcal. See Table 2 for description of the detectors.

This method is similar to the two-sub-event method, as one can see from the following equation,

$$\mathrm{Res}\{\Psi_n^{Fcal_P}\} = \sqrt{\frac{\left\langle \cos\left(n\left(\Psi_n^{Fcal_P} - \Psi_n^B\right)\right)\right\rangle \left\langle \cos\left(n\left(\Psi_n^{Fcal_P} - \Psi_n^{Fcal_N}\right)\right)\right\rangle}{\left\langle \cos\left(n\left(\Psi_n^{Fcal_N} - \Psi_n^B\right)\right)\right\rangle}} \quad (16)$$

$$\mathrm{Res}\{\Psi_n^{Fcal_N}\} = \sqrt{\frac{\left\langle \cos\left(n\left(\Psi_n^{Fcal_N} - \Psi_n^B\right)\right)\right\rangle \left\langle \cos\left(n\left(\Psi_n^{Fcal_P} - \Psi_n^{Fcal_N}\right)\right)\right\rangle}{\left\langle \cos\left(n\left(\Psi_n^{Fcal_P} - \Psi_n^B\right)\right)\right\rangle}} \quad (17)$$

In fact $\cos\left(n\left(\Psi_n^{Fcal_N} - \Psi_n^B\right)\right)$ and $\cos\left(n\left(\Psi_n^{Fcal_P} - \Psi_n^B\right)\right)$ would cancel out with each other if their resolution are the same, and the end results would be identical to the two-sub-event formula Eq. 15. However

the main advantage here is that we do not need to assume the FcalN and FcalP to have same resolution explicitly.

Fig.21 shows the ratio of Full-Fcal resolutions for $n = 2 - 6$ obtained for $Fcal$ from Type-II combinations to the ones obtained from the two sub-event method as a function of centrality. Same ratios are also shown for Sub-Fcal resolutions in Figure 22. We see that agreement for Full-Fcal are very good for all harmonics and we do not see any systematic variation of the ratios with centrality. The only noticible difference is about 1% downward shift of the ratios for $n = 3$ and 5, and a 2% downward shift of the ratios for $n = 4$. The agreements for the Sub-Fcal resolutions are even better for all harmonics, and we do not see any visible differnces. This suggest the assumption assumption made in the two sub-event method that $Fcal_P$ and $FCal_N$ have identical resolution is justified.

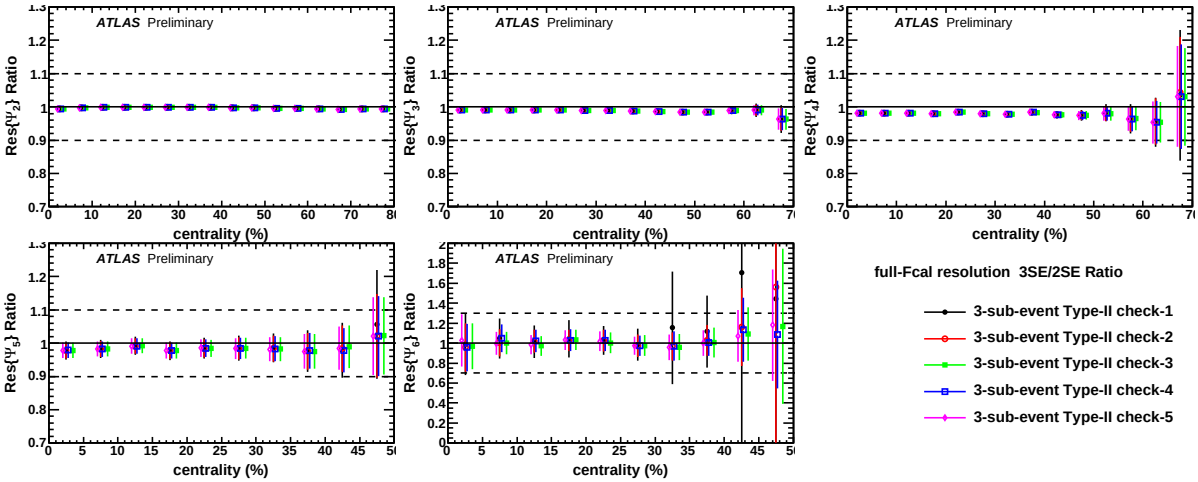

Figure 21: The ratio of Full-Fcal resolutions for $v_2 - v_6$ obtained for $FCal_p$ from Type-II combinations to the ones obtained from the two sub-event method. Error bars are statistical errors.

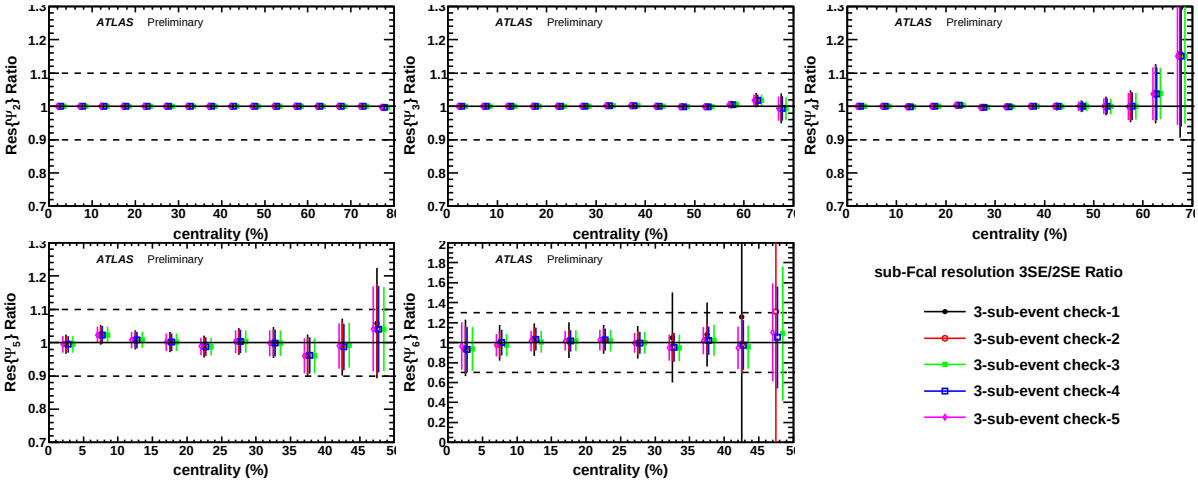

Figure 22: The ratio of Sub-Fcal resolutions for $v_2 - v_6$ obtained for $FCal_p$ from Type-II combinations to the ones obtained from the two sub-event method. Error bars are statistical errors.

In Type III analysis, the Sub-Fcal resolution is calculated for two sides of Fcal separately in two separate three sub-event studies, and then combined according to the standard formula Eq.13 and 15 that relates the two sub-detector resolution to the the full detector resolution. Note that detectors B and C

are any two detectors that have an η separation greater than 1.0 from the first detector ($FCal_p$ or $FCal_n$) and from each other. The main difference from Type-II check is that the reference detector B and C are chosen to be just half at either P or N side, but the choice are total symmetric for the two cases. As listed in Table 5, a total of 6 Type-III checks were performed. Again since $Fcal_P$ or $Fcal_N$ resolution is calculated at the intermediate step, it can also used for the Sub-Fcal method.

Type-III checks	
Check1	$FCal_P - EMB2_P - EME2_N$ and $FCal_N - EMB2_N - EME2_P$
Check2	$FCal_P - EMB1_P - EME2_N$ and $FCal_N - EMB1_N - EME2_P$
Check3	$FCal_P - EMB1EME0_P - EMB1EME1_N$ and $FCal_N - EMB1EME0_N - EMB1EME1_P$
Check4	$FCal_P - EMB1EME0_P - ID0_N$ and $FCal_N - EMB1EME0_N - ID0_P$
Check5	$FCal_P - ID1_P - EMB1EME0_N$ and $FCal_N - ID1_N - EMB1EME0_P$
Check6	$FCal_P - ID0_P - EME_N$ and $FCal_N - ID0_N - EME_P$

Table 5: A list of Type-III combinations where either $Fcal_P$ or $Fcal_N$ is chosen as the first detector (but they are not used at the same time as in Type-II case). They can be used to calulate resolution for both the Full-Fcal and Sub-Fcal. See Table 2 for description of the detectors.

Figure 23 shows the ratio of Full-Fcal resolutions for $n = 2 - 6$ obtained for $Fcal$ from Type-III combinations to the ones obtained from the two sub-event method as a function of centrality.We see extremely good agreement with the two sub-event values for $n = 2$ except in peripheral events. For $n = 3$ and $n = 4$, the three sub-event values are systematically higher than the two sub-event values but are within $\sim 4\%$ in the chosen region. For $n = 5$, we see that the ratio is systematically larger than one by about 10% in peripheral collisions, For $n = 6$, the three-sub-event results are now systematically lower than those obtained from two-sub-event methods by as much as 30% in mid-central and peripheral collisions. Same ratios for Sub-Fcal resolutions are shown in Figure 24, the systematic trends as function of centrality are quite similar as the Full-Fcal case. However we see that the deviation for n=2, 3 and 4 are somewhat larger (but remains independent of centrality), reaching about 5% for both n=3 and n=4. The level of deviation for n=5 and 6, however are quite similar to that for the Full-Fcal case.

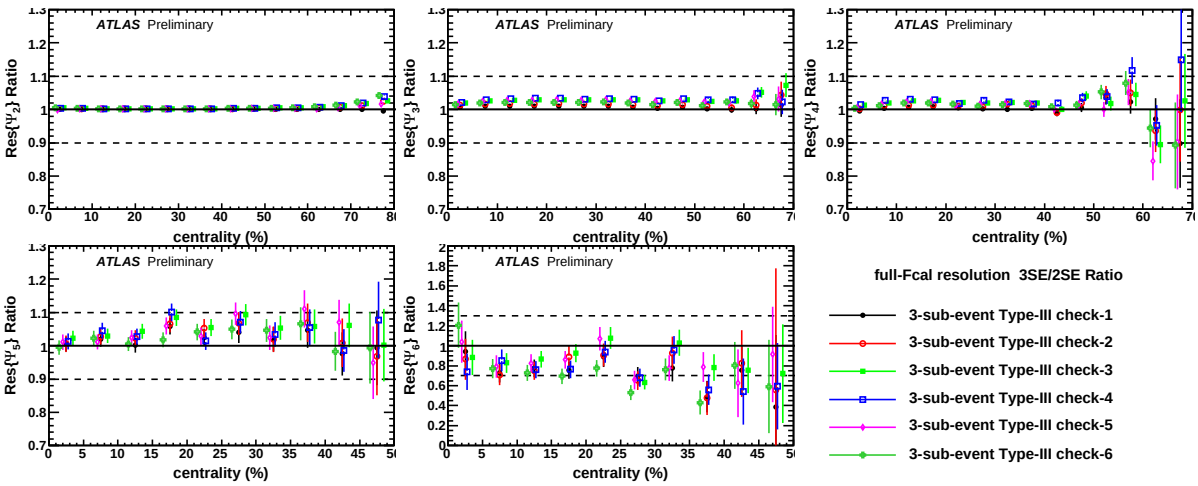

Figure 23: The ratio of Full-Fcal resolutions for $v_2 - v_6$ obtained for $FCal_p$ from Type-III combinations to the ones obtained from the two sub-event method. Error bars are statistical errors.

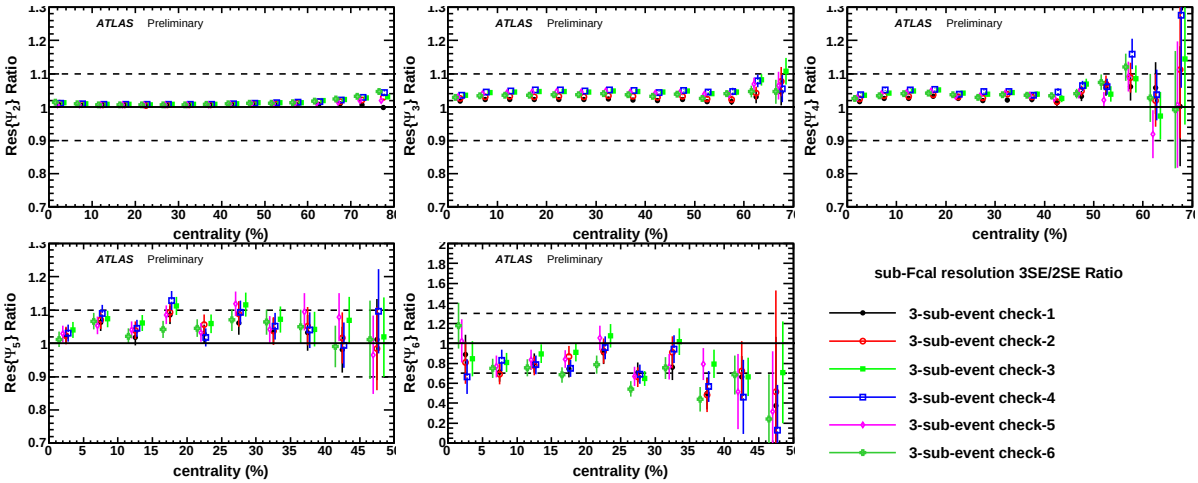

Figure 24: The ratio of Sub-Fcal resolutions for $v_2 - v_6$ obtained for $FCal_p$ from Type-III combinations to the ones obtained from the two sub-event method. Error bars are statistical errors.

To put all these results together we compiled an systematic error table in Table 6. The error are chosen, such that it covers the systematics for both the Full-Fcal and Sub-Fcal methods. In general, the spread of these different estimates is less than 5% for $n = 2 - 4$, grow to about 5-7% for $n = 5$ and about 30% for $n = 6$. To account for the systematic and sizable difference between the three and two sub-event methods for $n = 5$ and 6, we apply a 5% upward correction for $n = 5$ and a 15% downward correction for $n = 6$ on the two-sub-event resolution to particially account for this systematic differences. Also note that the size of the speard between three and two sub-event method also determine the range in centrality we used to present our final results. It is 0-80% for v_2, 0-70% for v_3 and v_4, and 0-50% for v_5 and v_6 beyond which the error becomes too large.

centrality	0-20%	20-40%	40-50%	50-70%	70-80%
n=2	0.05-0.02	0.015-0.01	0.015-0.02	0.03-0.04	0.04-0.06
n=3	0.03	0.03	0.03	0.03-0.05	
n=4	0.04	0.04	0.04	0.04-0.05	
n=5	0.1	0.1	0.1		
n=6	0.3	0.3	0.3		

Table 6: Summary of the systematic errors for the reaction plane resolutions for both Full-Fcal and Sub-Fcal method.

Figure 25 summarize the Res$\{\Psi_n\}$ and χ values together with the systematic errors for the Full-fcal detector. similar plot for the Sub-Fcal detector is shown in Figure 26. Note that the statistical errors on the Full-fcal and Sub-Fcal resolution are almost identical, as they are all derived from the same two-sub-event resolution (but the error on v_n^{obs} is larger for sub-fcal than for Full-fcal).

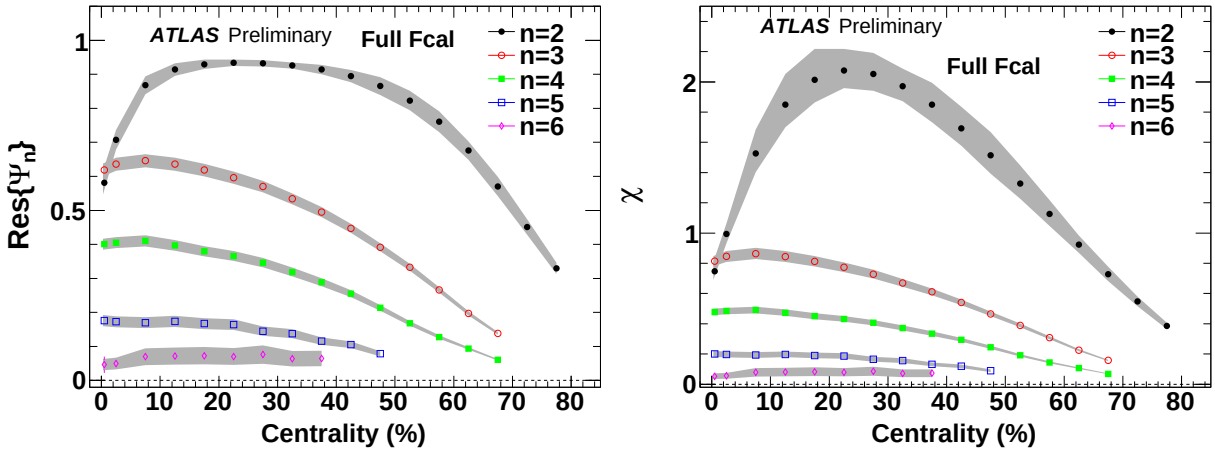

Figure 25: The final resolution (left) and χ (right) values for the full-Fcal detector together with the syetmatic error band.

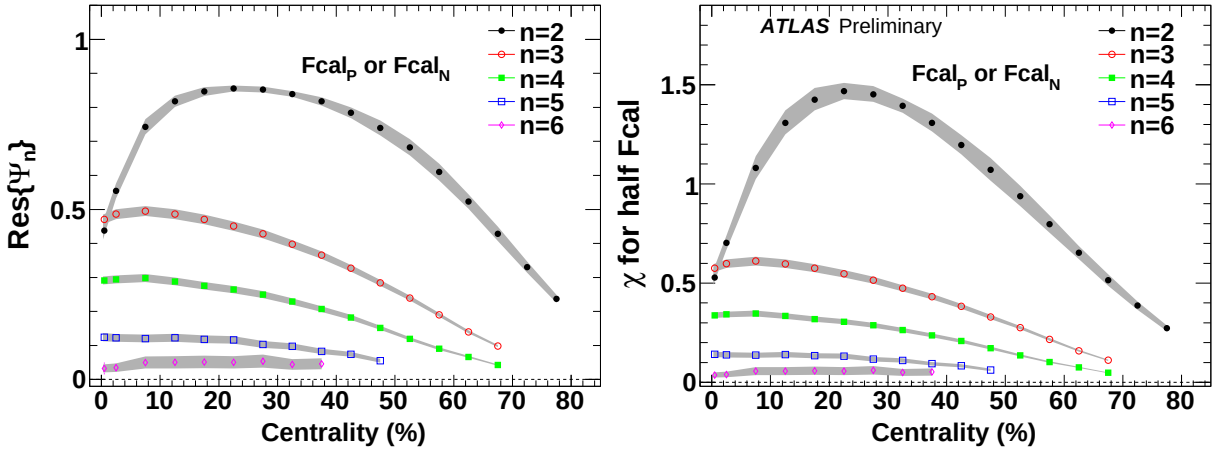

Figure 26: The final resolution (left) and χ (right) values for the sub-Fcal detector together with the syetmatic error band.

4.6 Determination of the raw v_n (v_n^{obs})

In this section, we describe how the raw v_n (v_n^{obs}) is calculated, and we shall use the Full-Fcal to illustrate the procedure. As explained in the Appendix (7.3), the v_n^{obs} is the value of the n^{th} order harmonic calculated by directly measuring the distribution of the particles about the n^{th} order event plane. This has to be corrected by the reaction plane resolution to obtain the true v_n value.

For each event, we calculate the corrected event plane angle Ψ_n for a given reaction plane detector. Then we bin the azimuthal angle relative to the EP ($\Delta\phi = \phi - \Psi_n$) and obtain the distribution $dN/d(n\Delta\phi)$. Note that we multiply by n such that the full distribution is a even periodical function with a unit range from $-\pi$ to π. Examples of such distribution in 2nd, 3rd and 4th event plane (folded one more time into $0-\pi$ since it is an even function) are shown in Figure 27. We have 48 bins from in plane ($n\Delta\phi = 0$) to the out of plane direction ($n\Delta\phi = \pi$). The raw flow signal can be obtained by expanding the distribution with a Fourier series.

$$dN/d\Delta\phi = A(1 + 2v_n^{obs}\cos n\Delta\phi + 2v_{2n}^{obs}\cos 2n\Delta\phi + ..) \quad (18)$$

Where $\Delta\phi = \phi - \Psi_n$. However, instead of a least chi square fit, we calculate the Fourier coefficients directly via Discrete Fourier Transformation (DFT) as :

$$v_{kn}^{obs} = \frac{\sum_{i=0}^{48} C_i \cos kn\Delta\phi_i}{\sum_{i=0}^{48} C_i}, k = 1, 2, 3.. \tag{19}$$

where C_i is the number of counts in a given $\Delta\phi_i$ bin, a small bin shift correction has been applied as well.

Note that higher order harmonic flow can appear at lower order event plane due to physical correlations between different order of plane. In general, one can measure knth order flow in n^{th} order plane where $k = 1, 2, 3.....$ This higher moments in a fix order plane are so called mixed harmonics, which is not a topic of current study. We just show its existance in the harmonics parameterization

$$dN/d\phi \propto 1 + 2\sum_{k=1}^{\infty} v_{kn} \cos kn(\phi - \Psi_n) \tag{20}$$

See the appendix (section 7.4) for a brief discussion on the mixed harmonics.

We noticed that the mean $\Delta\phi$ of charged hadron in a given bin is not necessarily located at the center of the bin. This leads to a bin shift correction, defined as the ratio of the average yield to the expected yield at the bin center. This correction is << 1% for k value up to 3, but we nevertheless applied it. The final v_{kn} is then obtained by applying the resolution correlation as $v_{kn} = \frac{v_{kn}^{raw}}{\mathrm{Res}(\Psi_{k|n})}$ for each centrality and p_T selections and values of k and n.

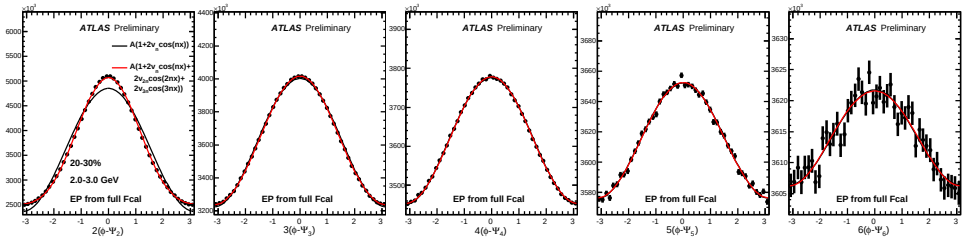

Figure 27: The azimuthal distribution of charged particles in 2-3 GeV/c relative to the Ψ_n determined by the FCal12 for 20-30%.

To see the contributions from different order of mixed harmonics to the $\Delta\phi$. We calculate the expected distributions using the valued v_{kn} values but truncated the formula Eq. 18 to include only the first few harmonics. The red line in Figure 27 shows the distribution including only the lowest order (k=1) term, i.e. only the v_n term in n^{th} harmonic plane, while the black line include the contributions up to k=3. We can see that the mixed harmonic contribution in the 2nd order event plane is clearly required. However higher order contribution in the 3rd order event plane is already very small, and it becomes negligible in the 4th order event plane.

4.7 Residual $\langle \sin(n\phi - \Psi_n) \rangle$ values in Ψ_n plane

The flattening procedure applied to the event plane is to ensure the distribution to be flat, and removes any detector effect. One way to check wether there are any residual detector effects that may lead to artifical correlation between tracks and the EP is to calcualte the sin component of the distribution of tracks with respect to the EP:

$$s_n^{obs} = \langle \sin n(\phi - \Psi_n) \rangle \tag{21}$$

This term should vanish since the reaction plane seen by the tracks is the same plane as measured by the Full-Fcal or Sub-Fcal. We quanty this residual sin term by taking the ratio of s_n^{obs} to the observed cos term charactorized by the v_n^{obs}.

The results for this check are shown in Figure 28 and 31 for several centrality selections for Full-Fcal (Since the same two-sub-event method are used. This residual sin term is almost identical for Sub-Fcal). One does see small but significant sin signal for particle relative to the measured EP. The s_n^{obs} signal relative to v_n^{obs} seems to be independent p_T, suggesting that this is a residual effects of the EP determination that affects all particles indepndent of their momentum. However, we do not see any obvious centrality dependence for such shifts, suggesting if may arise from the residual correlation between the Inner Detector and Fcal (for example deadarea appearing at the same ϕ location). A conservative estimate of the shift is about 0.5% , 1% , 2% and 4% for $n = 2$, 3, 4, and 5 respectively and they are always show a negative value. However for $n = 6$ shift is significantly larger and it is positive with an average deviation of about 10%.

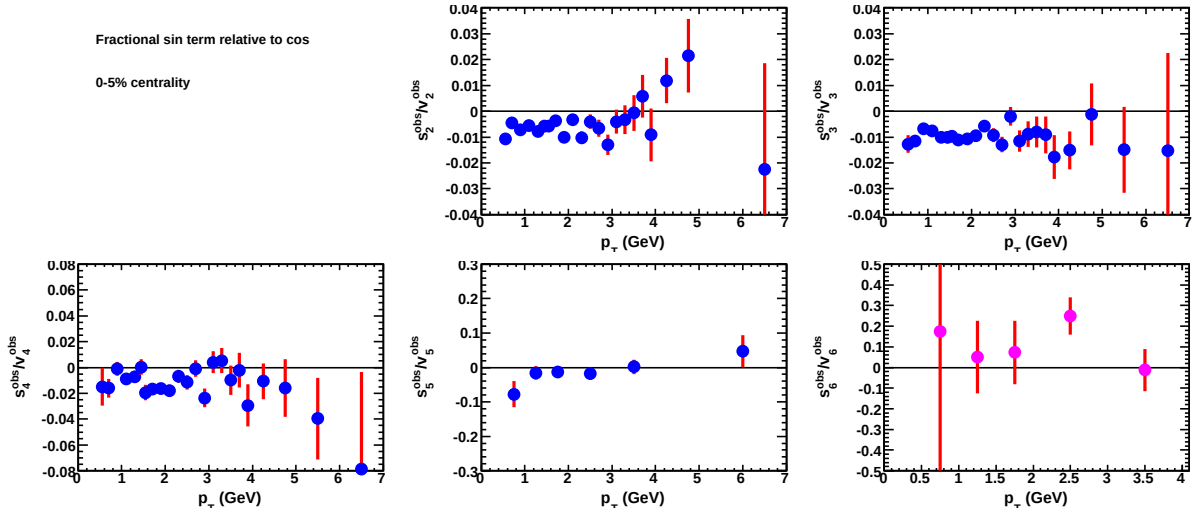

Figure 28: The ratio of raw observed sin term (s_n^{obs}) to the cos term (v_n^{obs}) as function of p_T for 0-5% centrality

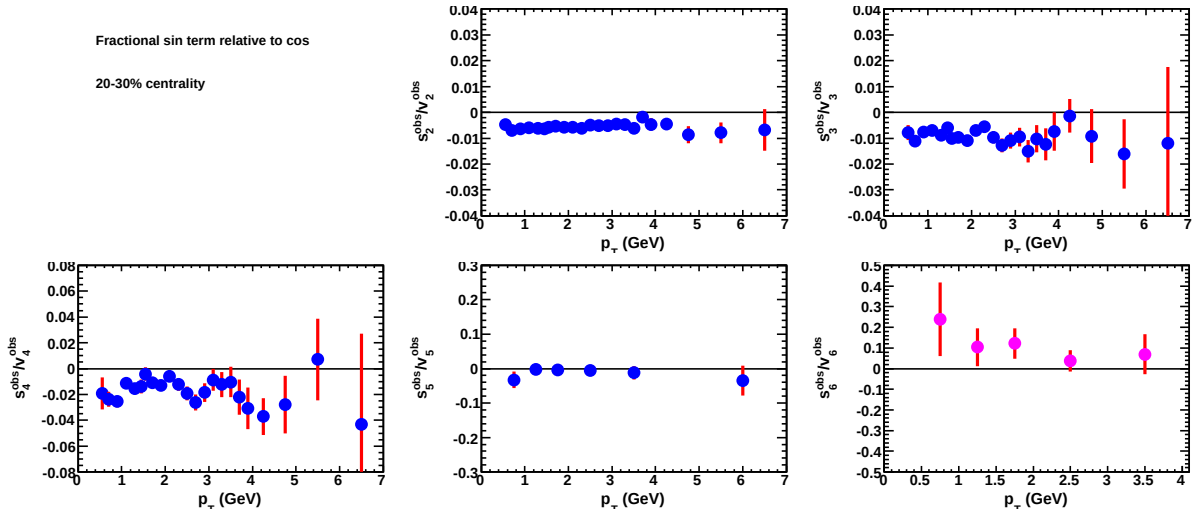

Figure 29: The ratio of raw observed sin term (s_n^{obs}) to the cos term (v_n^{obs}) as function of p_T for 20-30% centrality

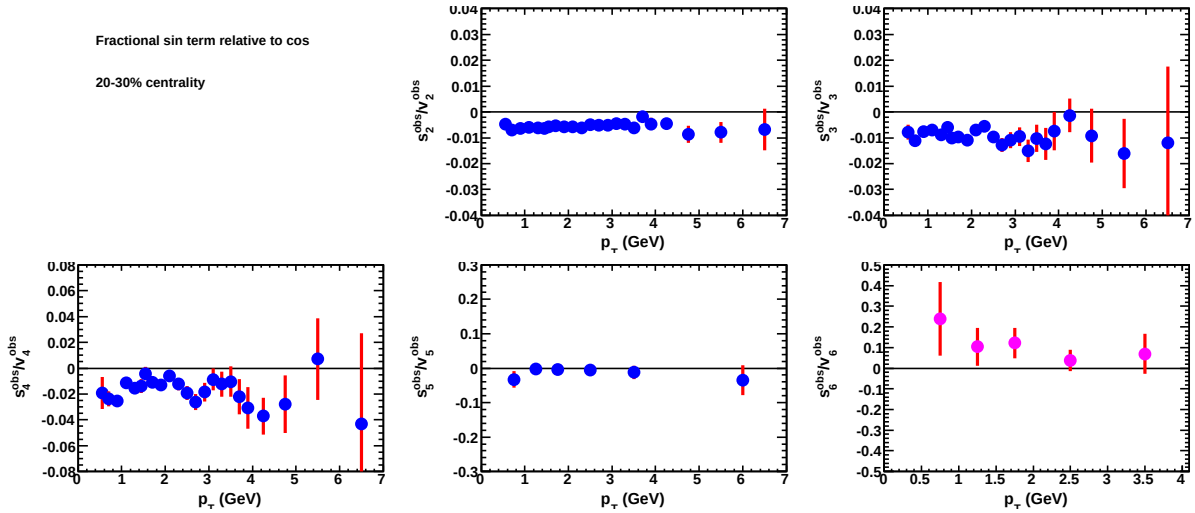

Figure 30: The ratio of raw observed sin term (s_n^{obs}) to the cos term (v_n^{obs}) as function of p_T for 30-40% centrality

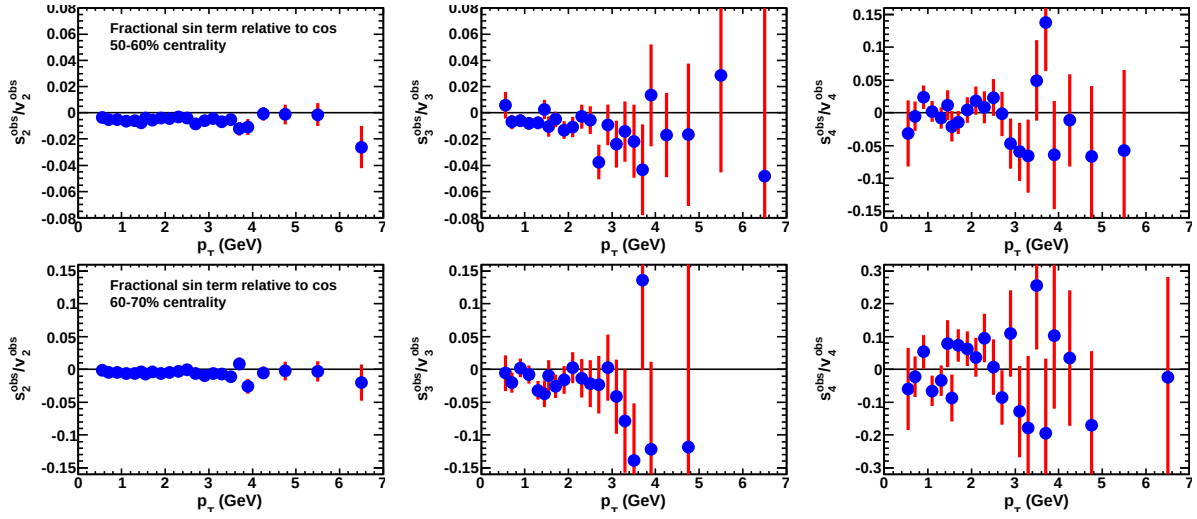

Figure 31: The ratio of raw observed sin term (s_n^{obs}) to the cos term (v_n^{obs}) for $n = 2-4$ as function of p_T for 50-60% (top) and 60-70% (bottom) centrality

5 Systematic errors discussion

5.1 Resolution correction and v_n^{obs}

Since v_n is calcualted as the ratio of v_n^{obs} to the resolution factor Res$\{\Psi_n\}$, so the all the systematic uncertainty arise from these two factors. The systematic error on the resolution correction has been evaluated with the three sub-event method, while those for the v_n^{obs} are evaluated by the sin term for distribution of tracks relative to the EP. Both of these two sources of error has been discussed and final uncertainty has been obtained. However in addition to these studies, we should also check the stablity of the results against the track and event selection we used in this analysis. That include the track cuts, centrality selection, and run by run variation of the v_n. We only use the Full-Fcal results for this check, since the results are essentially the same for Sub-Fcal. We shall focus on these sources of uncertainty in this section.

5.2 Effect of Tracking Cuts on v_n

As we did with the correlation analysis, we check to see if the cuts for $z0 \times sin(\theta)$ and $d0$ affect the measured flow harmonics or not. As before, we choose three different classes of cuts:

1. The standart "Tight cuts" : $d0 < 1mm$ and $z0 < 1mm$
2. 3.5σ cuts : $d0 < 3.5\sigma_{d0}$ and $z0\sin(\theta) < 3.5\sigma_{Z0}$
3. 1.0σ cuts : $d0 < \sigma_{d0}$ and $z0\sin(\theta) < \sigma_{Z0}$

where $\sigma_{d0/z0}$ are given by:

$$\begin{aligned} \sigma_{d0} &= \sqrt{(0.0211)^2 + \left(\frac{0.182}{(p_T/GeV)}\right)^2}\, mm \\ \sigma_{z0} &= \sqrt{(0.0542)^2 + \left(\frac{0.252}{(p_T/GeV)}\right)^2}\, mm \end{aligned} \tag{22}$$

The d_0^{cut} and z_0^{cut} are momentum dependent 1 standard deviation value of the d_0 and z_0 distributions. They are obtained by fitting the d_0 and z_0 distributions in p_T slices with double Gauss. The fit results for a representative central and peripheral bins are shown in Figure 32.

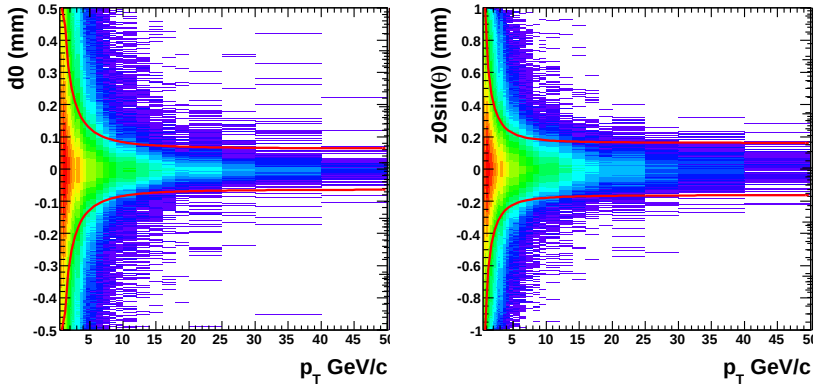

Figure 32: $d0$ and $z0sin(\theta)$ distributions for tracks as a function of p_T. The red curves indicate the p_T dependent cuts (used on top of the $1mm$ cuts).

Figure 33-36 summarize the varation of the v_n as function p_T for several centrality selections. The variation is quantified in terms of the ratios between the v_n with the matching cuts and without matching cut. We see in general the variation is small for all p_T centrality selections for $n = 2, 3$ and 4, but are somewhat larger for $n = 5$ and 6. We also notice a small but significant p_T dependence especially at

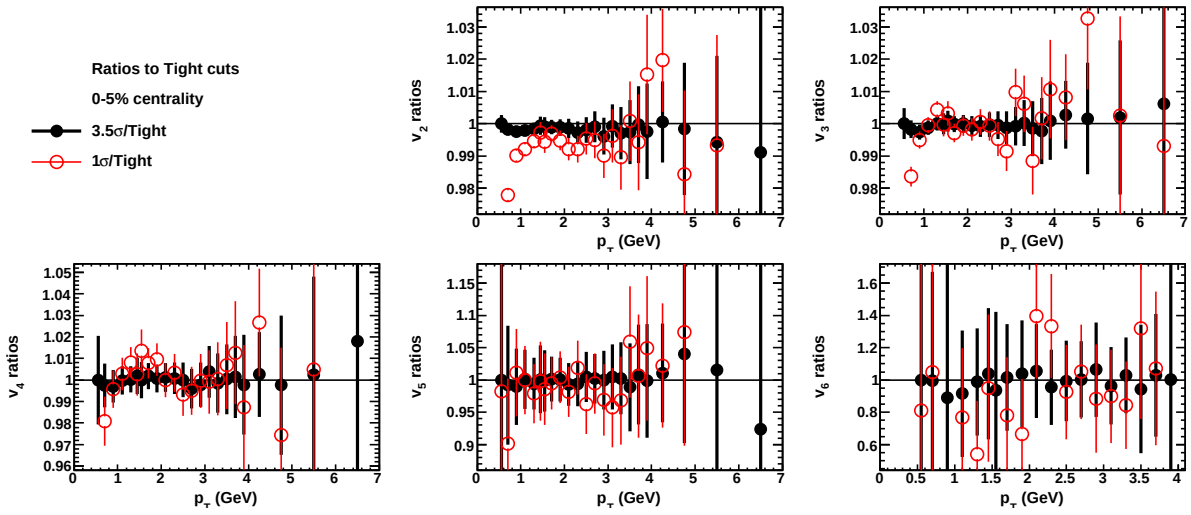

Figure 33: Ratios of the Full-Fcal v_n for tracks with matching cuts to those without matching cut to d_0 and $z_0 \sin\theta$. This is for 0-5% most central events.

$p_T < 2$ GeV in most central collisions. Such variation can be up to 2% at $p_T \sim 0.5$ GeV, suggesting that the v_ns are slightly smaller when a tight cut is used. This can be understood from the changing of the particle mixture when a tight matching is used. Namely, the protons and kaons tend to have large multiple scattering than that for charged pions, so they tends to have broader matching distribution and wold be preferablely removed when a tigher cut is used. In addition, the feed-down contribution also tends to have larger matching distribution as well. If these particle species have a larger v_n, then a tighter

matching cut tends to throw them away, leading to a smaller v_n. However this p_T dependence seems is only significant for 0-5% most central collisions.

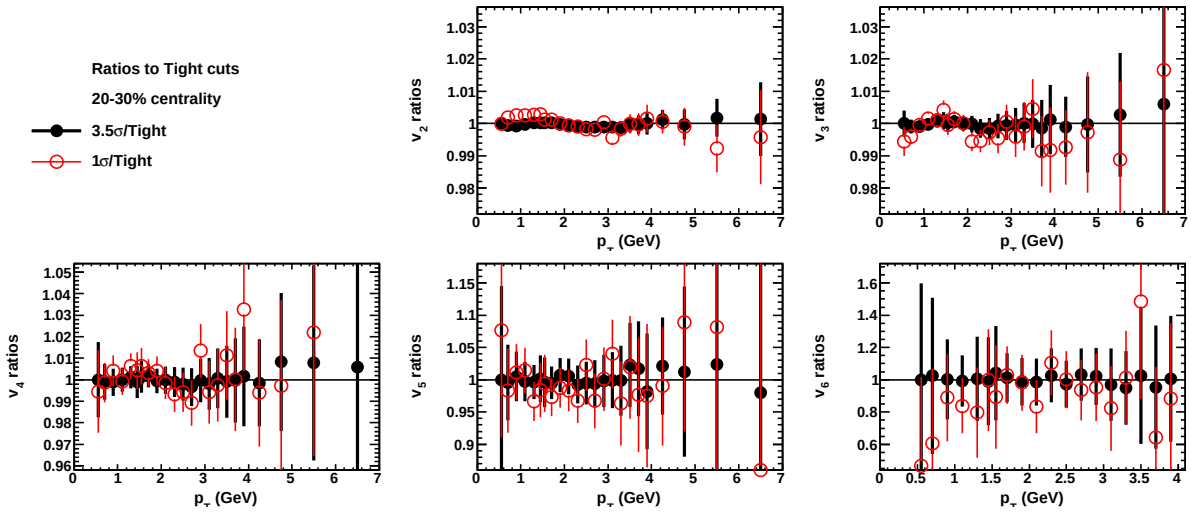

Figure 34: Ratios of the Full-Fcal v_n for tracks with matching cuts to those without matching cut to d_0 and $z_0 \sin\theta$. This is for 20-30% most central events.

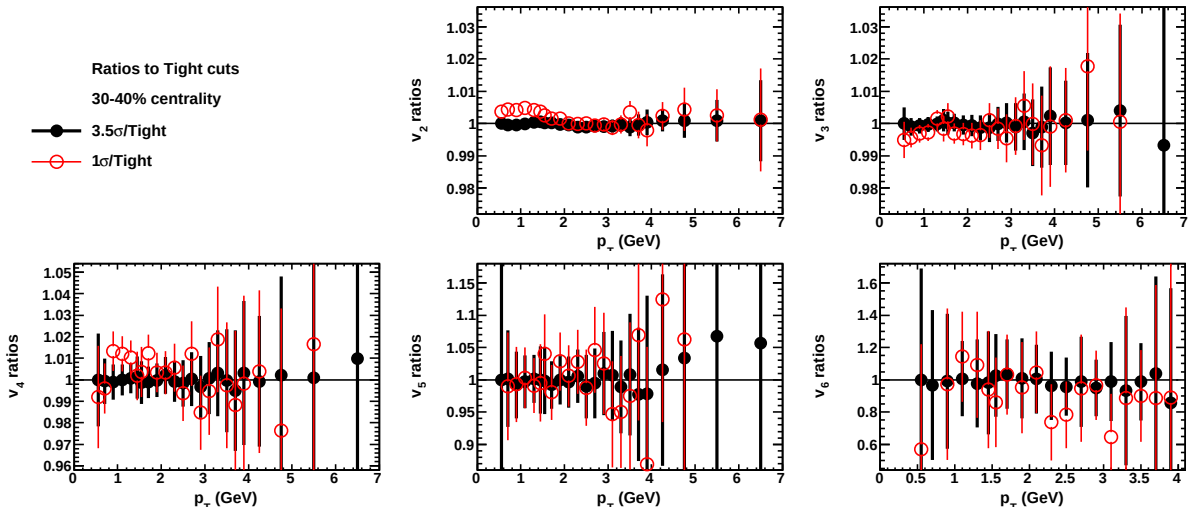

Figure 35: Ratios of the Full-Fcal v_n for tracks with matching cuts to those without matching cut to d_0 and $z_0 \sin\theta$. This is for 30-40% most central events.

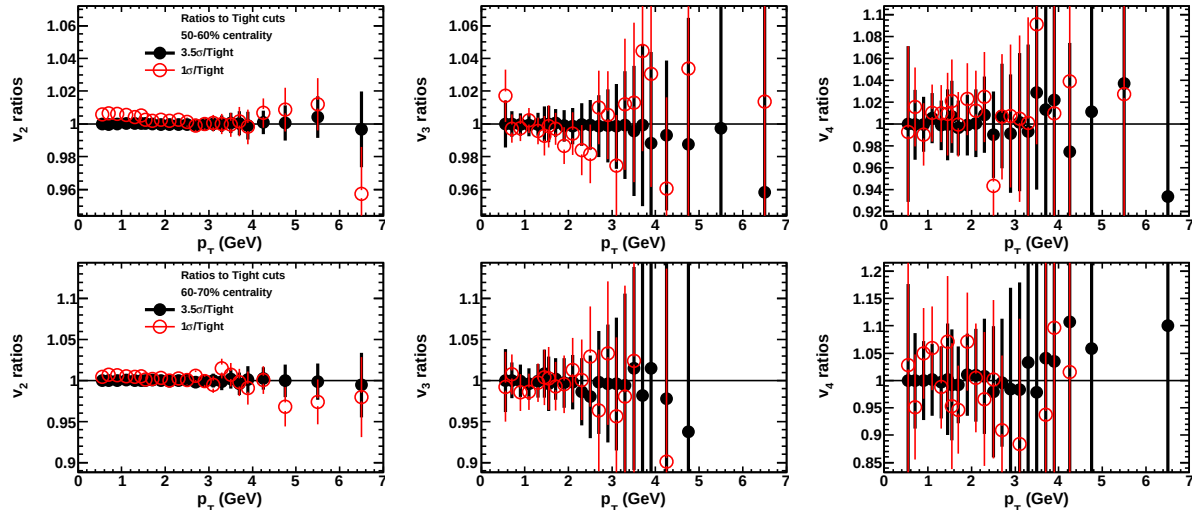

Figure 36: Ratios of the Full-Fcal $v_2 - v_4$ for tracks with matching cuts to those without matching cut to d_0 and $z_0 \sin\theta$ for 50-60% (top) and 60-70% (bottom) centrality selections.

In other centrality bins the variations are always less than 0.5% for v_2 and v_3, it becomes about 2% for v_4, 3% for v_5 and up to 10% for v_6. In Table 7 list the final systeamtic error we quote on the results.

The systematic error due to track cuts				
	Centrality	$p_T < 1$ GeV	$1 < p_T < 2$ GeV	$2 < p_T$ GeV
v_2	0-10%	2%	0.5%	0.2%
	¿10%	0.5%	0.5%	0.2%
v_3	0-10%	2%	0.5%	0.2%
	¿10%	0.5%	0.5%	1%
v_4	0-40%	2%	1%	1%
	¿40%	2%	2%	2%
v_5	0-50%	3%	3%	3%
v_5	0-50%	10%	10%	10%

Table 7: Summary of systematic errors for the v_n associated with track cuts

5.3 Run by run variations of v_n

The ATLAS detector performance could also vary from run to run. Such variation in principle should largely be smoothed out when we present the results for the full datasets. Nevertheless, it is important to see whether the detector is stable over the time of the whole heavy ion running, and how much change it translate into the v_n in the correlation analysis. Since such check severely lowers event statistics, we organize all the runs into 4 different running periods or groups with approximately the same statistics. The run ranges and corresponding luminosity are listed in Table 8. The way we used to check the variation is by taking the ratio of the v_n obtained in each run group with those for the full statistics.

Run range	169405-169270	169564-169839	169864-170002	170004-170482
luminosity(μb^{-1})	1866.3	1832.9	1772.7	1873.3

Table 8: The four run groups and corresponding integrated luminosity.

Figure 37-40 shows the dependence of the v_n variation on p_T for several centrality selections. Overall we do not see a clear dependence on the target p_T nor centrality, although the ratios shows larger spread due to increasing statistical error. The level of p_T and centrality dependent deviations beyond statistical fluctuation is about < 0.5%, 1%, 2%, 3% and 10% for $v_2 - v_6$, respectively.

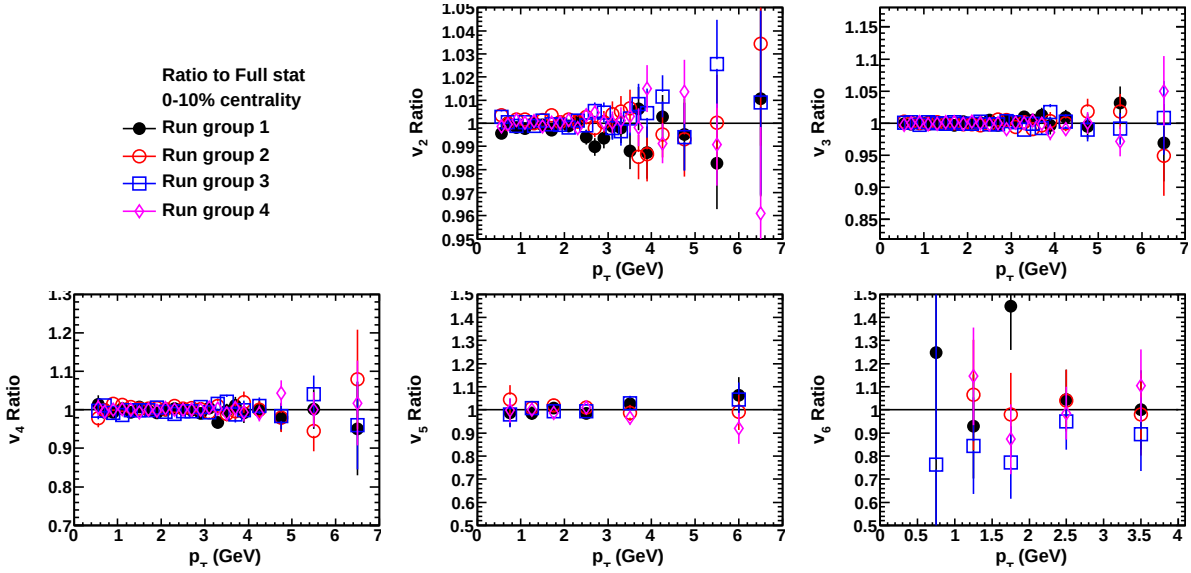

Figure 37: p_T dependence of the run by run variation of the full-fcal v_n obtained for four run groups. From top to bottom they are for 0-10% centrality selections.

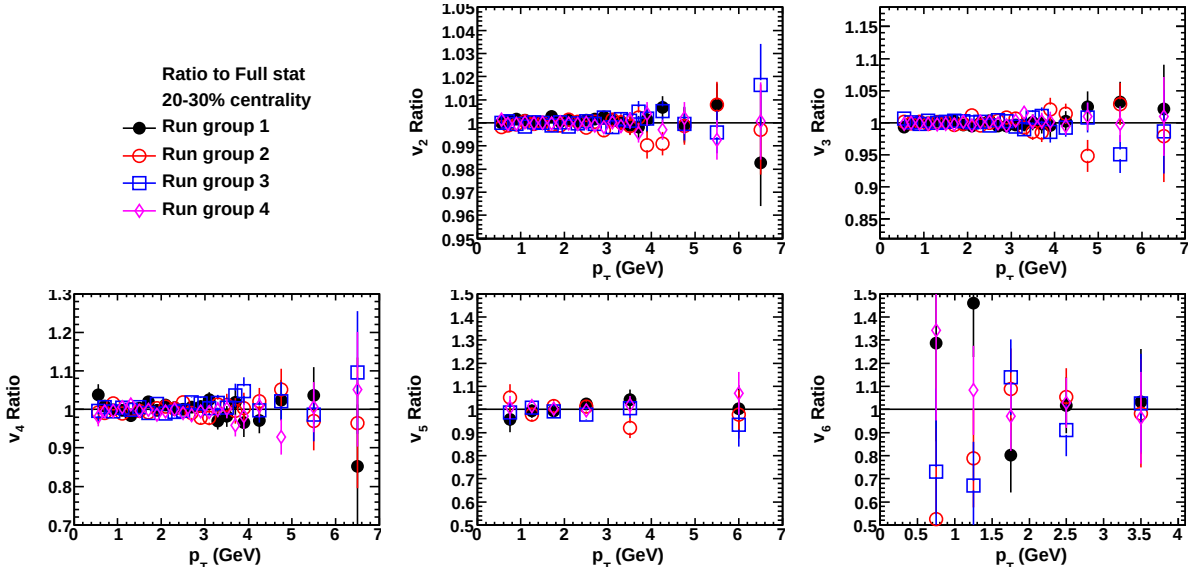

Figure 38: p_T dependence of the run by run variation of the full-fcal v_n obtained for four run groups. From top to bottom they are for 20-30% centrality selections.

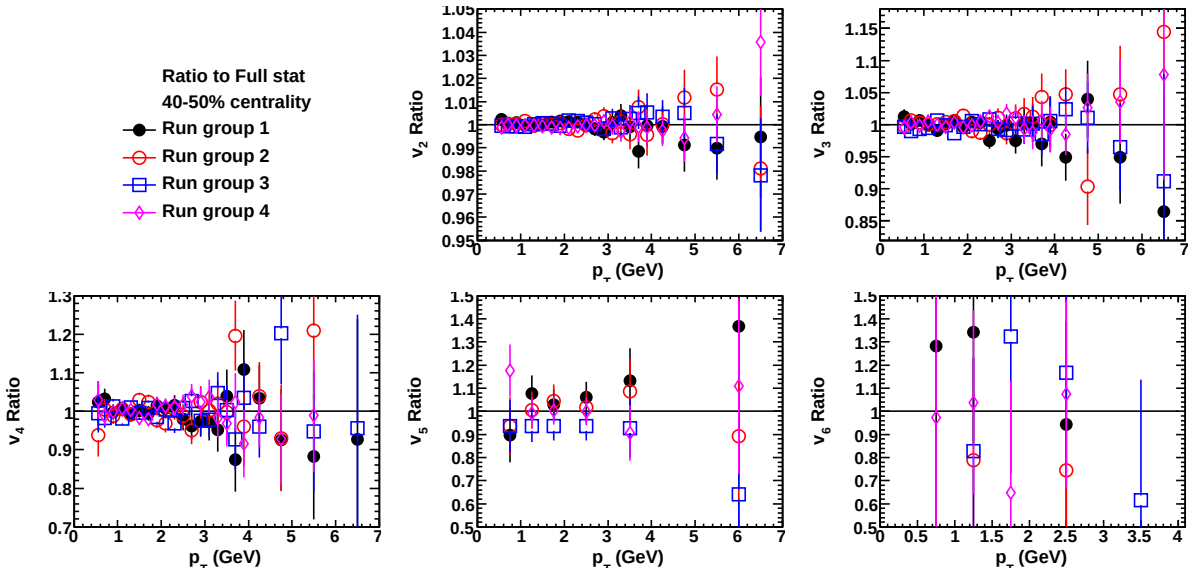

Figure 39: p_T dependence of the run by run variation of the full-fcal v_n obtained for four run groups. From top to bottom they are for 40-50% centrality selections.

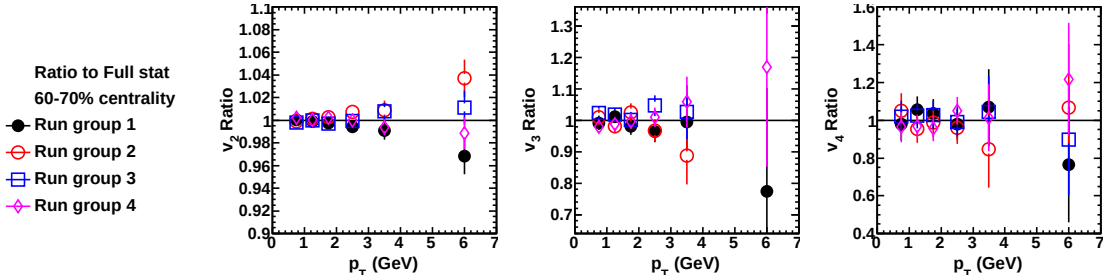

Figure 40: p_T dependence of the run by run variation of the full-fcal v_n obtained for four run groups. From top to bottom they are for 60-70% centrality selections.

5.4 Monte Carlo studies

A detailed Monte-Carlo study of the flow analysis method had been done by the flow group for v_2 measurements using HIJING with an afterburner that implement the v_2 signal before the GEANT simulation. In general a good agreement has been observed between the reconstructed v_2 value and those at the truth level. This is shown by Figure 41 directly copied from their note.

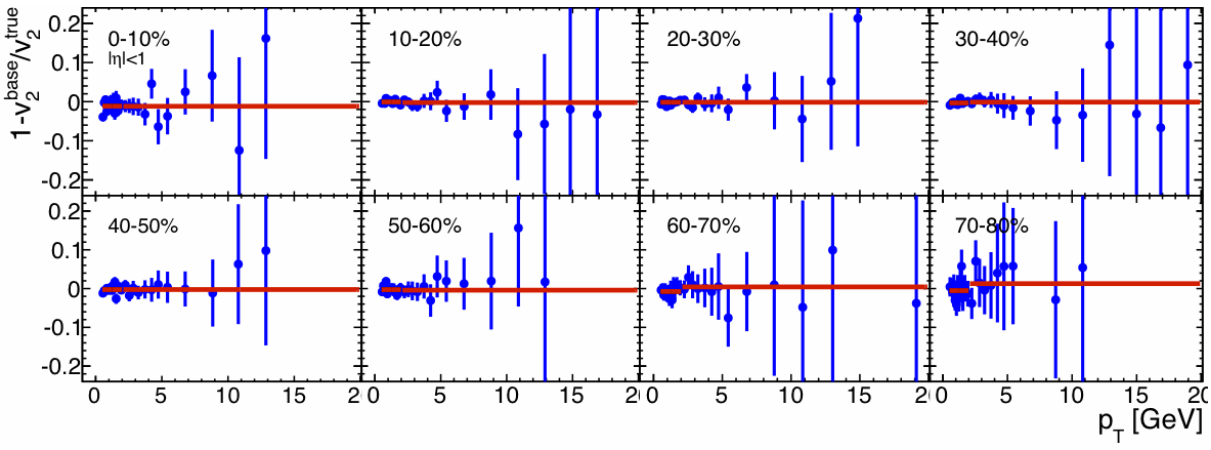

Figure 41: Relative differences between the reconstructed and true v_2 for $|\eta| < 1$.

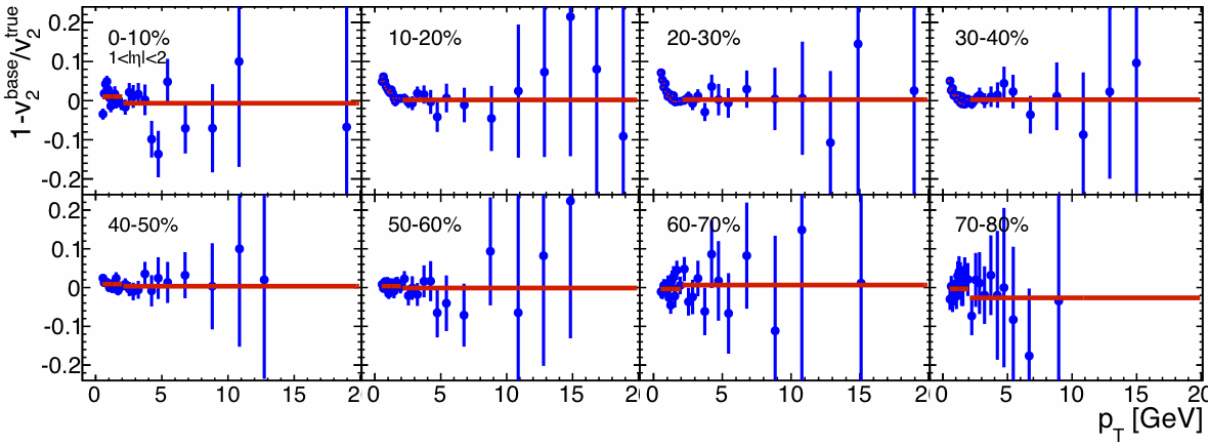

Figure 42: Relative differences between the reconstructed and true v_2 for $1 < |\eta| < 2$.

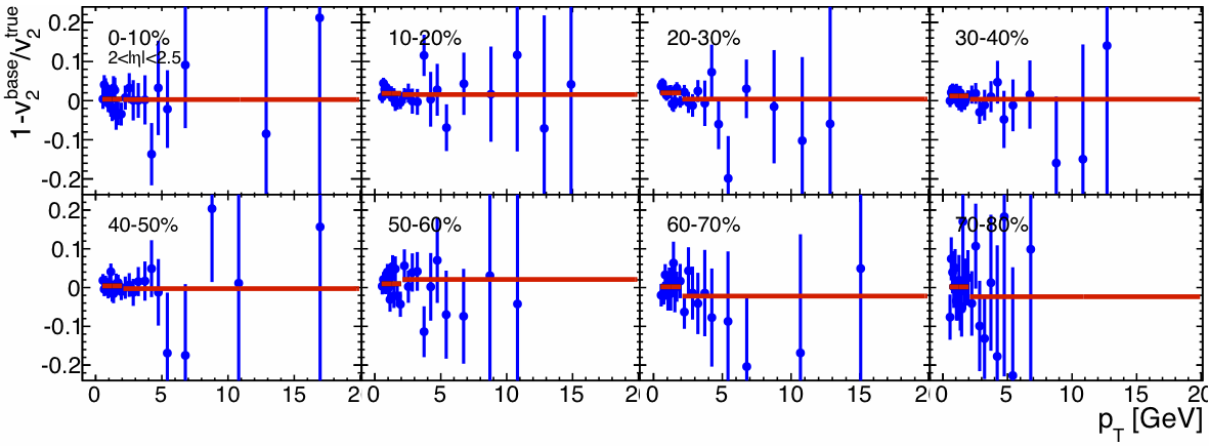

Figure 43: Relative differences between the reconstructed and true v_2 for $2 < |\eta| < 2.5$.

Since this is the first time the higher order harmonic is measured. No such physics signal has been introduced in the ATLAS Monte Carlo simulation. So we did not check the reproducibility of the v_n in

MC. However we expect the performance should be quite similar. At current stage we do not quote any systematic error associated with the v_n from MC.

5.5 Data driven cross-checks with Fcal sub-detectors

One advantage of flow analysis in ATLAS is the fine segmentation of the detector allow measurement of v_n using event plane determined by many different detectors. We have seen the demontration of this in the section where determine the Fcal resolution by correlating it with the EP determined by other detectors. In this section, we are going to divide Fcal into several sub-detectors and measure the v_n indpendently. In this study we use the following set of sub-detectors

- FCal layer one (FCal1)
- FCal layer two (FCal2)
- FCal layer three (FCal3)
- FCal layer one at $3.3 < |\eta| < 4.0$ (FCal1-low)
- FCal layer one at $4.0 < |\eta| < 4.8$ (FCal1-high)
- FCal layer one and two (FCal12)

Where the last one is our default analysis which have discussed in great length so far. The analysis procedure for the first five cases are exactly the same as those for the default. Including the calibration and fattening of the event plane, and resolution correction. We then compare the v_n results with those obtained by the full Fcal layer1 and layer2 (our default results).

The first three checks are useful in the sense that they are situated at exactly the same rapidity, thus they are suppose to measure the same underlying reaction plane. So by comparing these three cases, we can check how well we can reproduce the v_n. Note that tee composition of particles that contribute to the E_T in the three layers of the FCal are expected to be somewhat different (π^0 contribute mostly to first layer, while charged hadron can contribute to all layers. The last two checks are useful because they have different rapidity gap from the inner detectors, thus a comparison between the two allows use to quantify the effects of auto-correlations, especally those from jets.

Figure 44 compare the resolutions obtained by the three different layers of the Fcal for $\Psi_2 - \Psi_5$ together with Fcal12. We see that Fcal1 has the best much better resolution compare to Fcal2 which in turn is much better than FCal3. For Ψ_4 and Ψ_5 the Fcal3 resolution is very poor hence was not used in the analysis. We see than the resolution for Fcal12 which is obatined bu combining Fcal1 and Fcal2 is only slightly better than Fcal1. In Figure 45, we make similar comparisons between FCal1-low and FCal1-high to FCal1 (which is the combination of FCal1-low and FCal1-high). We see that for $n = 2$ the resolutions between FCal1-low and FCal1-high are comparable, but for higher order harmonics the resolution of FCal1-high drops much lower than FCal1-high.

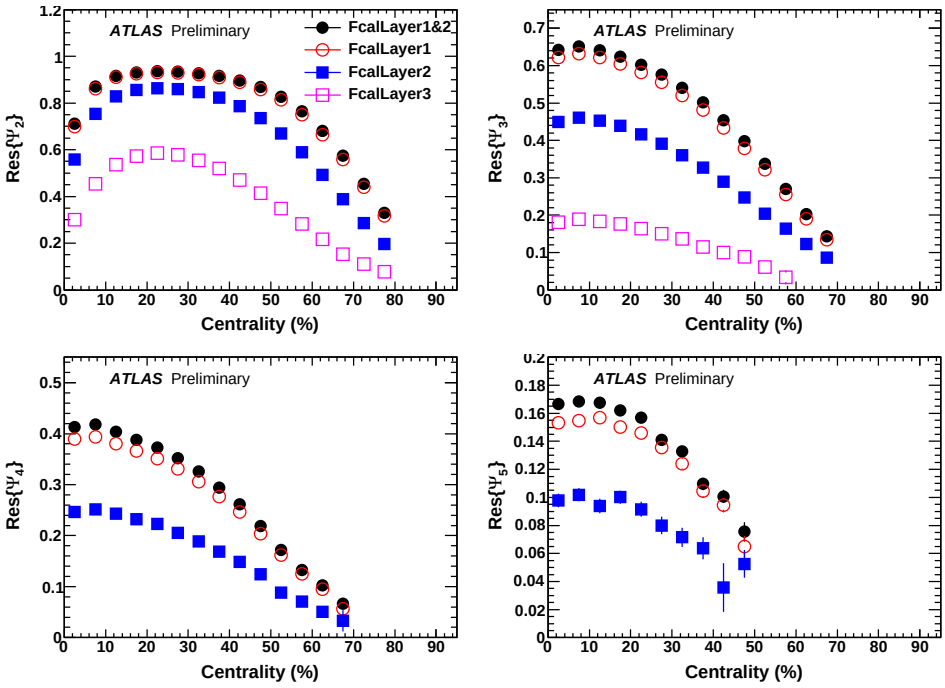

Figure 44: The centrality dependence of the n^{th} reaction plane resolution factor for n=2 to 5, compared between FCal1, FCal2, FCal3.

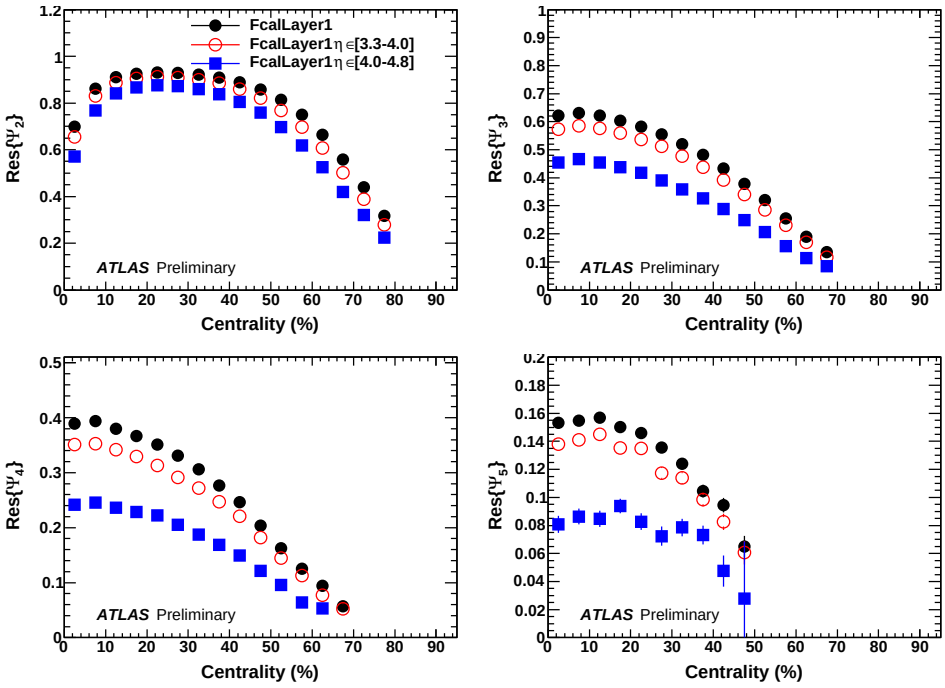

Figure 45: The centrality dependence of the n^{th} reaction plane resolution factor for n=2 to 5, compared between FCal1_low, Fcal1_high and FCal1

Figures 46-49 show the ratios of the v_n using the EPs measured by different parts of the FCal detectors. The top panels show the comparison of v_n from FCal1, FCal2 and FCal3 relative to Fcal12. The lower panels show comparison of FCal1-low and FCal1-high to FCal1. For v_2 values compared in Figure 46, we see that FCal1 and FCal2 adree within 1%, while the results from FCal3 are a few percent higher. This is not unexpected, as the FCal3 resolution is very poor and we expect it has its own addtional systematics. For v_3 values (figure 47 we also have good agreement within 2% – 5%, here we dont show the values for FCal3 in the 60 – 70% bin as the resolution is very poor. Figures 48 and 49 show comparisons for v_4 and v_5, we exclude FCal3 from here because it has very poor resolution. For v_4 and v_5 also we see good agreement wherever the statistics alow us make such comparisons.

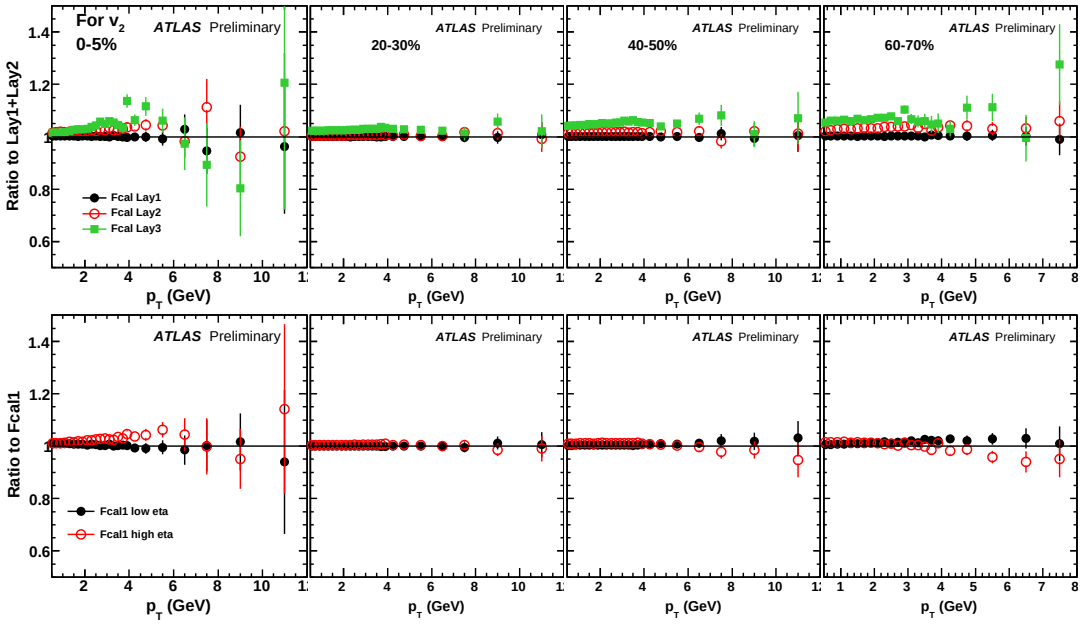

Figure 46: Top panels: Ratios of v_2 obtained using different layers of Fcal (top row) to that obtained using Full-Fcal. Bottem panels: Ratios of v_2 obtained using different η segments of Fcal-layer1 (Fcal1-low and FCal1-high) to full Fcal-layer1(FCal1). Both comparisons are shown for four representative centrality selections.

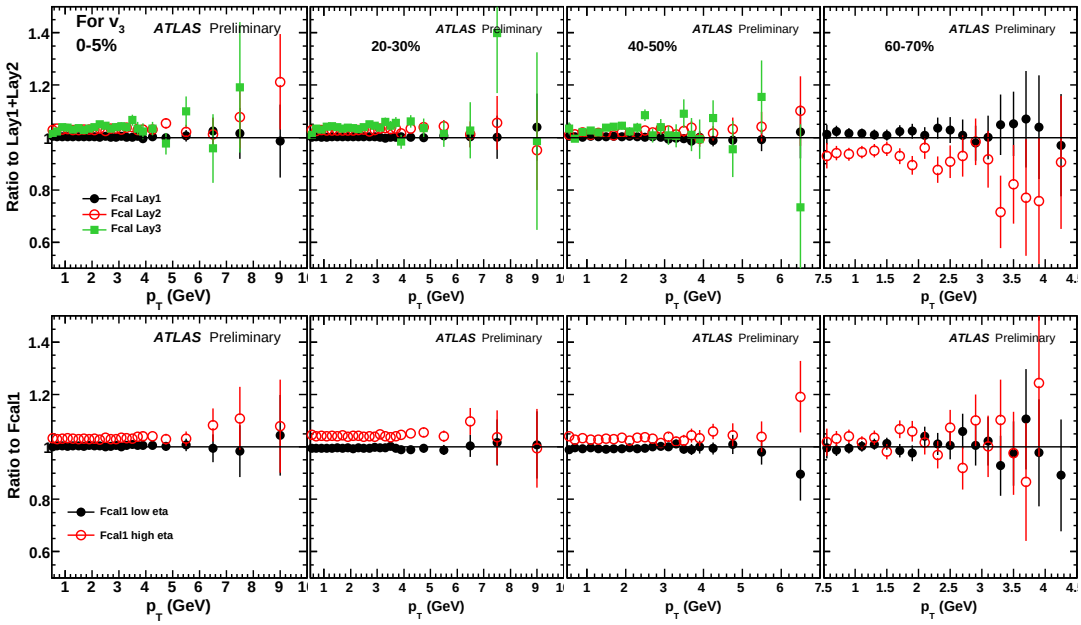

Figure 47: Same as previous figure, but for v_3

;

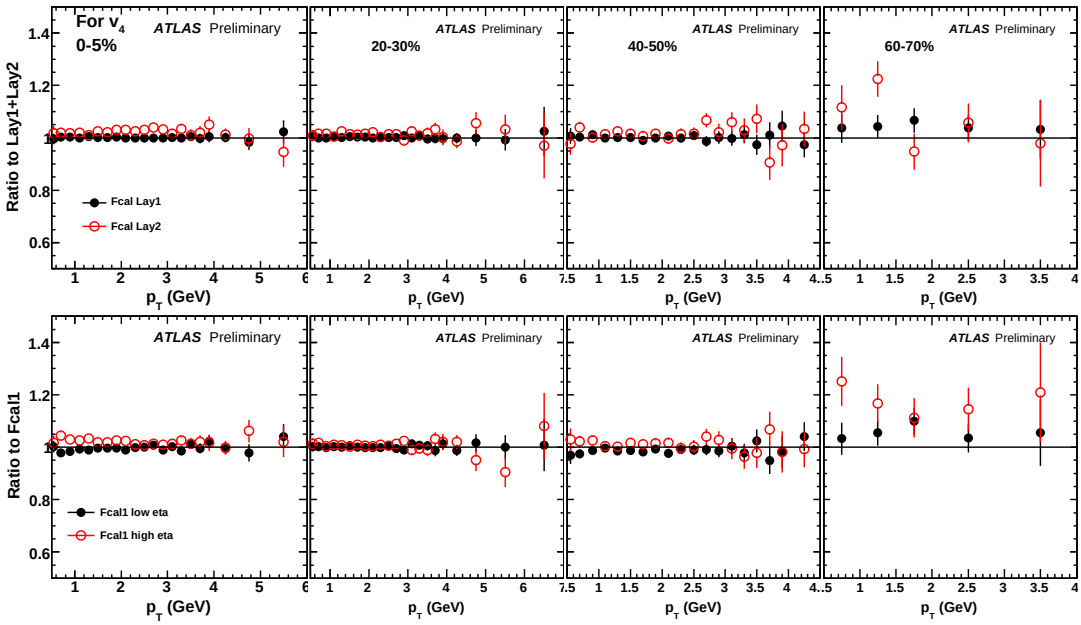

Figure 48: Same as previous figure, but for v_4

;

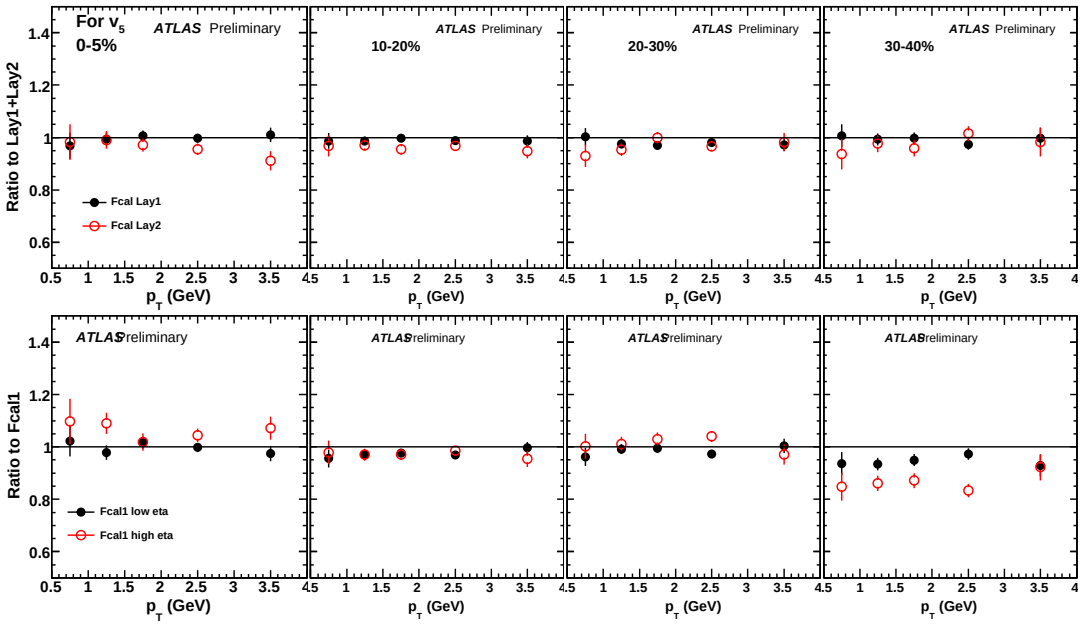

Figure 49: Same as previous figure, but for v_5

;

In general, the summary of these checks are that they have shown that the systematic effects due to reaction plane determination and autocorrelation are quite small (¡5%), but are slightly different for different order of harmonic flow. However, as n increase, the precision of v_n measurement decreases, and the systematic errors increases, especially in the case of v_6. One caveat with this comparision is that different detectors has their own set of associated systemtics. The systematic errors for detectors with poor resolution should be larger. For example FCal2has a smaller weight to combined EP plane for FCal12, but in general has poor performance compare to the first layer (more noise and worse energy resolution, the shower profile is also larger). However, the fact that these detectors can have up to factor 4 difference in their resolution correction, while still agree with each other within 2-10% is amazing. This also give us confidence to our results.

Table 9 summarize the systematic difference seen between different measuremnents for $v_2 - v_5$.Most likely this difference comes from the detectors with poor resolution, thus not representative of the true resolution of the combined detector Fcal12. So we shall treat the study in this section as cross checks and do not include them in the final systematic error table.

Table 9: Summary of the cross-checks for v_n measurements using different EP detectors

	Layer1 vs Layer2			Low vs high η		
	central	mid-central	peripheral	central	mid-central	peripheral
v_2	2%	1%	3%	1-5%	1%	$< 5\%$ at $p_T < 4$ GeV
v_3	2%	2%	3 %	2%	3%	3%
v_4	1%	1%	1%	3%	1%	1%
v_5	3%	2%	3%	3%	3%	3%

5.6 Summary of the systematic uncertainties

Table 10-14 summarize the list of systematic errors on $v_2 - v_6$ measurement for Full-Fcal and Sub-Fcal methods for various centrality ranges. They are quoted nominally for 5% centrality bins. For example 0-20% refer to 0-5, 5-10, 10-15, and 15-20% bins, the corresponding errors refer the range of errors for that four bins. For example an 5-2% error would mean that the error for 0-5% centrality bin is 5% and that for 15-20% centrality bin is 2%. We also quote the error for a special 0-1% centrality bin, which usually has the same systematic errors as that for 0-5%. However it has its own statistical uncertainty for the resolution correction, which can become very big for v_6.

Error type	comment	Centrality				
		0-20%	20-40%	40-50%	50-70%	70-80%
Resolution	Sys.	5-2%	1.5-1%	1.5-2%	3-4%	4-6%
	stat.	0.06-0.1%	0.01%	0.02%	0.04-0.1%	0.2-0.4%
track cut	$p_T < 1$ GeV	2%	0.5%	0.5%	0.5%	1%
	$1 < p_T < 2$ GeV	0.5%	0.5%	0.5%	0.5%	1%
	$2 < p_T$ GeV	0.1%	0.1%	0.1%	0.5%	1%
residual sin term		0.8%	0.6%	0.6%	0.5%	0.2%
run-by-run variation		0.2%	0.1%	0.2%	0.5%	1%
Total	$p_T < 1$ GeV	5.5-3%	1.3-1.7%	1.3-2.2%	3.2-4.1%	4.3-6.2%
	$1 < p_T$ GeV	1%	1.3-1.7%	1.3-2.2%	3.2-4.1%	4.3-6.2%

Table 10: Summary of systematic errors for the v_2 for both full-FCal and sub-FCal

Error type	comment	Centrality			
		0-20%	20-40%	40-50%	50-70%
Resolution	Sys.	3%	3%	3%	3-5%
	stat.	0.09%	0.1-0.17%	0.3%	0.4-2.6%
track cut	$p_T < 1$ GeV	2%	0.5%	0.5%	0.5%
	$1 < p_T$ GeV	0.5%	0.5%	0.5%	2%
residual sin term		1%	1%	1%	1.5%
run-by-run variation		0.5%	0.5%	1.5%	2%
Total	$p_T < 1$ GeV	3.8%	3.4%	3.7%	4-6.2%
	$1 < p_T$ GeV	3.3%	3.4%	3.7%	4.4-6.5%

Table 11: Summary of systematic errors for the v_3 for both full-FCal and sub-FCal

Error type	comment	Centrality					
		0-1%	0-20%	20-40%	40-50%	50-60%	60-70%
Resolution	Sys.	4%				4	5%
	stat.	0.7%	0.3%	0.3-0.5%	0.7-1.1%	1.8-3.2	5.9-15%
track cut		1%	1%	1%	2%	4%	4%
residual sin term		2%	2%	2%	2%	3%	5%
run-by-run variation		1%	1%	1.5%	2%	4%	4%
Total		4.8%	4.7%	4.9%	5.4%	7.8-8.2%	11-17.5

Table 12: Summary of systematic errors for the v_4 for both full-FCal and sub-FCal

Error type	comment	Centrality			
		0-1%	0-20%	20-40%	40-50%
Resolution	Sys.	10%			
	stat.	4%	2%	2-4%	5-20%
track cut		1%	1%	1%	2%
residual sin term	$p_T < 1$ GeV	5%			
	$p_T > 1$ GeV	2%	2%	5%	2%
run-by-run variation		2%	2%	2%	4%
Total		12.3%	11.8%	13%	13-23%

Table 13: Summary of systematic errors for the v_5 for both full-FCal and sub-FCal

Error type	comment	Centrality bins			
		0-1%	0-20%	20-40%	40-50%
Resolution	Sys.	30%			
	stat.	50%	16-7%	6-9%	12-23%
track cut		10%			
residual sin term		10%			
run-by-run variation		10%			
Total		61%	38-35	36%	37-42%

Table 14: Summary of systematic errors for the v_6 for both full-FCal and sub-FCal

6 Results

Let us quickly summarize the process used to obtain the v_n values. The whole process has been discussed previously, here we doa quick recap. The analysis involved two passes through the data and one final analysis:

- First Pass : This pass is used for obtaining the correation factors for the Q-vectors for each order which includes $\langle Q^{raw} \rangle$ and the flattening corrections. The calibration constants obtained in this pass are used in the second pass.

- Second Pass : In this pass, for each event the raw Q-vectors for each harmonic are measured after the shifting and flattening corrections are applied. The Q-vectors are then used to determine the

event plane orientation. Finally the distribution of the charged particles w.r.t. the event plane (Ψ_n) are stored in bins of p_T , η (of track) and centrality(of event). Also the correlations between the event planes obtained by the the positive and negative sides of the FCal (i.e. $\Psi_n^P - \Psi_n^N$) are stored for all centrality bins. This correlation will be used to obtain the reaction plane resolution.

- Final Analysis : The correlation between $\Psi_n^P - \Psi_n^N$ is used to obtain the reaction plane resolution for each harmonic. Also by taking the fourier transformation of the particle distributions about the event plane, the raw v_n values are obtained. The raw v_n values are corrected to account for the reaction plane resolution to obtain the final corrected v_n values.

- Systematic Errors : For estimating the various systematic errors discussed in the text, usually specialized analysis similar to the one above are run with the necessary parameter (such as tracking cut or reaction plane detector) appropriately modified. For the final result, the systematic errors from the various sources are put together (as discussed in the systematic-errors-section).

6.1 η dependence

The η dependence of v_n is more sensitive to jet influence, especially at high η where the track is close to the FCal. Hence a resonable η gap is necessary between the tracks and the detector used to determine the reaction plane. The Full-Fcal has a minimum 0.8 unit seperation from the tracks while the Sub-Fcal has a minimum of 3.3 unit seperation from the track. Figure 50-54 summarize the η dependence of the v_n for selected centrality and p_T. In each panel the results from Full-Fcal(top two rows) and Sub-Fcal (bottom two rows) are always shown together to illustract the effects of the auto-corrleations. We see the results for Sub-Fcal has a slight decrease of the v_n towards large η by about 5%; Since the EP is in opposite hemisphere relative to tracks, larger η implies a even larger rapidity seperation (so it reaches 5.8 unit seperation at $\eta = 2.5$). The Full-Fcal also show a small decrease in some cases, but in general much flatter than the sub-fcal results. These few % difference between the two methods could indicate the level of auto-correlations.

Based on this observation, we decide to use the Sub-Fcal to present the η dependence, while use the Full-Fcal for the p_T and centrality dependence study. The reason for this is that The full FCal has a better resolution that the Sub-FCal. This is especially important for v_5 and v_6 measurements where the resolution is very low (in which case the full FCal has $\sim \sqrt{2}$ times higher resolution. The difference between Full-Fcal and sub-fcal for η integrated v_n results differs by about 2.5% on average.

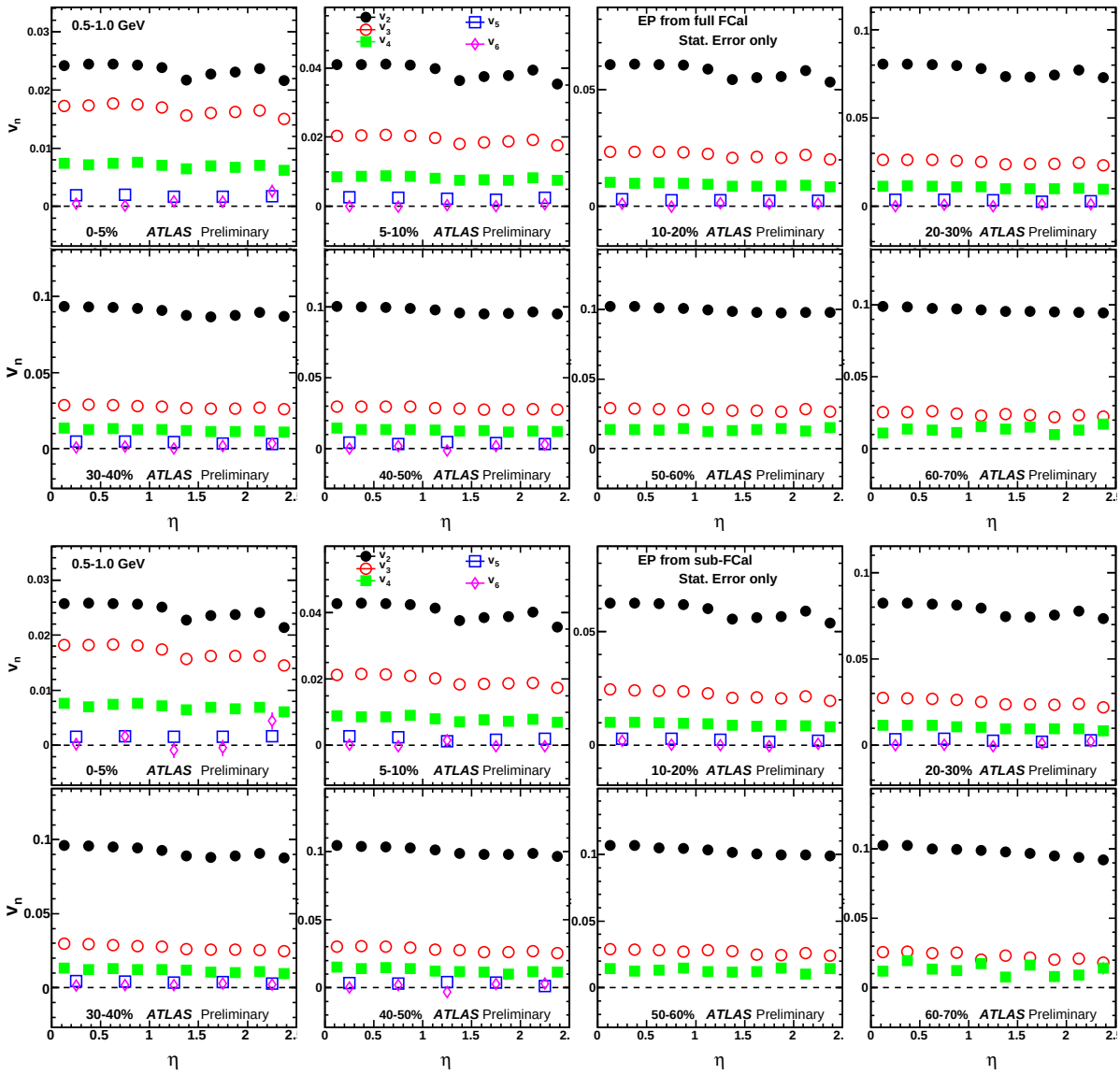

Figure 50: η dependence of v_n for 0.5-1 GeV bin, Each panel corresponds to a different centrality class. Top two rows corresponds results using Full-Fcal while the bottom corresponds Sub-Fcal.

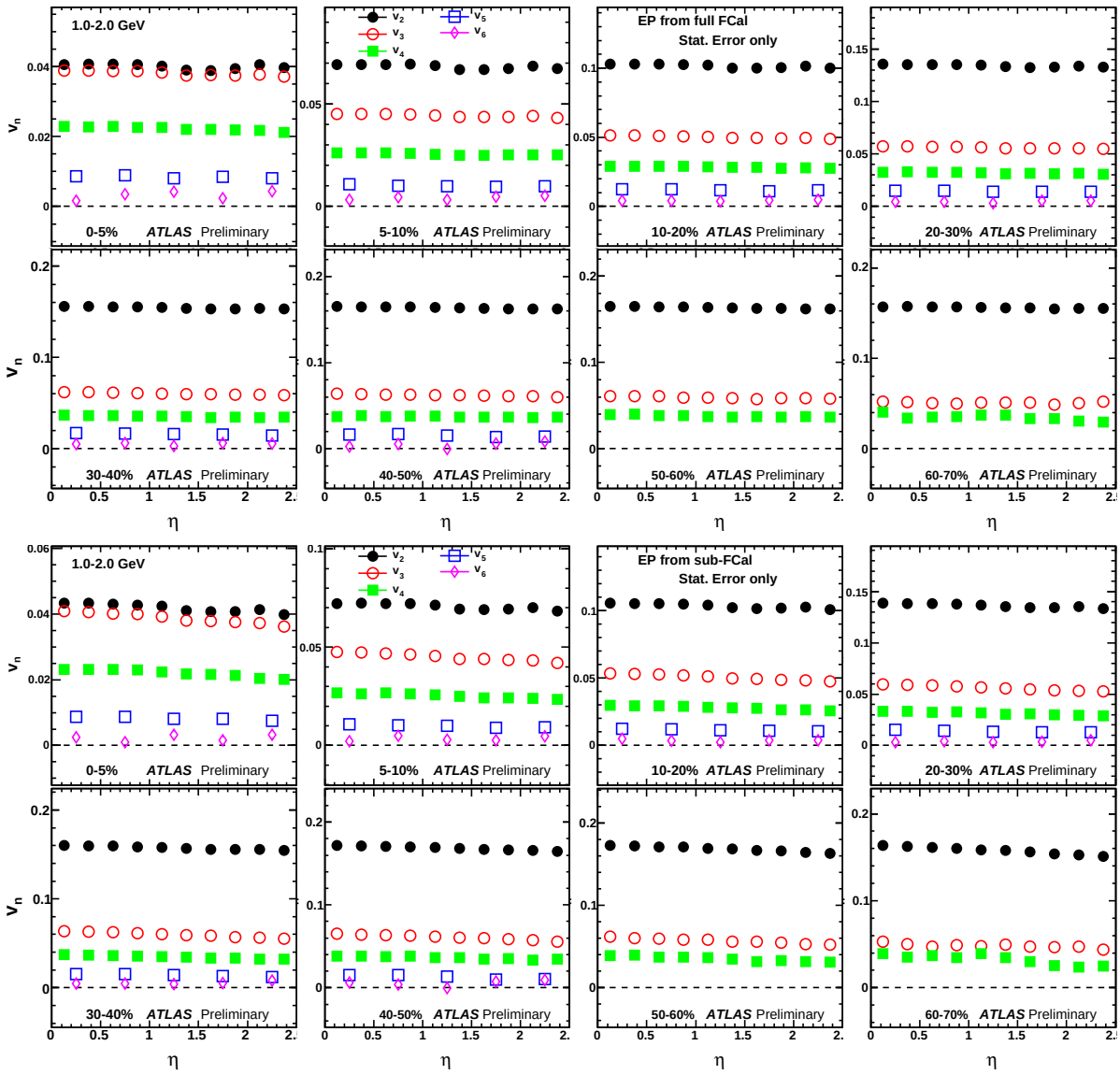

Figure 51: same as previous figure except for 1-2 GeV

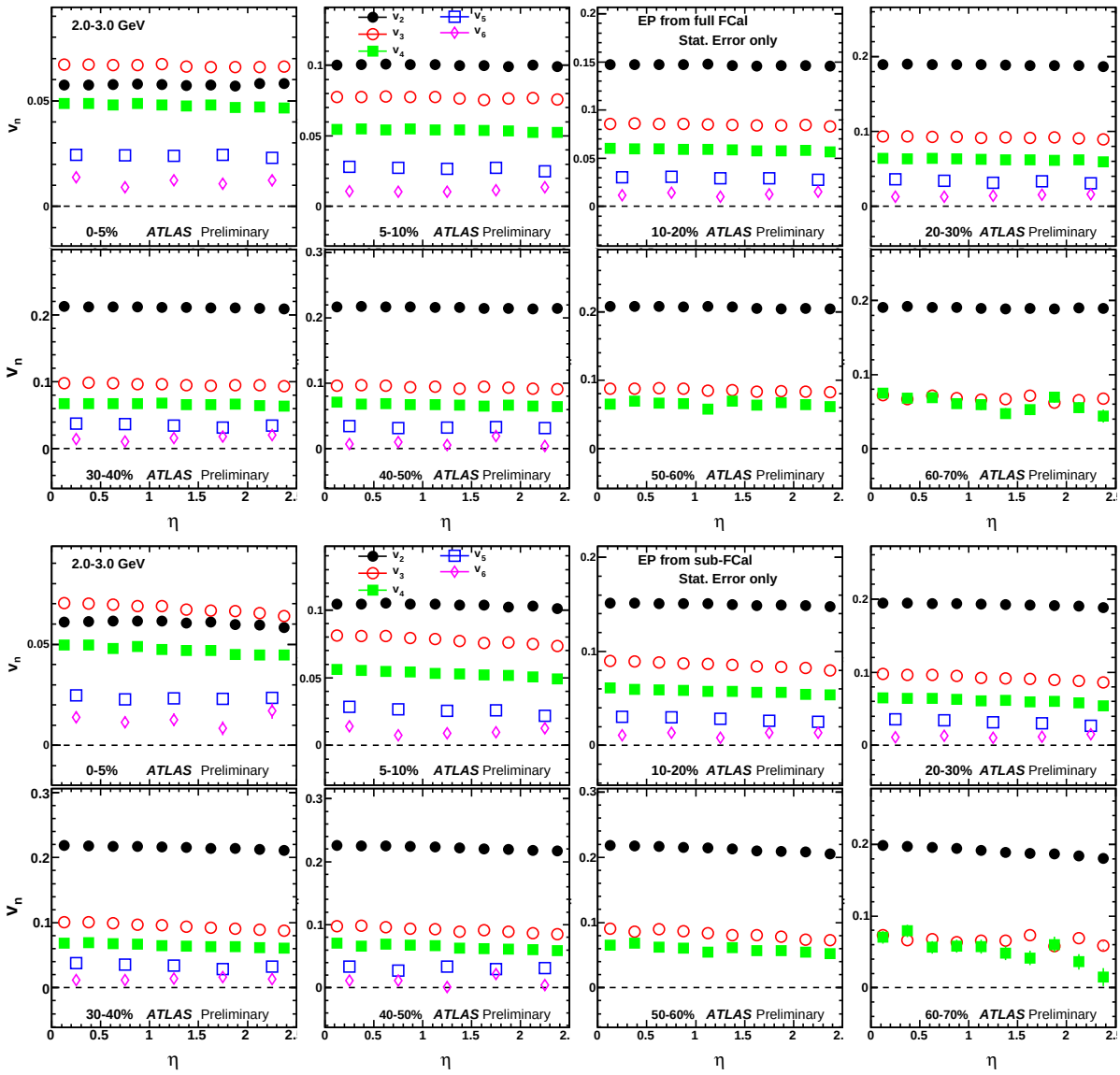

Figure 52: same as previous figure except for 2-3 GeV

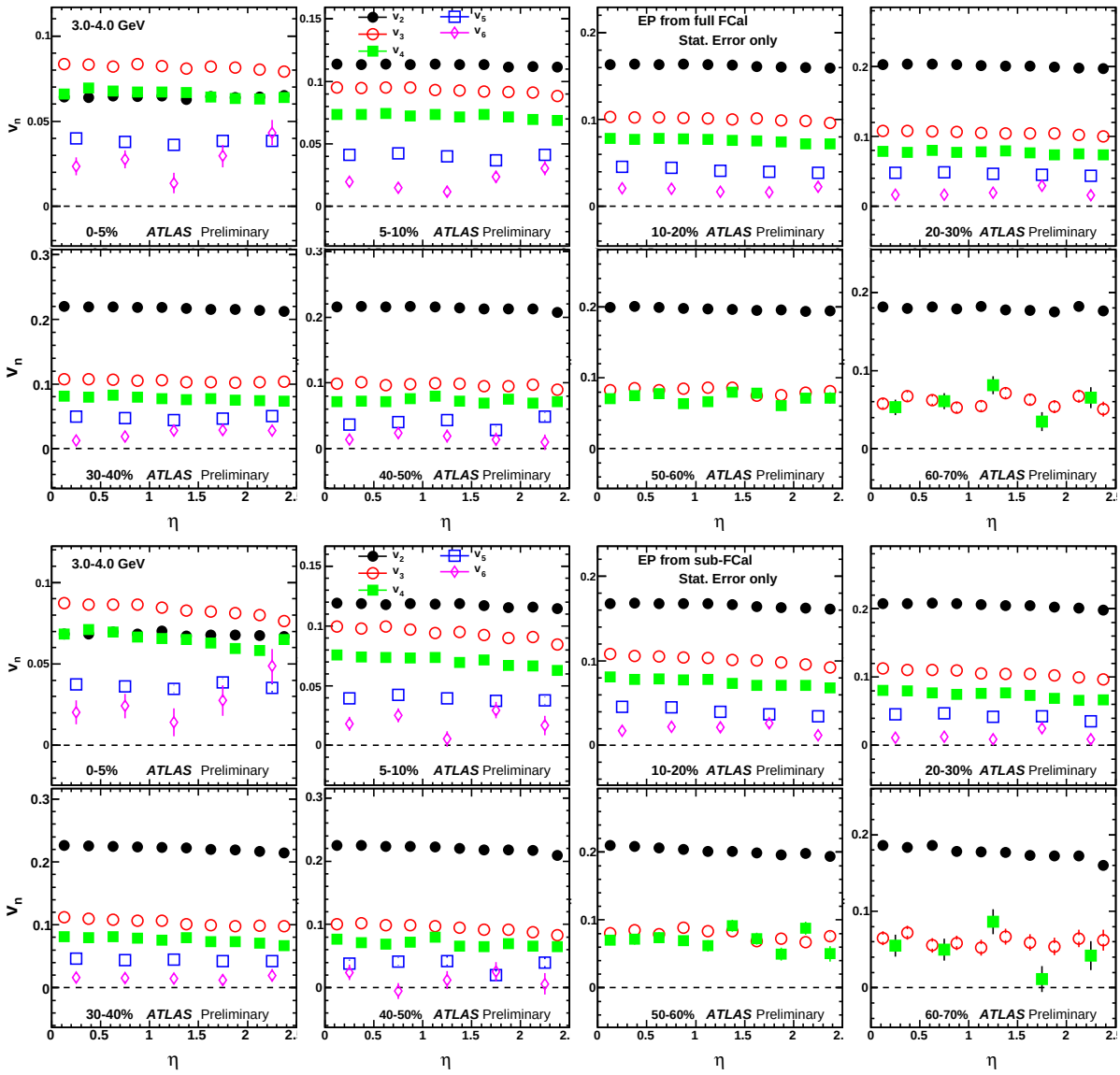

Figure 53: same as previous figure except for 3-4 GeV

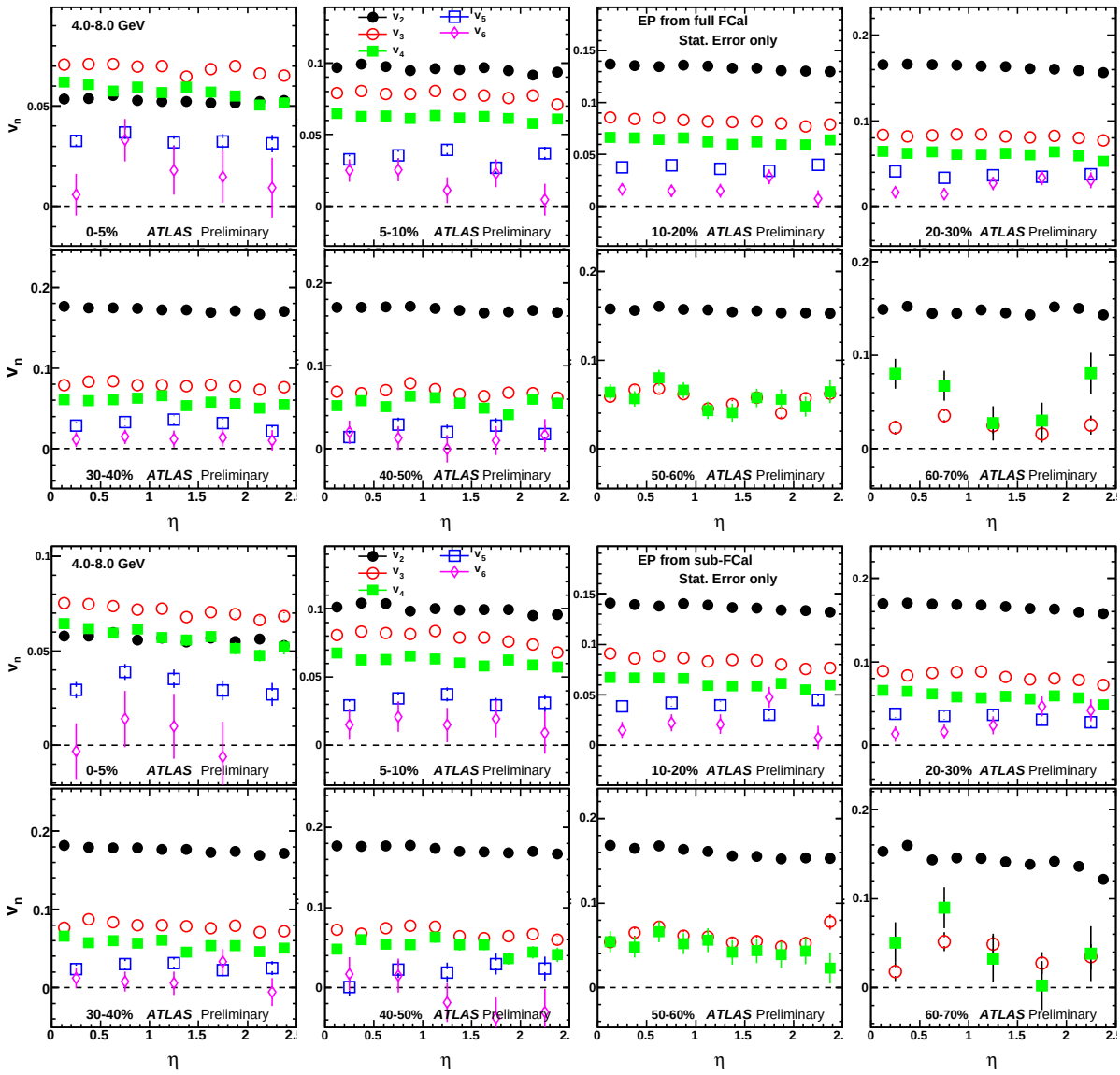

Figure 54: same as previous figure except for 4-8 GeV

6.2 v_n vs p_T

Figure55 shows the p_T dependence of v_2-v_6 for several centrality selections. We see that they all show a similar p_T dependence trend, namely, they first increase with p_T to about 3-4 GeV, then decrease with p_T. However, the overall magnitude of the v_n generally decrease for larger n, except in most central bins where the v_3 seems to be the largest.

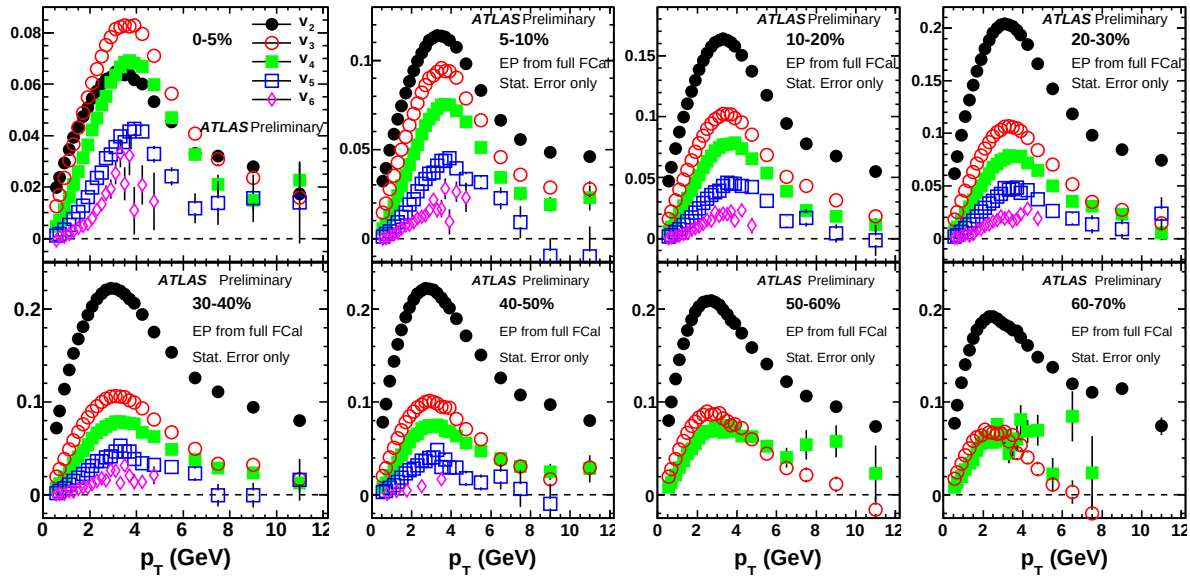

Figure 55: p_T dependence of v_n. Each panel corresponds to a different centrality class.

We notice that the rate with which the v_n reach the corresponding maximum also depends on n. It has been argued that the v_n is controlled by the eccentricity ϵ_n, and it has been shown that the ϵ_n scales as r^n. Thus we calculate $\epsilon_n^{1/n}$, and scale it relative to $\epsilon_2^{1/2}$. The result is shown in Figure 56. We see that the ratios only depend weakly on p_T, suggesting that the that this scaling properly account for the p_T dependence (with in 10%). However the magnitude of the ratios seem to vary slightly with n and centrality.

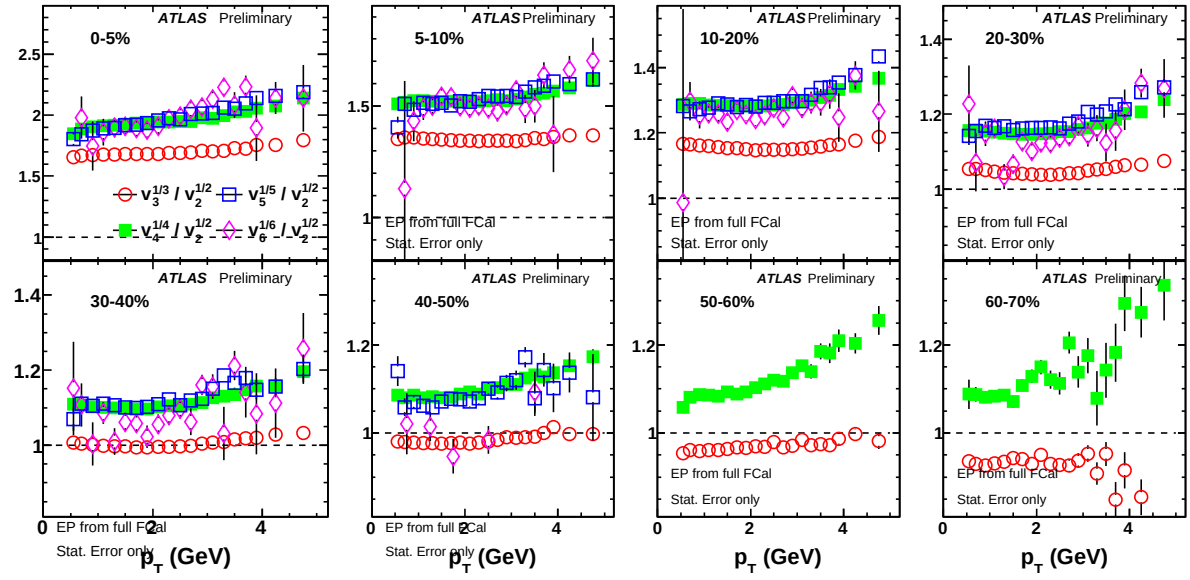

Figure 56: v_n scaling with p_T. The plotted quantity is $\frac{v_n^{1/n}}{v_2^{1/2}}$.

6.3 v_n vs centrality

Figure57 shows the centrality dependence of the v_n for several p_T bins. The centrality bins are 5% in width, but we have a special bin for the top 1% most central events. This bin is importance, when we compare the results obtained here to the ones obtained from the two-particle correlation analysis. Similar results for 10% centrality binning is shown in Figure58. Going from central to peripherial collisions, v_2 first increases, reaches maximum at around 30-40% centrality, and then decreases; v_3 shows a similar but much weaker centrality dependence; while v_4-v_6 almost show no clear centrality dependence trend. We also see that the tail end of the centrality dependence (that is at peripheral events) v_2 again increases. And the higher in p_T we go, the earlier (in centrality) this upward appears. This tail indicates the breakdown of collective behavior and the emergence of the jet influence. We see that this bending near the tail is much less prominent for other harmonics. This is because the jet shape has a natural v_2 in it (due to its back-to-back nature), but doesnot have v_3, v_4 etc.

We also notice that in general v_2 is much larger than the other harmonics. This is because the fireball produced in the collisiosn has a natural ϵ_2 which translates into large v_2. However, in the most central events (in the top 5% and more so in the top 1%) which correspond to (almost) complete overlap between the colliding nuclei, there is no natural ϵ_2 present in the fireball. In these events, all eccentricities come from fluctuations in the initial shape of the fireball. A very interesting thing we see from the centrality plots in that for these top 5% most central events, the v_3 values are larger than the v_2 , and in some p_T bins, even v_4 and v_5 are larger than v_2.

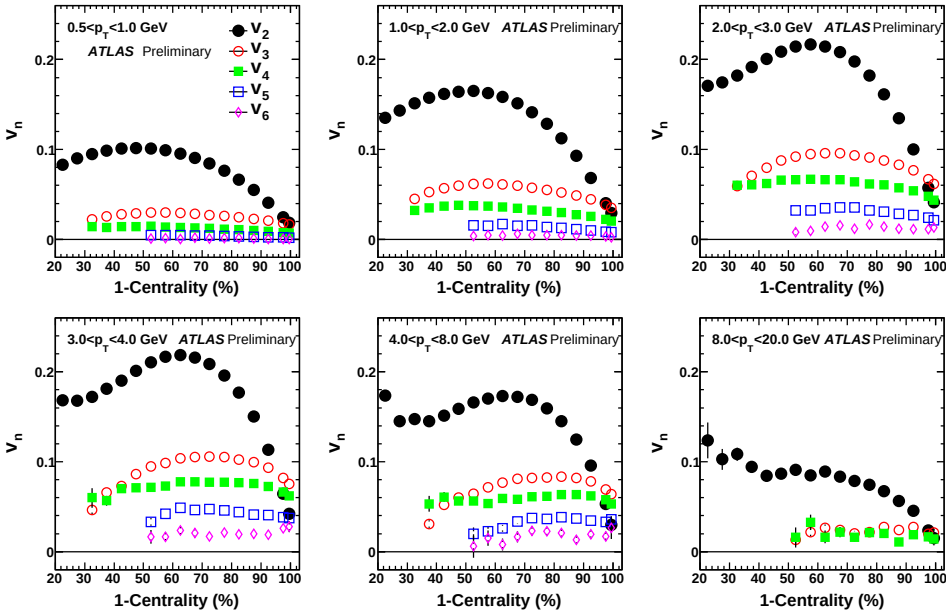

Figure 57: v_n as a function of centrality for different p_T bins in 5% centrality steps plus a 0-1% most central bin. The right-hand end of the X-axis corresponds to most central and the origin corresponds to peripheral events.

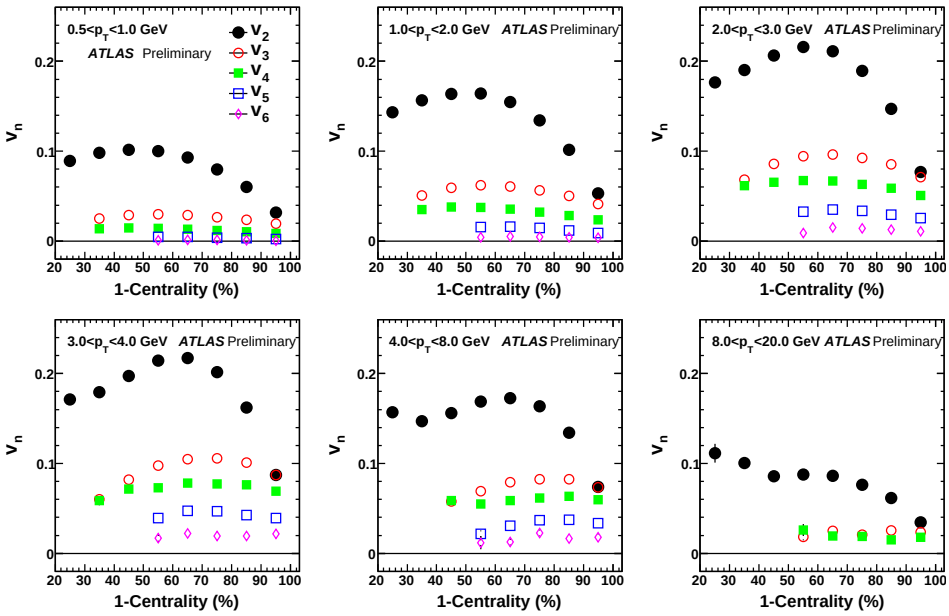

Figure 58: v_n as a function of centrality for different p_T bins in 10% centrality steps. The right-hand end of the X-axis corresponds to most central and the origin corresponds to peripheral events.

6.4 Comparision between results for full FCal and FCal$_{P(N)}$

Figure shows the ratios of v_n obtained from from FCal$_{P(N)}$ to those obtained full FCal for various centrality selections. The FCal$_{P(N)}$ results are higher than those from full FCal for v_2 by about 5%, but the difference decreases towards mid-central collsions to about 2%. However, the differene is almost independent of p_T, except for most central 0-5% and peripheral collisions (> 70%).

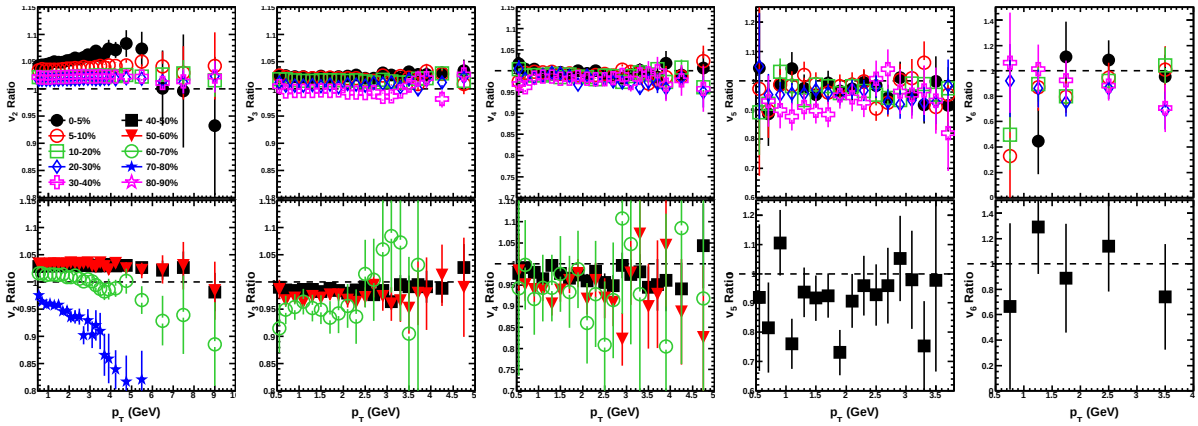

Figure 59: Ratios of v_n obtained from FCal$_{P(N)}$ to those obtained from full FCal for various centrality selections (0-40% for top panels and 40-80% in the bottom panels). From left to right, they are $v_2 - v_6$.

To further dissect these systematic differences. In Figure 60, we plot the v_n ratios between FCal$_{P(N)}$ and full FCal as function of η for 1-2 GeV and for various centrality selections. Again we see that the FCal$_{P(N)}$ results are sytematically higher than those from full FCal. For v_2, the ratios decrease slightly

with η suggesting that the full FCal has weaker η dependence; in most peripheral collisions (eg 70-80%), the ratio drops by amost 20%, this just reflects the fact that the $\text{FCal}_{P(N)}$ has a much stronger η dependence while full FCal has none. The reason as we explained before is due to the fact that the full FCal has more influence from di-jet which bias the RP measurement due to a smaller η gap between ID and full FCal. For $n > 2$, we see the ratios drops with η by about 10% indepdent of centrality selections, again suggesting that $\text{FCal}_{P(N)}$ has stronger η dependence. Similar comparisons of η dependence for other p_T bins can be found in Appendix. However based on these observations, we concluded that the differences between the full FCal and $\text{FCal}_{P(N)}$ are within 1-5% for η integrated results, the only outlier would be the v_2 in 0-5% central collisions which shows about 5% difference.

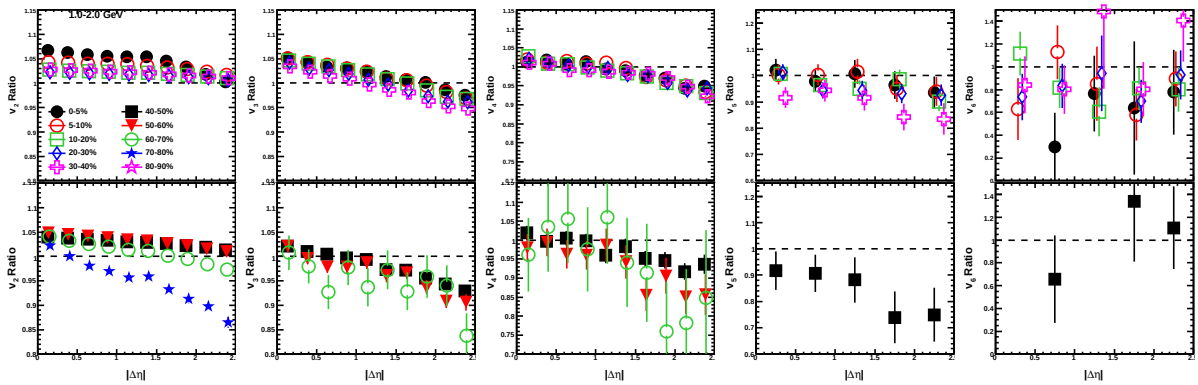

Figure 60: Ratios of the v_n from $\text{FCal}_{P(N)}$ to those obtained from full FCal for 1-2 GeV for various centrality selections. From the left to right they are v_2, v_3, v_4, v_5 and v_6, respectively.

6.5 Comparision with the v_2 from the elliptic flow paper

There is an independent analysis of v_2 carried out by the Krakow flow group. They employed a different EP calibration procedure, in which they re-weight the tower energy of the FCal to make the EP to be flat, instead of applying a shifting and flattening procedure used in our analysis. The other difference is that we include events in z vertex in range of $|z_{vtx}| < 150mm$ while the Krakow group only use events in $|z_{vtx}| < 100mm$. So the natural question is how well our measurement compare with theirs. Figure 61 plot the ratio of the v_2 obtained from our analysis to those from the flow paper (ATLAS-HION-2011-05-001). The green band indicate our systematic error on the reactional plane resolution estimated by comparison between two sub-event-method and three-sub-event methods. The two measrements show excellent agreements within errors.

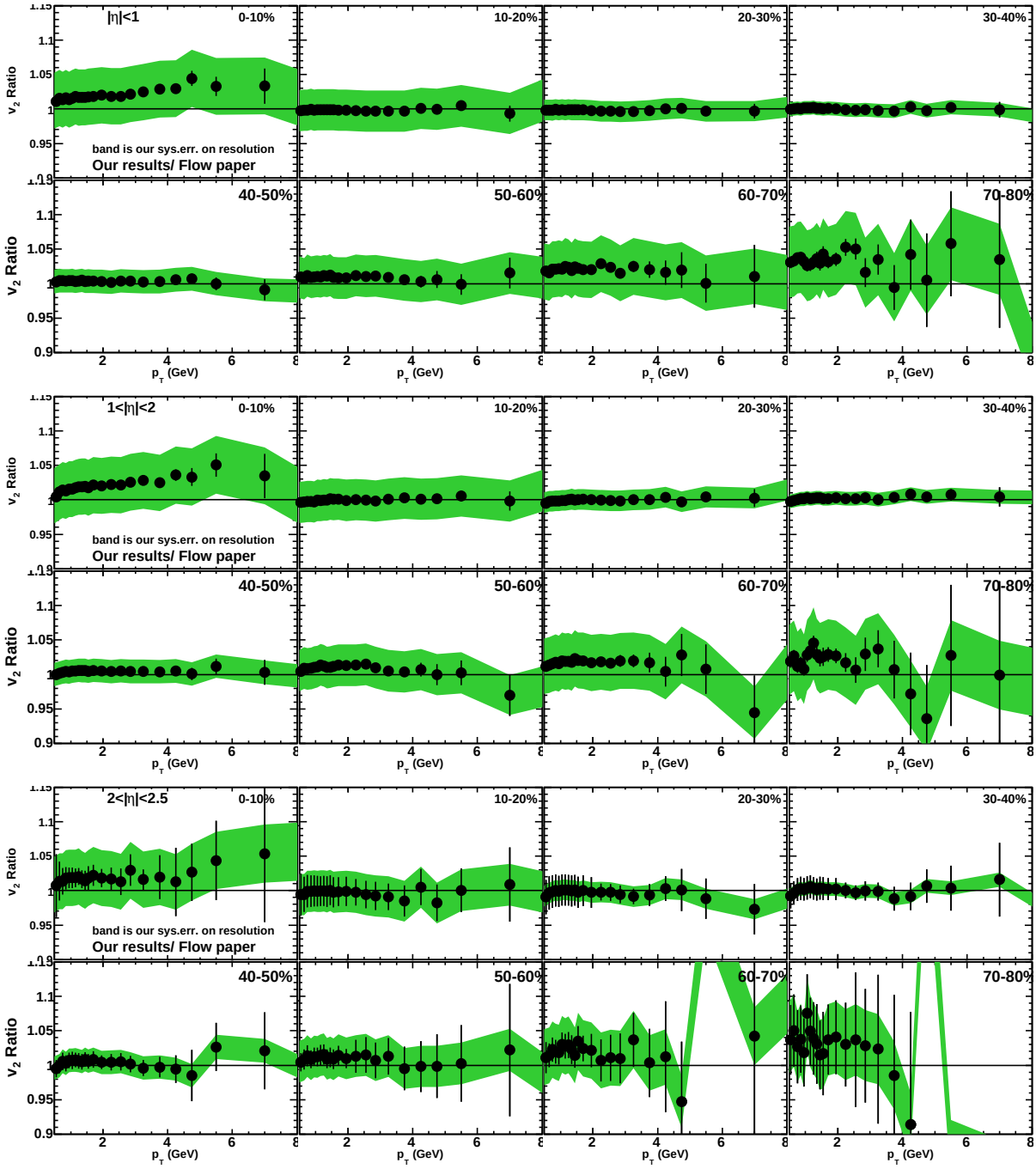

Figure 61: comparison of v_2 from this analysis for $\mathrm{FCal}_{P(N)}$ with flower paper (ATLAS-HION-2011-05-001) results in $|\eta| < 1$ (top), $1 < |\eta| < 2$ (middle) and $2.0|\eta| < 2.5$ (bottom).

7 Appendix

7.1 more comparison between full FCal and Fcal$_{P(N)}$

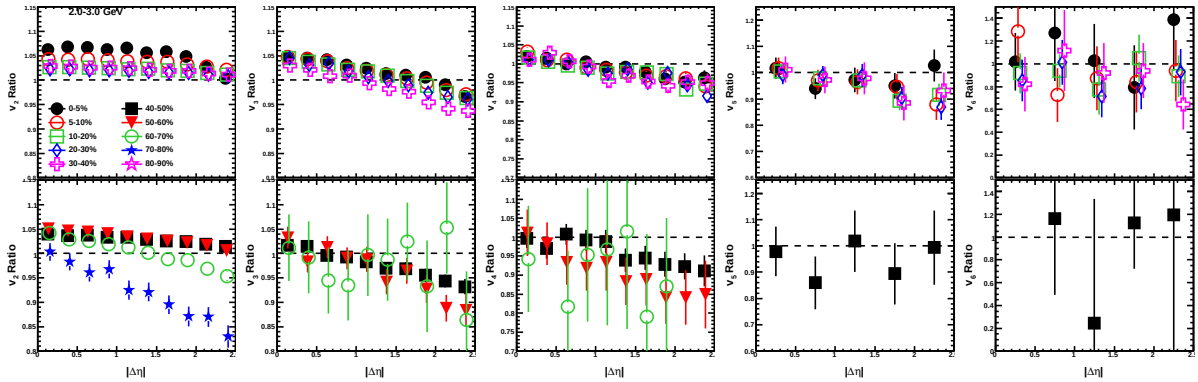

Figure 62: Ratios of the v_n from the full FCal to that for the FCal$_{P(N)}$ for 2-3 GeV for various centrality selections. From the left to right they are v_2, v_3, v_4, v_5 and v_6, respectively.

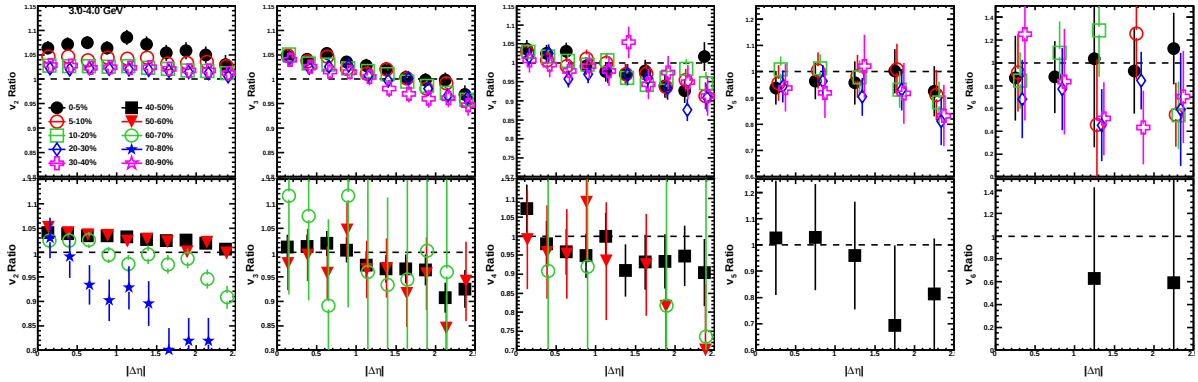

Figure 63: Ratios of the v_n from the full FCal to that for the FCal$_{P(N)}$ for 3-4 GeV for various centrality selections. From the left to right they are v_2, v_3, v_4, v_5 and v_6, respectively.

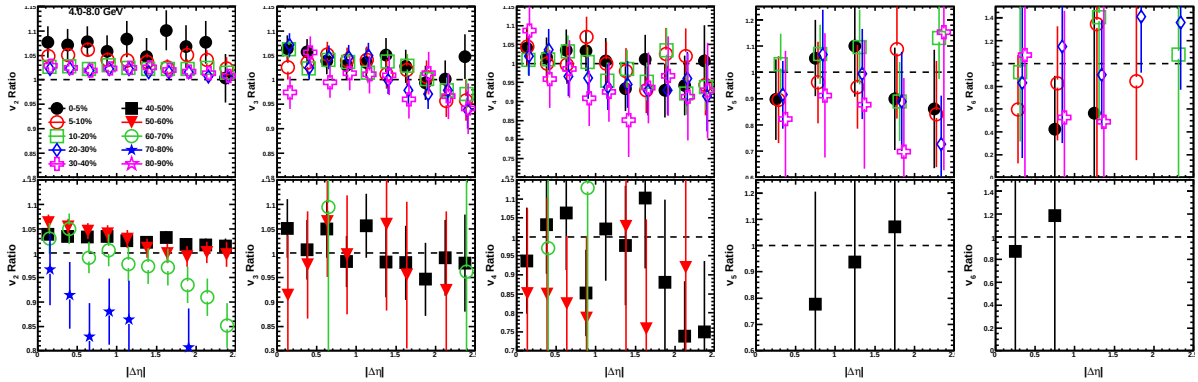

Figure 64: Ratios of the v_n from the full FCal to that for the FCal$_{P(N)}$ for 4-8 GeV for various centrality selections. From the left to right they are v_2, v_3, v_4, v_5 and v_6, respectively.

7.2 Determining the reaction plane angle

Here we explain the method used for determining the reaction plane angle. The measured anisotropy for a given detector, where the RP angle is estimated, can be expressed as a Fourier series,

$$\begin{aligned} 2\pi dN/d\phi &= Q_0 + \sum_n (Q_{x,n}\cos n\phi + Q_{y,n}\sin n\phi) \\ &= Q_0 + \sum_n Q_n \cos n(\phi - \Psi_n), \\ &= Q_0(1 + \sum_n 2v_n^{\rm obs}\cos n(\phi - \Psi_n)), \end{aligned} \tag{23}$$

with

$$\begin{aligned} &Q_{x,n} = \sum_i w_i \cos n\phi_i,\ \ Q_{y,n} = \sum_i w_i \sin n\phi_i, \\ &Q_n^2 = Q_{x,n}^2 + Q_{y,n}^2,\ \ \Psi_n = \frac{1}{n}\tan^{-1}\left(\frac{Q_{y,n}}{Q_{x,n}}\right), \end{aligned} \tag{24}$$

and

$$v_n^{\rm obs} = \frac{Q_n}{2Q_0} = \frac{Q_n}{2\sum_i w_i} \equiv \langle \cos\left(n(\phi - \Psi_n)\right)\rangle\,. \tag{25}$$

w_i is the appropriate weight for each detector channel, be it number of charged particles, or total transverse energy. Ψ_n is n'th order event plane (EP) defined by the n'th order flow vector

$$\overrightarrow{Q_n} = (Q_{x,n}, Q_{y,n}) = (Q_n\cos n\Psi_n, Q_n \sin n\Psi_n), \tag{26}$$

and the usual definition of raw flow coefficient $v_n^{\rm obs}$, is simply the magnitude of the flow vector Q_n normalized by twice of the total weight (or twice number of particles if $w_i = 1$). Ψ_n could be different from the n'th order true reaction plane, $\Psi_{\rm RP,n}$, due to finite multiplicity fluctuations. One may also

measure the kn'th order $\overrightarrow{Q_{kn}}$ and $v_{kn}^{\rm obs}$ from n'th order event plane Ψ_n for any natural number k. This is because of different order of harmonics flow may correlated with each other, and such correlation may result in measureable higher order flow relative to the lower order EP. $v_{kn}^{\rm obs}$ determined this way is known as the mixed harmonics flow coefficient.

Once the event plane angle Ψ_n is determined using forward detectors, the flow signal for tracks at mid-rapidity, can be expressed as (similar to Eq.25),

$$dN/d\phi = A(1 + 2\sum_n v_n^{\rm obs}\cos n(\phi - \Psi_n)) \tag{27}$$

7.3 Reaction plane resolution

Due to finite statistics in the determination of the reaction plane (or $Q-vector$), the measured reaction plane is different than the true reaction plane. We now consider how the difference between the true reaction plane and the observed reaction plane affects the measured harmonics and how we can correct for this. For deriving most of the results in this section, we follow the work done in [REFERENCES]. We denote the true $n'th$ order reaction plane by Ψ_n^{true} and the observed reaction plane by Ψ_n^{obs}. The distribution of particles can now be written as:

$$\begin{aligned} N(\phi) &= N_0\left(1 + 2v_n cos(n(\phi - \Psi_n^{true}))\right) \\ &= N_0\left(1 + 2v_n cos\left(n(\phi - \Psi_n^{obs}) - n(\Psi_n^{obs} - \Psi_n^{true})\right)\right) \\ &= N_0\left(1 + 2v_n cos\left(n(\phi - \Psi_n^{obs})\right) cos\left(n(\Psi_n^{obs} - \Psi_n^{true})\right)\right) \\ &\quad + N_0\left(2v_n sin\left(n(\phi - \Psi_n^{obs})\right) sin\left(n(\Psi_n^{obs} - \Psi_n^{true})\right)\right) \end{aligned} \tag{28}$$

Note that by Ψ_n^{obs} we mean the observed reaction plane that has been corrected for all systematic detector effects. Thus any difference between Ψ_n^{obs} and Ψ_n^{true} is purely because of the finite statistics used in the determination of Ψ_n^{true}. Assuming that the fluctuations of the observed reaction plane about the true reaction plane are independent of the true reaction plane[REFERENCE Probably not necessary], that is, the $\Delta\Psi_n (= \Psi_n^{obs} - \Psi_n^{true})$ distribution is independent of Ψ_n^{true}, we have:

$$\left\langle cos\left(n(\phi - \Psi_n^{obs})\right) cos\left(n(\Psi_n^{obs} - \Psi_n^{true})\right)\right\rangle = \left\langle cos\left(n(\phi - \Psi_n^{obs})\right)\right\rangle \left\langle cos\left(n(\Psi_n^{obs} - \Psi_n^{true})\right)\right\rangle \tag{29}$$

$$\left\langle sin\left(n(\phi - \Psi_n^{obs})\right) sin\left(n(\Psi_n^{obs} - \Psi_n^{true})\right)\right\rangle = \left\langle sin\left(n(\phi - \Psi_n^{obs})\right)\right\rangle \left\langle sin\left(n(\Psi_n^{obs} - \Psi_n^{true})\right)\right\rangle \tag{30}$$

Now, since the fluctuations of the observed reaction plane about the true reaction plane must be symmetric (that is, the probability of $\Psi_n^{obs} - \Psi_n^{true}$ to be $+\Delta\Psi_n$ and $-\Delta\Psi_n$ are the same), when averaged over many events we must have:

$$\left\langle sin\left(n(\Psi_n^{obs} - \Psi_n^{true})\right)\right\rangle = 0 \tag{31}$$

Thus the particle yield averaged over many events can be written as:

$$N(\phi) = N_0\left(1 + 2v_n \times \left\langle cos\left(n(\Psi_n^{obs} - \Psi_n^{true})\right)\right\rangle \times cos\left(n(\phi - \Psi_n^{obs})\right)\right) \tag{32}$$

We see that the difference between the observed reaction plane and the true reaction plane effectively reduces the measured value of v_n by a factor of $\left\langle cos\left(n(\Psi_n^{obs} - \Psi_n^{true})\right)\right\rangle$. We define this factor as the reaction plane resolution (for the nth-order harmonic) of the detector:

$$Resolution = \left\langle cos\left(n(\Psi_n^{obs} - \Psi_n^{true})\right)\right\rangle \tag{33}$$

Once the resolution is determined, the true value of v_n can me obtained by dividing the observed value by the resolution. That is:

$$v_n = \frac{v_n^{obs}}{\left\langle cos\left(n(\Psi_n^{obs} - \Psi_n^{true})\right)\right\rangle} \tag{34}$$

7.4 Mixed harmonics

Here we explain the concept of mixed harmonics. Mixed harmonics mean the value of the m^{th} order harmonic in the n^{th} order plane. For example the v_4 measured in the Ψ_2 plane is a mixed harmonic (which will be smaller than v_4 about Ψ_4 plane). Let us start with our master equation for the particle distribution and write it about the Ψ_n plane.

$$\begin{aligned}\frac{dN}{d\phi} &= N_0\left(1 + \sum_{m=1}^{\infty} 2v_m cos(m(\phi - \Psi_m))\right) \\ &= N_0\left(1 + 2v_n cos(n(\phi - \Psi_n)) + \sum_{m\neq n}^{\infty} 2v_m cos(m(\phi - \Psi_n) - m(\Psi_m - \Psi_n))\right)\end{aligned} \tag{35}$$

When averaged over many events, the $m \neq n$ terms become:

$$\langle cos(m(\phi - \Psi_n) - m(\Psi_m - \Psi_n))\rangle = \langle cos(m(\phi - \Psi_n))\rangle \langle cos(m(\Psi_m - \Psi_n))\rangle \tag{36}$$

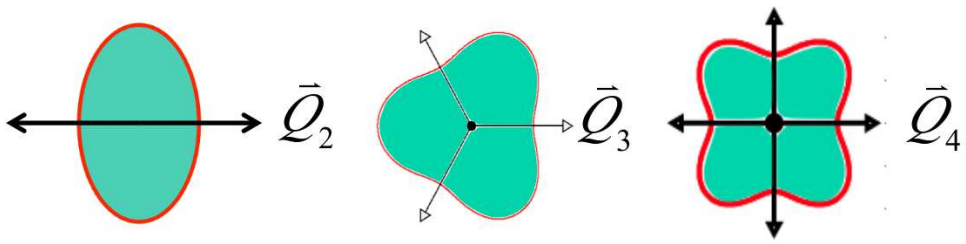

Figure 65: The elliptic, triangular and square anisotropies. Notice the two fold degeneracy in ϵ_2, three fold degeneracy in ϵ_3 and four fold degeneracy in ϵ_4 .

Now Ψ_m has an $m - fold$ ambiguity (or degeneracy) in its defenition (see fig.65) while Ψ_n has an n-fold ambiguity. While picking the Ψ_n (or Ψ_m) plane, we get at random one of these n (or m) values. If the n different values of the reaction plane Ψ_n are represented by Ψ_n^i with $(i = 1, 2, ...n)$ then $m \times \Psi_n^i$ will differ from each other by a multiple of 2π if m is an exact multiple of n. Thus if $m = kn$ (where k is an integer), $cos(m(\Psi_m - \Psi_n^i))$ will be the same no matter which of the Ψ_n^i we pick. However, if $m \neq kn$, then $cos(m(\Psi_m - \Psi_n^i))$ will be different for each Ψ_n^i and will be average to zero (when averaged over many events).

Thus the particle distribution averaged over many events about the Ψ_n plane can be written as (keeping only the $m = kn$ terms):

$$\frac{dN}{d\phi} = N_0\left(1 + 2v_n cos(n(\phi - \Psi_n)) + \sum_{k=2}^{\infty} 2v_{kn}\left\langle cos(m(\Psi_m - \Psi_n))\right\rangle cos(nk(\phi - \Psi_n))\right)$$
$$= N_0\left(1 + \sum_{k=1}^{\infty} 2\widehat{v_{kn}} cos(kn(\phi - \Psi_n))\right) \quad (37)$$

Where

$$\widehat{v_{kn}} = v_{kn}\left\langle cos(m(\Psi_m - \Psi_n))\right\rangle \quad (38)$$

For $k = 1$ obviously $\widehat{v_{kn}} = v_n$. From Eq.38, we see that the mixed harmonics directly measure the correlation of the Ψ_m plane with the Ψ_n plane. And also that the mixed harmonic $\widehat{v_{kn}}$ will always be smaller than v_{kn} as $\langle cos(m(\Psi_m - \Psi_n))\rangle \leq 1$.

7.5 Event plane flattening [put references here]

The distribution of the true reaction plane should be flat. This means that when averaged over many events, the reaction plane (or the $Q - vector$) doesnt have any preferred direction. However due to detecter effects such as inefficiencies/dead-regions/hot-regions, the raw event-plane distribution is not flat. For example, if the Forward calorimeter has a few towers with higher gains than the rest, then the $Q - vector$s will get more contribution from these towers, and will have a tendency to align along them. Similarly dead modules in the pixel detectors will result in the $Q - vector$ having less contribution fomr these regions and will be aligned opposite to these modules. In order to account for these detector effects on the on the $Q - vector$ (and in turn on the reaction plane), a recentering-flattening procedure us used to correct the reaction plane distribution.

In order to deomstrate the non-flatness of the raw EP (denoted as Ψ_n^{Raw}), we plot the distributions of Ψ_2^{Raw} and Ψ_3^{Raw} obatined from the FCal for a few centralities in Fig.66. (Note by FCal, we always mean layers 1 and 2 of the FCal and $\eta \in (3.3, 4.8)$).

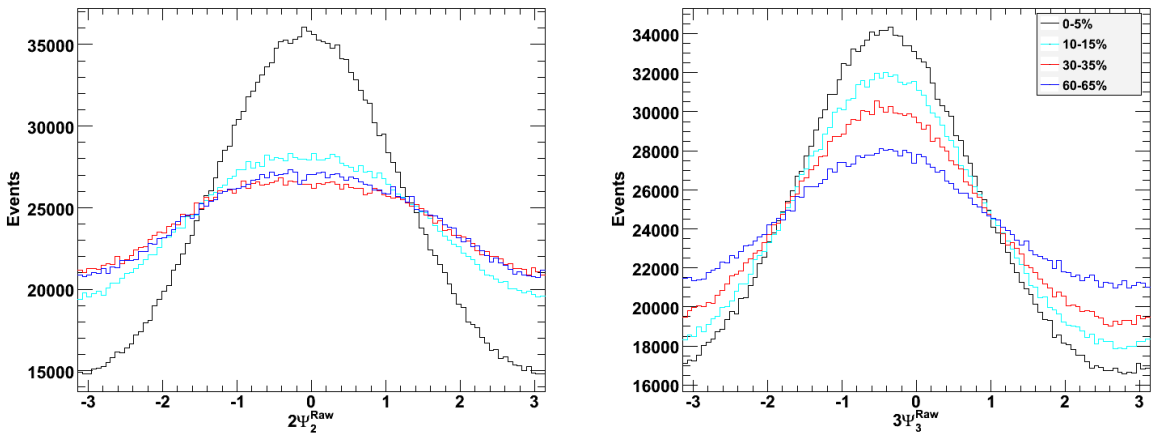

Figure 66: The Event Plane distribution for Ψ_2^{Raw} and Ψ_3^{Raw} obatined from FCal for four different centralities. The error bars should be $\sqrt{N_{Events}}$ and are suppressed for calrity.

7.5.1 Recentering and rescaling of the $Q-vector$

As mentioned before, the true $Q-vector$ distribution distribution doesnot have any prefered direction. Thus, we must have :

$$\langle Q_{n,x} \rangle = \left\langle Q_{n,y} \right\rangle = 0 \tag{39}$$

Since the raw $Q-vectors$ averaged over many events, have x and y components, the $Q-vector$ is recentered at (0,0) by subtracting these out. This recentering procedure is done order by order for all $Q-vectors$. Also since the mean values of the raw $Q-vectors$ depend on the centrality, this recentering in done is narrow bins of centrality (5% bins in our case).

$$\begin{aligned} Q_{n,x}^{recentered} &= Q_{n,x}^{Raw} - \langle Q_{n,x}^{Raw} \rangle \\ Q_{n,x}^{recentered} &= Q_{n,x}^{Raw} - \langle Q_{n,x}^{Raw} \rangle \end{aligned} \tag{40}$$

Further, the $Q-vectors$ are renormalized to have a mean value of 1.0. This is acheieved by scaling the recentered $Q-vector$ by the $\sigma_{x/y}$ of the raw $Q-vector$ distribution. As with the recentering, the rescaling is again done in narrow centrality bins. The rescaling of the $Q-vector$ doesnot have any effect on the reaction plane and is only for plotting purposes and for comparing the distributions across different centralities. We denote the $Q-vector$ obatined after the recentering and rescaling as Q^{meas}. Thus the whole recentering and rescaling procedure can be written as:

$$\begin{aligned} Q_{n,x}^{meas} &= \left(Q_{n,x}^{Raw} - \langle Q_{n,x}^{Raw} \rangle \right) / \sigma_{n,x} \\ Q_{n,y}^{meas} &= \left(Q_{n,y}^{Raw} - \langle Q_{n,y}^{Raw} \rangle \right) / \sigma_{n,y} \end{aligned} \tag{41}$$

7.5.2 Flattening of the event plane

After recentering the $Q-vector$ the event-plane distributions Ψ_n^{meas} are almost flat. Further corrections involve shifting the event plane by small angle $\Delta\Psi_n$:

$$\Delta\Psi_n = \sum_{k=1}^{k_{max}} \frac{2}{kn} \left(-\langle sin(kn\Psi_n^{meas}) \rangle cos(kn\Psi_n^{meas}) + \langle cos(kn\Psi_n^{meas}) \rangle sin(kn\Psi_n^{meas}) \right) \tag{42}$$

Where $k_{max} = 12$ in our analysis. Finally the fully corrected reaction plane is obtained as :

$$\Psi_n = \Psi^{meas} + \Delta\Psi_n \tag{43}$$

In Fig.67 we plot the raw, recentered and flattened Event planes for two different centralities for $n = 2, 3, 4, 5, 6$. From the plots it is clear that the recentering take care of most of the detector anisotropies and the flattening only makes minor modifications.

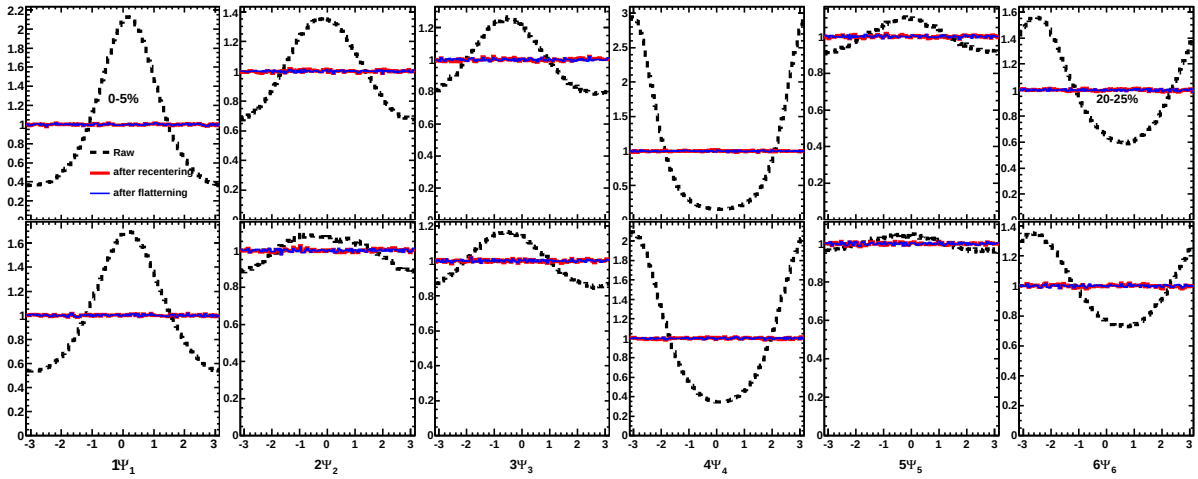

Figure 67: The raw, recentered and flattened distributions for Ψ_2 obatined using FCal (layer1+layer2)

7.5.3 Meaning of the shifts $\langle Q^{Raw}_{n,x/y} \rangle$

We not take a detailed look at the shifts $\langle Q^{Raw}_{n,x/y} \rangle$. First we explain what these $\langle Q^{Raw}_{n,x/y} \rangle$ mean physically. Measured with a calorimeter, the Q-vectors are simply the azimuthal distribution of the transverse energy(E_T). The Q-vector in a particular event can be written as a function of phi as:

$$Q^{True}(\phi) = Q_0 \left(1 + \sum_{n=1}^{\infty} 2v_n \cos(n\phi - n\psi_n) \right)$$

However the measured raw energy distribution will be affected by the detector efficiency ϵ, and we have:

$$Q^{Raw}(\phi) = Q^{True}(\phi) \times \epsilon(Q^{True}(\phi), \phi) \tag{44}$$

Where we have assumed that the efficiency is both a function of the true deposited energy $Q^{True}(\phi)$ and the angle ϕ. If we relax this assumption to make the efficiency only a function of ϕ, then we have:

$$Q^{Raw}(\phi) = Q^{True}(\phi) \times \epsilon(\phi) \tag{45}$$

Now the efficiency function can be expanded in a Fourier series (whose form we keep similar to our flow expansion):

$$\epsilon(\phi) = \epsilon_0 \left(1 + \sum_{n=1}^{\infty} 2\epsilon_n \cos(n\phi - n\Phi_n) \right) \tag{46}$$

Substituting this into the expansion of the Raw$Q-vector$, we get:

$$\begin{aligned} Q^{Raw} &= Q_0 \left(1 + \sum_{n'=1}^{\infty} 2v_{n'} \cos(n'\phi - n'\psi_{n'}) \right) \times \epsilon(\phi) \\ &= Q_0 \left(1 + \sum_{n'=1}^{\infty} 2v_{n'} \cos(n'\phi - n'\psi_{n'}) \right) \times \epsilon_0 \left(1 + \sum_{n''=1}^{\infty} 2\epsilon_{n''} \cos(n''\phi - n''\Phi_{n''}) \right) \\ &= \epsilon_0 Q_0 \left(1 + \sum_{n'=1}^{\infty} 2v_{n'} \cos(n'\phi - n'\psi_{n'}) + \sum_{n''=1}^{\infty} 2\epsilon_{n''} \cos(n''\phi - n''\Phi_{n''}) + O(\epsilon_{n'} v_{n''}) \right) \end{aligned} \tag{47}$$

Where we have ignored terms of Order $O(\epsilon_{n'} v_{n''})$ in the above formula (Note that these terms are actually handled by the flattening procedure). This gives us for $Q_{n,x}^{Raw}$ and $Q_{n,y}^{Raw}$

$$Q_{n,x}^{Raw} = \int Q(\phi) \times cos(\phi) d\phi = \epsilon_0 Q_0 \left(2 v_n \cos(n\psi_n) + 2\epsilon_n \cos(n\Phi_n)\right) \quad (48)$$

$$Q_{n,y}^{Raw} = \int Q(\phi) \times sin(\phi) d\phi = \epsilon_0 Q_0 \left(2 v_n sin(n\psi_n) + 2\epsilon_n sin(n\Phi_n)\right) \quad (49)$$

were we to calculate the reaction plane angle ψ_n from the raw Q_n values, we would get :

$$\psi_n^{Raw} = tan^{-1}\left(\frac{\epsilon_0 Q_0 \left(2 v_n sin(n\psi_n) + 2\epsilon_n sin(n\Phi_n)\right)}{\epsilon_0 Q_0 \left(2 v_n cos(n\psi_n) + 2\epsilon_n cos(n\Phi_n)\right)}\right) = tan^{-1}\left(\frac{(v_n sin(n\psi_n) + \epsilon_n sin(n\Phi_n))}{(v_n cos(n\psi_n) + \epsilon_n cos(n\Phi_n))}\right) \neq \psi_n \quad (50)$$

Now we explain how the recentering corrects this. When averaged over many events, as the reaction plane angles (ψ_n) are completely random, we get:

$$\left\langle Q^{Raw} \right\rangle = \epsilon_0 Q_0 \left(1 + \sum_{n''=1}^{\infty} 2\epsilon_{n''} \cos(n''\phi - n''\Phi_{n''})\right) \quad (51)$$

This gives us:

$$\left\langle Q_{n,x}^{Raw} \right\rangle = \int \left\langle Q^{Raw}(\phi) \right\rangle \times cos(\phi) d\phi = \epsilon_0 Q_0 \left(2\epsilon_n \cos(n\Phi_n)\right)$$

$$\left\langle Q_{n,y}^{Raw} \right\rangle = \int \left\langle Q^{Raw}(\phi) \right\rangle \times sin(\phi) d\phi = \epsilon_0 Q_0 \left(2\epsilon_n sin(n\Phi_n)\right) \quad (52)$$

Equations.51 and 52 also give us the physical meaning of $\left\langle Q_n^{Raw} \right\rangle$.Up to a normalization constant Q_0(independent of n), $\left\langle Q_n^{Raw} \right\rangle$ measures the nth harmonic coefficient in the Fourier expansion of the detector efficiency $\epsilon(\phi)$. When we go from one centrality to another, Q_0 will change, but ϵ_0, ϵ_n and Φ_n will remain same. This means that the while the magnitude of $\left\langle Q_n^{Raw} \right\rangle$ changes from one centrality to another, the direction will remain fixed. Further as Q_0 is independent of n, the magnitudes of the different $\left\langle Q_n^{Raw} \right\rangle$ will scale by the same amount going from one centrality to another. That is, if $|\left\langle Q_2^{Raw} \right\rangle|$ change by a factor of $'x'$ going from centrality-1 to centrality-2, then $|\left\langle Q_{2/3/4...}^{Raw} \right\rangle|$will also change by a factor of $'x'$.

Now lets see how accounting for the $\left\langle Q_n^{Raw} \right\rangle$ corrects the measurement of the reaction plane. The recentered (or shifted) $Q_{n,x/y}$ are given by:

$$Q_{n,x}^{recentered} = Q_{n,x}^{Raw} - \left\langle Q_{n,x}^{Raw} \right\rangle = \epsilon_0 Q_0 \left(2 v_n \cos(n\psi_n)\right) \quad (53)$$

$$Q_{n,y}^{recentered} = Q_{n,y}^{Raw} - \left\langle Q_{n,y}^{Raw} \right\rangle = \epsilon_0 Q_0 \left(2 v_n sin(n\psi_n)\right) \quad (54)$$

and calculating the ψ_n from the recentered $Q - vector$, we get:

$$\psi_n^{recentered} = tan^{-1}\left(\frac{Q_{n,y}^{recentered}}{Q_{n,x}^{recentered}}\right) = tan^{-1}\left(\frac{\epsilon_0 Q_0 \left(2 v_n sin(n\psi_n)\right)}{\epsilon_0 Q_0 \left(2 v_n \cos(n\psi_n)\right)}\right) = \psi_n \quad (55)$$

We see that the recentered $Q - vectors$give us the correct reaction plane. We once again note that in Eq.47, we had ignored terms of $O(\epsilon_{n'} v_{n''})$, Had we kept those terms, Eq.55 would be further modified by the term in Eq.42. These terms are accounted for by the flattening procedure.

7.5.4 Shifts $\langle Q^{Raw}_{n,x/y} \rangle$ for the FCal

Now we do a study of the shifts $\langle Q^{Raw}_{n,x/y} \rangle$ for the FCal. This is also presented in the main text, but we show them here again for continuity. We will analyze one run only(run 170002) so that any run-by-run changes in the detector acceptance do not affect our observations. in Fig.68, we plot the $\langle Q^{Raw}_{n,y} \rangle$vs $\langle Q^{Raw}_{n,x} \rangle$ distributions for $FCal - Layer1$ for n=1,2,3,4,5,6. Each harmonic is represented by a different color and the different points for a particular harmonic are for different centralities (20 bins of 5% centrality with the most central one having the highest magnitude). On the right plot, we have rescaled the Q-vectors such that the point corresponding to the most central events (0-5%) has a magnitude of 1.0.

From these figures, we can see the two scaling relations that we had expected in the last section. We see that as the centrality bin changes, the magnitude of the shifts change (as they should), but the direction is extremely stable. We also see the expected scaling in the magnitudes, which is evident from the right plot. When the most central class has been scaled to have $|Q^{Raw}_n| = 1.0$, we see that the other classes have roughly the same magnitude independent of n.

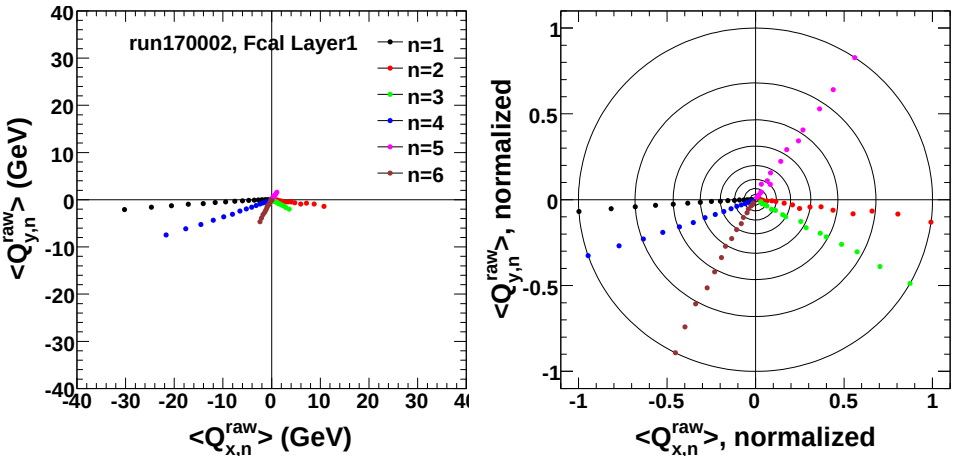

Figure 68: $\left\langle Q^{Raw}_{n,y} \right\rangle$ vs $\left\langle Q^{Raw}_{n,x} \right\rangle$ for $n = 2, 3, 4, 5, 6$. Left Plot is unscaled, right plot is scaled such that the most central(0-5%) bin has $|\left\langle Q^{Raw}_n \right\rangle| = 1.0$.

In Fig. we plot this information again but in polar co-ordinates. The left plot is $|\left\langle Q^{Raw}_n \right\rangle|$ vs $n\Phi_n$, right plot is $|\left\langle Q^{Raw}_n \right\rangle|$ vs Φ_n. We see that the angles are stable independent of centrality. There is some fluctuations in the more peripheral bins, this is because the magnitude $|\left\langle Q^{Raw}_n \right\rangle|$ is very small, so the angle is susceptible to fluctuations.

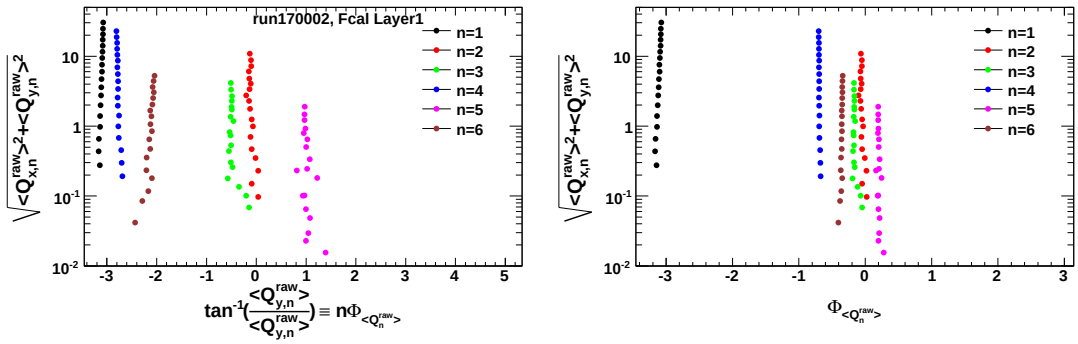

Figure 69: $|\left\langle Q_n^{Raw}\right\rangle|$ vs $angle(\left\langle Q_n^{Raw}\right\rangle)$ for $n = 2, 3, 4, 5, 6$. Left plot is vs $n\Phi_n$, right plot is vs Φ_n

The angles Φ_n can be directly calculated from the $E_T(\phi)$ distribution in the calorimeter averaged over all centralities:

$$\left\langle \frac{dE_T}{d\phi} \right\rangle = \epsilon_0 Q_0 + \sum_{n=1}^{\infty} 2\overline{Q_n^{Raw}} \cos(n\phi - n\Phi_n)$$

Where $\overline{Q_n^{Raw}}$ means (weighted) average of Q_n^{Raw} over all events (in all centralities). We plot this in the left panel of Fig. 70, the vertical lines in the plot show the angles associated with the different harmonics. In the right plot, we show the comparison of these angles obtained by the direct Fourier fit of E_T to the ones obtained during the recentering procedure (from Figs. 68 and 69). We see extremely good agreement between the values. Also from the E_T Fourier fit, we see that n=4 harmonic is the second largest component (after n=1), in fact the background modulation is larger than the true v_4 signal(PUT REFERENCE TO VN PLOT HERE). We also note that the positions of the $n\Phi_n$ values obtained match exactly with the position of the peaks of the $n\Psi_n^{Raw}$ plotted in Fig.67.

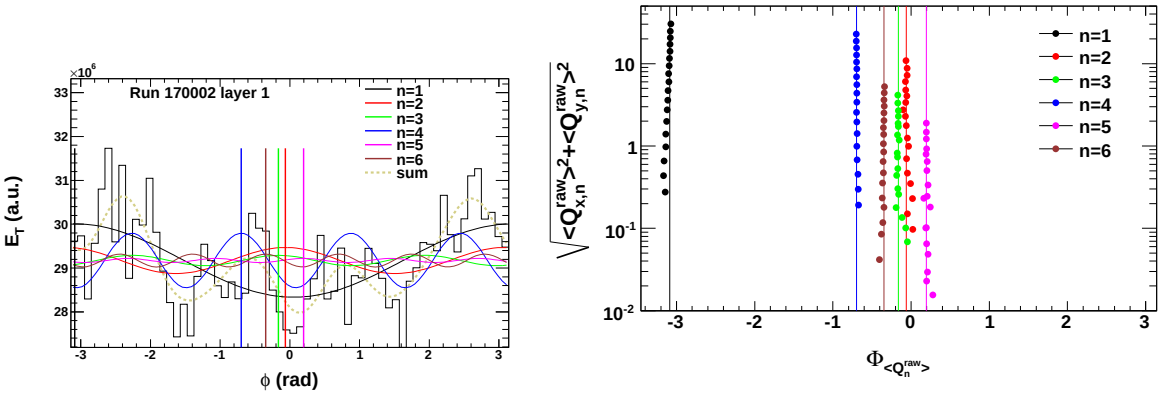

Figure 70: Left plot: Fourier fit to the E_T deposited in FCal(Layer-1), the vertical lines show the angles associated with the different harmonics. Right plot: Comparison between the angles obtained by direct Fourier fit(vertical lines), to the ones obtained from calibration(circular points, each point represents one centrality bin of 5% width).

All the results that we showed in this section pertain to run 170002 only. As mentioned before, we took only one run into consideration so that any run-by-run changes in the detector acceptance do not affect our results. Finally, in Fig. we show the run dependence of these parameters (both the magnitude

and the direction of Q_n^{Raw}) for two different centralities for all 34 runs that we use in our analysis. As is evident from this plot, there is only a small variation in the acceptance/efficiency of the FCal across the 34 runs.

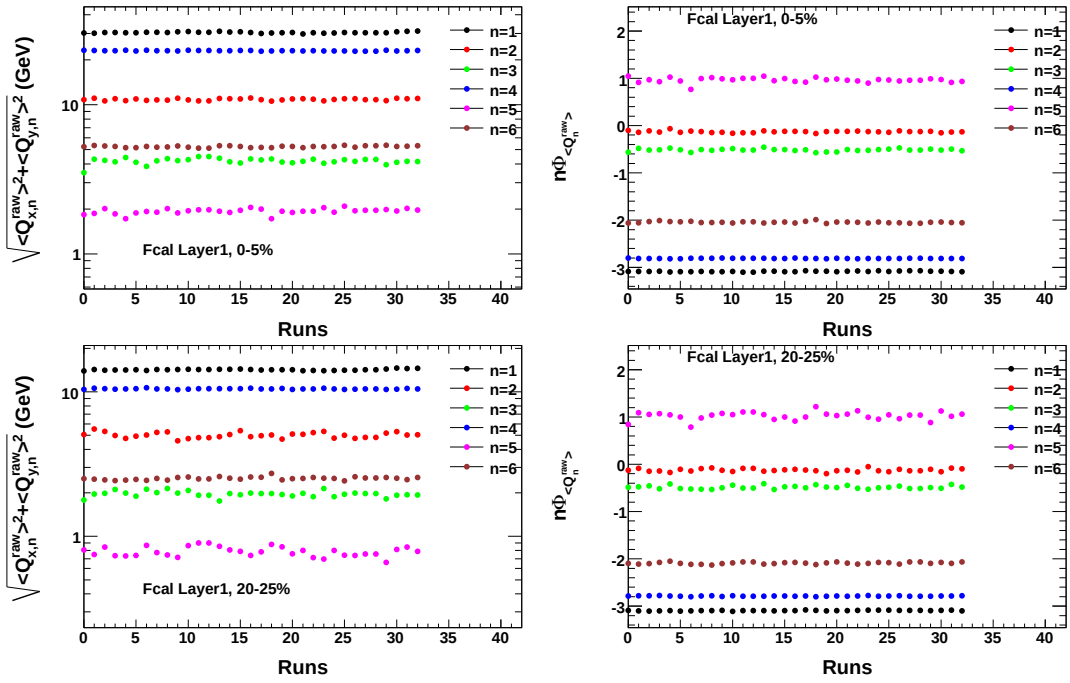

Figure 71: Run by run dependence of $|Q_n^{Raw}|$ and $n\Phi_n$ for two different centralities

7.6 Determining the detector resolution

Event plane determination: As mentioned before, due to the finite number of particles of the system, the measured flow vector fluctuates around its true value. Defining the direction of the true flow vector as the x-axis, such dispersion distribution can be expressed as (assuming gauss-like distribution which is true when multiplicity is large: central-limit theorem)

$$\frac{dN}{dQ_{x,n}dQ_{y,n}} = \frac{1}{\pi\sigma_n^2}\exp\left(-\frac{\left|\overrightarrow{Q_n} - \langle Q_n\rangle\right|^2}{\sigma_n^2}\right), \tag{56}$$

with equal variance in x and y direction,

$$\sigma_y^2 = \sigma_x^2 = \sum_i w_i^2 \cos^2 n\phi_i = \frac{N\left\langle w^2\right\rangle}{2} \equiv \frac{\sigma_n^2}{2}. \tag{57}$$

where $\langle w^2\rangle$ represent the average of the quadrature weight, and N is the number of particles. We can also rewrite the dispersion equation 56 in terms of Q_n and relative angle $\Delta\Psi_n = \Psi_n - \Psi_{\mathrm{RP,n}}$ between measured and mean flow vector as

$$\frac{dN}{Q_n dQ_n d\left(n\Delta\Psi_n\right)} = \frac{1}{\pi\sigma_n^2} \times \exp\left(-\frac{Q_n^2 + \langle Q_n\rangle^2 - 2Q_n\langle Q_n\rangle\cos n\Delta\Psi_n}{\sigma_n^2}\right), \tag{58}$$

Equations 56-57 show that the precision with which we determine Ψ_n depends only on the magnitude of $\langle Q_n\rangle$ relative to its variance σ_n,

$$\chi_n = \frac{Q_n}{\sigma_n}, \tag{59}$$

In fact, integrating out the Q_n in Eq. 58, gives the expression for the dispersion distribution for the reaction plane angle,

$$\frac{dN}{d\Delta n\Psi_n} = \frac{\exp(-\chi_n^2)}{\pi}\left\{1 + z\sqrt{\pi}\left[1 + erf(z)\right]\exp(z^2)\right\} \tag{60}$$

with $z = \chi_n^2\cos n\Delta\Psi_n$. Because $\langle Q_n\rangle$ is proportional to average flow signal $\langle v_n\rangle$ and N, $\langle Q_n\rangle = N\langle v_n\rangle\langle w^2\rangle$, assuming $\langle w\rangle^2 = \langle w^2\rangle$, we have $\chi_n = \sqrt{2N}\langle v_n\rangle$. This implies that if we increase the multiplicity by factor of 2, χ_n would increase by a factor of $\sqrt{2}$. This is the bases for the two sub-event and three sub-event methods for calculating the reaction plane resolution.

Reaction plane resolution: The general expression for reaction plane resolution can be derived directly from Eq. 60,

$$\langle\cos k\Delta n\Psi_n\rangle = \frac{\chi_n\sqrt{\pi}}{2}e^{-\frac{\chi_n^2}{2}}\left[I_{\frac{k-1}{2}}(\frac{\chi_n^2}{2}) + I_{\frac{k+1}{2}}(\frac{\chi_n^2}{2})\right] \tag{61}$$

where the I_n is the modified Bessel functions of the first kind. However, in order to calculate the resolution, we first need to know χ_n, which can not be obtained from distribution Eq. 60, since we do not know $\Psi_{\mathrm{RP,n}}$. Instead, we employ the two-subevent method and three-subevent method to calculate the resolution.

7.6.1 Two sub-event method

In order to determine χ we use the two subevent method. This involves dividing the detector into two sub-detectors having nearly (possibly exactly) equal acceptance and to determine the event plane for each of them. We call the two reaction planes obtained from the two sub-detectors as Ψ_n^A and Ψ_n^C. Both of these will fluctuate about the true reaction plane according to Eq.60 but with a χ value $\sqrt{2}$ smaller that that of the full detector. This is because χ scales with number of particles as $\sim\sqrt{N}$ and each of the two sub-detectors have half the number of particles than the full detector We denote the sub-event χ by χ_S. Thus we have :

$$\chi_{sub} = \chi_A = \chi_C = \frac{\chi}{\sqrt{2}} \tag{62}$$

Using Eq.60, we can determine the distribution of the relative angle $\Delta n\Psi_n' = n(\Psi_n^A - \Psi_n^C)$:

$$\frac{dN}{d\Delta n\Psi'_n} = \frac{e^{-\chi^2_{sub}}}{2}\left[\frac{2}{\pi}(1+\chi^2_{sub}) + z(I_0(z)+L_0(z)) + \chi^2_{sub}(I_1(z)+L_1(z))\right] \quad (63)$$

Where $z = \chi^2_{sub} cos(\Delta n\Psi'_n)$ and L_0 and L_1 are modified Sturve functions. This distribution is normalized between 0 and π. This distribution can be experimentally measured and then fitted with Eq.63 to obtain χ_{sub}. from which we can obtain the full detector's χ (by multiplying by $\sqrt{2}$) and the use Eq.61 to obtain the full resolution.

In our analysis, we use the Fcal for determining the reaction plane. We choose the $A-Side$ FCal as one of the sub detectors and the $C-Side$ FCal as the other. The distribution of $\Delta\Psi'_n$ is similarly obtained with Ψ^A_n being the reaction plane obtained with A side FCal and Ψ^C_n the reaction plane obtained with C side FCal. The sub detector χ_{sub} values are then calculated by fitting the distribution of $\Delta\Psi'_n$ with Eq.63. Then Eq.61 us used with $\chi = \sqrt{2}\chi_{sub}$ to obtain the full resolution.

There is another method of obtaining the sub-detector resolution. Consider the cosine of $n(\Psi^A_n - \Psi^C_n)$:

$$\begin{aligned} cos\left(n(\Psi^A_n - \Psi^C_n)\right) &= cos\left(n(\Psi^A_n - \Psi^{True}_n) - n(\Psi^C_n - \Psi^{True}_n)\right) \\ &= cos\left(n(\Psi^A_n - \Psi^{True}_n)\right) cos\left(n(\Psi^C_n - \Psi^{True}_n)\right) \\ &\quad + sin\left(n(\Psi^A_n - \Psi^{True}_n)\right) sin\left(n(\Psi^C_n - \Psi^{True}_n)\right) \end{aligned} \quad (64)$$

Since the individual fluctuations in $(\Psi^A_n - \Psi^{True}_n)$ and $(\Psi^C_n - \Psi^{True}_n)$ are independent of each other, averaging over many events, we have:

$$\left\langle cos\left(n(\Psi^A_n - \Psi^{True}_n)\right) cos\left(n(\Psi^C_n - \Psi^{True}_n)\right)\right\rangle = \left\langle cos\left(n(\Psi^A_n - \Psi^{True}_n)\right)\right\rangle \left\langle cos\left(n(\Psi^C_n - \Psi^{True}_n)\right)\right\rangle \quad (65)$$

$$\left\langle sin\left(n(\Psi^A_n - \Psi^{True}_n)\right) sin\left(n(\Psi^C_n - \Psi^{True}_n)\right)\right\rangle = \left\langle sin\left(n(\Psi^A_n - \Psi^{True}_n)\right)\right\rangle \left\langle sin\left(n(\Psi^C_n - \Psi^{True}_n)\right)\right\rangle \quad (66)$$

Now, since the fluctuations of the observed reaction plane about the true reaction plane must be symmetric (that is, the probability of $\Psi^{A/C}_n - \Psi^{true}_n$ to be $+\Delta\Psi_n$ and $-\Delta\Psi_n$ are the same), when averaged over many events we must have:

$$\left\langle sin\left(n(\Psi^{A/C}_n - \Psi^{true}_n)\right)\right\rangle = 0 \quad (67)$$

Thus Eq. averaged over many events becomes:

$$\left\langle cos\left(n(\Psi^A_n - \Psi^C_n)\right)\right\rangle = \left\langle cos\left(n(\Psi^A_n - \Psi^{True}_n)\right)\right\rangle \left\langle cos\left(n(\Psi^C_n - \Psi^{True}_n)\right)\right\rangle = \left\langle cos\left(n(\Psi^{A/C}_n - \Psi^{True}_n)\right)\right\rangle^2 \quad (68)$$

The last equality in Eq.68 follows from the fact that $\left\langle cos\left(n(\Psi^{A/C}_n - \Psi^{True}_n)\right)\right\rangle$ which are the resolutions of sub-detector A and C repectively, are equal to each other. Thus we get the sub detector resolution as:

$$\left\langle cos\left(n(\Psi^{A/C}_n - \Psi^{True}_n)\right)\right\rangle = \sqrt{\left\langle cos\left(n(\Psi^A_n - \Psi^C_n)\right)\right\rangle} \quad (69)$$

The RHS of the above equation is experimentally evaluated and from which we can obtain the sub-detector resolution. We can then use this resolution in the LHS of Eq.61 to obtain the sub-detector χ_{sub}. Form which we obtain the full detector χ as $\sqrt{2}\chi_{sub}$. In principle, both the fit method (Eq.63) and the $\langle cos\rangle$ method (Eq.69 and Eq.61) should give us the same value of χ_{sub} (and hence same value of χ). Any difference in between the two values can be used as a systematic error on the reaction plane resolution.

7.6.2 Three sub-event method

The three-subevent method does not require knowledge of χ_n. Instead, we directly calculate the resolution of a given detector A by using its correlation with the event planes from two other detectors B and C sitting at different η windows.

$$\mathrm{Res}\{\Psi^A_{n|k}\} = \langle \cos(kn(\Psi^A_n - \Psi_{\mathrm{RP,n}}))\rangle = \sqrt{\frac{\left\langle \cos\left(kn\left(\Psi^A_n - \Psi^B_n\right)\right)\right\rangle \left\langle \cos\left(kn\left(\Psi^A_n - \Psi^C_n\right)\right)\right\rangle}{\left\langle \cos\left(kn\left(\Psi^B_n - \Psi^C_n\right)\right)\right\rangle}} \tag{70}$$

Once $\mathrm{Res}\{\Psi^A_{n|k}\}$ is known, we can calculate the χ_n using Eq. 61. There are many combinations for A, B and C. One such example is $A = FCal$, $B = EMBarrel_N$ and $C = EMBarrel_P$. The main advantage of the three-sub-event method is that it allows many independent estimates of the resolution for each event plane, thus we can estimate more reliably the associated systematic errors.